POLITECNICO DI TORINO

Collegio di Ingegneria Chimica e dei Materiali

Master of Science Course
in Materials Engineering for Industry 4.0

Master of Science Thesis

Modeling the Influence of Wear on the Evolution of the Coefficient of Friction

Tutors

Prof. Milena Salvo
Ass. Professor Frédéric Cabanettes
Prof. Cedric Bosch
Dr. Emilie Viéville

Candidate

Rao Muteeb Ur Rehman

October 2025

Erasmus Mundus Joint Master in Manufacturing 4.0 by intElligent and susTAinable technologies

MASTER's Degree Thesis

Modeling the Influence of Wear on the Evolution of the Coefficient of Friction

Supervisors

Ass. Professor Frédéric Cabanettes

Dr. Emilie Viéville

Prof. Cedric Bosch

Prof. Daniele Ugues

Candidate

Rao Muteeb Ur Rehman

September 2025

Abstract

Friction and wear are essential parameters affecting the reliability, performance, and lifespan of mechanical parts subjected to sliding contact. Their reliable prediction is vitally important to optimize design, minimize maintenance, and avoid premature failure. This thesis develops and calibrates three numerical models to predict wear and the evolution of the coefficient of friction (CoF) in dry sliding contact, with a focus on the tribological pair of a stainless steel disc and an nickel alloy sphere. The modelling tool employs Archard's wear law, with contact pressures in contact mechanics being updated iteratively to account for changes in geometry as a result of wear. At the macro scale, global pressure distribution variation over time for a nominally smooth surface is modeled using a Winkler elastic foundation model. Surface roughness is treated at the micro scale by the bearing area curve so that real contact area and local pressures can be calculated directly, and wear can be more accurately predicted. Experimental validation was conducted by Rtec tribometer testing under controlled speed and load conditions, then by post-testing characterization using 3D profilometry for measurement of worn height and wear volume, and by scanning electron microscopy (SEM) for wear mechanism investigation. The wear coefficient (K) was experimentally calibrated from wear volumes and applied to all models. Predictions from the models were verified against worn height, sphere worn-patch diameter, total wear volume, and CoF evolution.

Results show that all models predicted worn height and total wear volume correctly within experimental uncertainty. Versions 1 and 2 caught CoF trends correctly, with a small initial offset due to approximating a constant interfacial shear strength (τ_0) from initial conditions. Version 3 overestimated CoF, with a linearly increasing CoF due to coarse micro-contact discretizations. The findings prove that the future research should be targeted towards a coupled two-scale modelling scheme, enabling consistent wear-life prediction over a broader range of materials and operating conditions.

Acknowledgments

As I reach the end of my Master's experience, I am reminded that research is never an individual activity. This thesis is completed by the guidance, generosity, and support of many, each of whom has contributed in his/her own way to this achievement.

I would like to begin with a sincere gratitude to my supervisor and co-supervisor, Prof. Frédéric Cabanettes and Dr. Emilie Viéville, whose understanding, patience, and positive criticisms have been a valuable addition to my research and academic development. Their encouragement and trust pushed me to step outside my comfort zone.

I am also deeply grateful to Prof. Cédric Courbon and Coralie Spicker for their insightful advice and support, which have enriched my work immensely.

I thank École Centrale de Lyon (ENISE), École des Mines de Saint-Étienne, and Politecnico di Torino for giving me the opportunity to grow as a researcher within an international and intellectually stimulating atmosphere.

To my friends and colleagues, I am grateful for the times we shared in terms of challenges in the classroom, debates, and many instances of support along the way.

To my family, I am most grateful for your unwavering confidence in me as a pillar of strength during my academic journey. To my mother, for every sacrifice, prayer, and love without which I would never have made it where I am today, I dedicate this milestone to you.

To all who have been with me on the journey, thank you.

Table of Contents

List of Figures

List of Tables

Nomenclature

Symbol	Description	Units
CoF, μ	Coefficient of friction	– (dimensionless)
CO_2	Carbon dioxide	–
H	Hardness of the material	Pa
SiC	Silicon carbide	-
Al_2O_3	Aluminium oxide	-
K	Wear coefficient (Archard's law)	mm^3/N·m
F_t	Frictional force	N
F_n	Applied normal force	N
τ	Shear strength	Pa
A_r	Real area of contact	m^2
P	Pressure	Pa
K_N	Normal stiffness per unit area	N/m^3
u_z	Vertical deformation	m
C_W	Geometry dependent Winkler constant	–
E^*	Effective elastic modulus	Pa
b_H	Winkler contact width	m
V	Wear volume	mm^3
L	Sliding distance	m
α	Parameter (depends on debris size/fraction)	–
d^*	Critical length for deformation	m
γ	Surface energy	J/m^2
G	Shear modulus	Pa
ν	Poisson's ratio	–
σ_j	Junction stress	Pa
μ_a	Adhesive component of CoF	–
μ_p	Ploughing component of CoF	–
μ_{pc}	Ploughing CoF due to trapped debris	–
N_{pc}	Number of ploughing contacts with debris	–
ρ	Normalized wear particle density	–
λ	Scaling exponent (ploughing model)	–
μ_{pc1}	Ploughing friction from a single particle	–
R_a	Arithmetic average roughness	µm
L_t	Total profile length	mm
L_s	Sampling length	µm
λ_c, L_c	Cut-off wavelength for roughness	mm
N	Number of sampling lengths	–

A_0	Contact area at experiment end (reference)	m^2
A_{new}	Contact area at simulation step	m^2
τ_0	Shear strength from initial CoF	Pa
μ_0	Initial coefficient of friction	–
Δh_{ij}	Wear depth at element (i, j)	m
P_{ij}	Local pressure at element (i, j)	Pa
V_{ij}	Local sliding velocity at element (i, j)	m/s
Δt	Time step for wear calculation	s
δ	Penetration depth of sphere into disc	m
$\texttt{GAP}_Z$	Gap between sphere and disc	m
$BIN_{\text{penetration}}$	Binary contact indicator	–
dx, dy	Discretized element dimensions	m
$Z_{\text{min}}, Z_{\text{max}}$	Bounds in bisection loop	m
$Z_{\text{Sphere\_new}}$	New sphere position	m
A_{real}	Real contact area	m^2
$F_{\text{penetrate}}$	Force from real area × hardness	N
P_{Winkler}	Pressure from Winkler model	Pa
$P_{\text{rough contact}}$	Pressure from rough contact model	Pa

Chapter 1

Introduction

In today's world, technology and machines are a big part of our daily lives, from cars and airplanes to a small chip in cellphone and household appliances, we expect these machines to work efficiently and for long time. But when surfaces on these machines interact with each other, they get damaged and lead to problems like energy loss, breakdown and expensive repair. This chapter begins with the industrial background that highlight the need to understand these surface interactions and their effect on machine or component life cycle, leading to an introduction of the scientific field (tribology) concerned from this interaction with its historical development. It then outlines the specific goals and scope of this thesis. By establishing a clear understanding of the basic principles and current applications of tribology, this chapter lays the groundwork for the more detailed analysis presented in the following chapter.

1.1 Industrial Background

Across the whole world, machines and components form the backbone of the industry, from the manufacturing and transportation to the energy production and processing. One important factor which is influencing the performance and efficiency in a component is the surface interactions. These surfaces interactions often go unnoticed, are responsible for the energy consumption and maintenance efforts. In fact, these surface interactions account for approximately 23% in four large energy consuming sectors: transportation, industry, energy industry, and residential, 20% is needed to overcome friction, and an additional 3% is tied to wear related repairs and component replacement [1], these phenomenons also impact the CO_2 emissions as shown in figure 1.1. Advancements in material research and development, surface coatings, and lubrication technologies have the potential to reduce energy consumption in the transport and power sectors by up to 25% and 20%, respectively [1], underlining the importance of surface engineering in improving efficiency and in achieving sustainability goals of the industry.

These phenomenon might concerns several industries as nuclear energy production, where components operate under severe conditions such as high temperatures, radiation, and heavy pressures. In different assemblies, most critical component are the ones, which are moving against each other. A commonly used material pairing in nuclear components is steel and nickel based alloys. These materials often slide against each other, resulting in surface interaction which can lead to potential material loss depending on load conditions over prolonged operation cycles.

One of the important challenge in such components is understanding, how different wear mechanisms can affect the evolution of coefficient of friction (CoF).

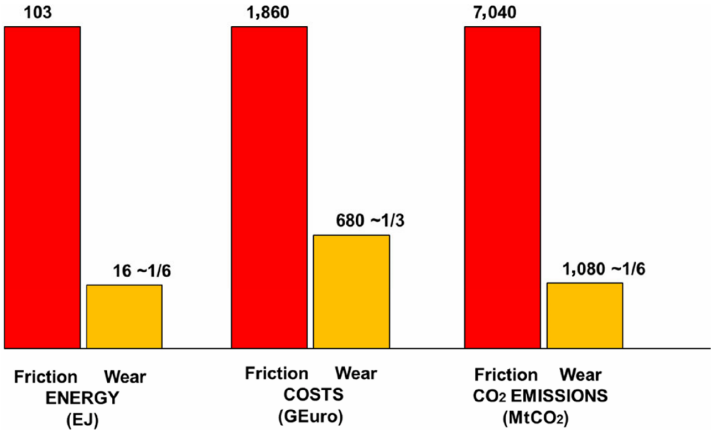

Figure 1.1: Energy consumption, costs and CO_2 emissions due to friction and wear globally [1]

1.2 Introduction to Tribology

The term tribology finds its origin in the Greek *tribos*, meaning rubbing, it was formally put forward by the British Department of Education and Science in the Jost Report of 1966. This report brought to light the vast economic losses suffered by UK industries due to poor friction and wear control and put forth the idea of tribology as a rather inclusive scientific discipline dealing with these issues [2] . The name tribology is fairly recent, but its understanding goes back much farther and has been applied throughout history. The earliest civilizations would apply natural oils and greases to reduce on friction for transport systems and making tools more efficient. By approximately 1880 BC, the ancient Egyptians might have been using manpower along with some elementary lubricants to reduce friction while transporting large statues as shown in the figure 1.2 [3] [4].

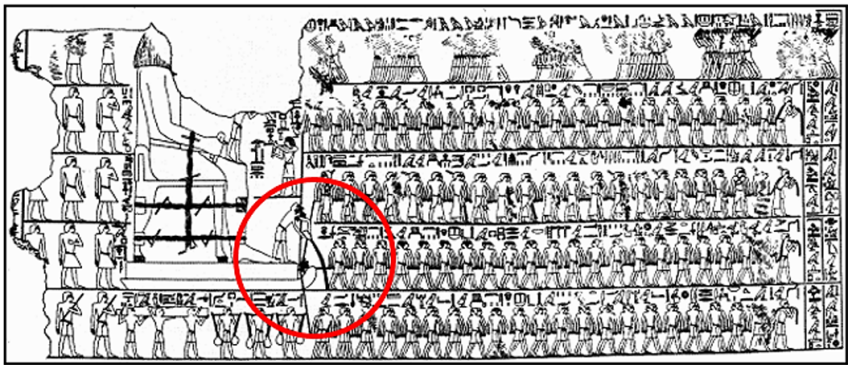

Figure 1.2: Transporting an Egyptian statue from the tomb of Tehuti-Hetep, El-Bersheh (1880 BC) [3] [4]

In the 15th century, Leonardo da Vinci studied friction, and then foundational laws were set forth by Amontons and Coulomb in the 17th and 18th centuries [5]. Tribological effects appear in systems comprising contacting surfaces, e.g., brake pads, turbine bearings, and joints. Hence, while friction helps in braking, frictional losses also represent loss of energy that goes into damaging surfaces. Wear reduces the life of components and increases maintenance cost, hence, lubrication through

oils, greases, coatings, or surface textures is consider essential to counteract these effects.

Modern tribology started with Hertz as early as 1882 with his theory on elastic contact between curved bodies [6], which gave rise to a series of other models and advance research into the subject [7].

Tribology is an interdisciplinary discipline as shown in figure 1.3 bridging mechanical engineering, materials science, and surface chemistry. Friction and wear shall be understood with contact mechanics, stress analysis, solid material properties, and chemical behavior of lubricants and oxides.

With the development in technology and research, friction and wear are not considered fixed properties anymore in modern tribology. Traditionally, the coefficient of friction is assumed constant in classical design, following the Amonton's and Coulomb's laws. Currently, it is believed to change with surface roughness, the lubrication regime, the temperature of the contact, materials used, and the nature of the load. In dry sliding between steel surfaces, for example, CoF varies between 0.1 and over 1.0, depending on the surface and environmental conditions [2].

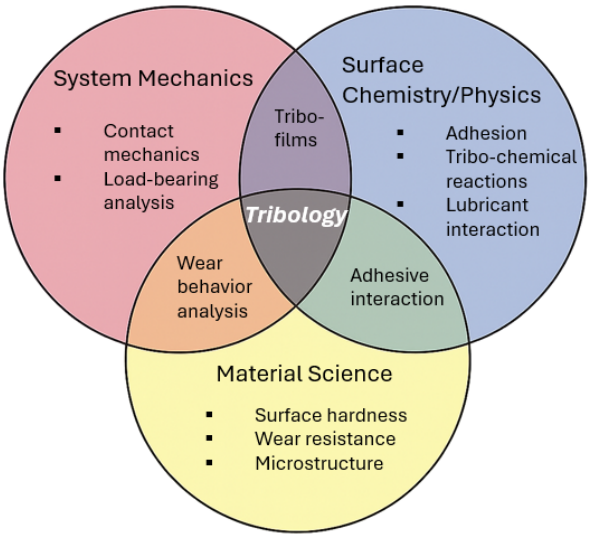

Figure 1.3: Interdisciplinary connections of tribology

Studying these dynamics, tribology has now involved new experimental and computational methods. High-resolution characterization tools like Scanning Electron Microscopes (SEM) and Atomic Force Microscopes (AFM) are now used to understand wear mechanisms at micro and nano scales. Analytical models like Archard's wear laws [8] are being used in conjunction with finite element simulations, and tribometers to simulate and measure behavior under controlled conditions [5] [9]. With these tools, realistic, predictive wear models factoring contact mechanics, material degradation, and energy dissipation can be made.

In short, tribology is an important field to ensure that mechanical systems work efficiently and reliably. Knowledge in friction, wear, and lubrication goes beyond mere technical interest, it is key to the sustainability of the existing technologies.

1.3 Objective and Scope of the Thesis

This thesis intends to assess and anticipate tribological behavior of stainless steel and inconel alloy in dry sliding. Figure 1.4 presents an overview of the thesis workflow.

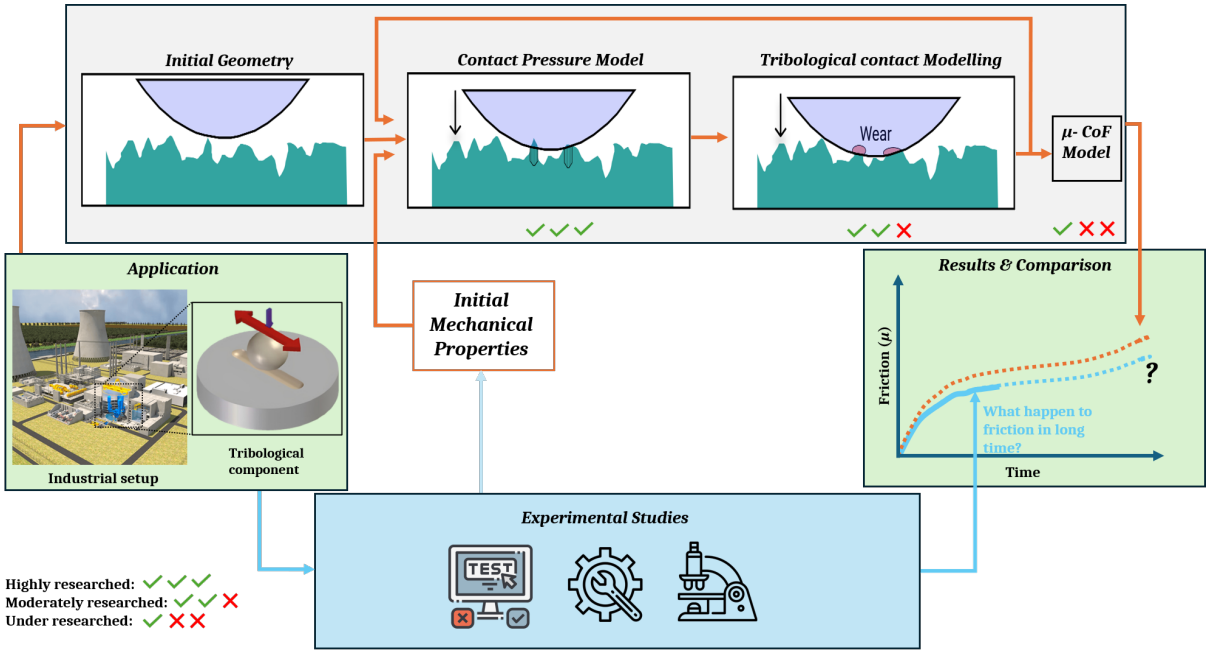

Figure 1.4: Scope of the thesis

The main objectives of this thesis are as follows:

- Develop computational models for wear and CoF evolution incorporating effects caused by contact pressure, real contact area, and surface roughness.
- Validate the proposed models using experimental data including worn geometries, worn volumes, and CoF trends.
- Identify key parameters that link contact conditions, wear mechanisms, and CoF behavior of a tribological system.

The experimental and computational approach advances the understanding of wear and friction in industrial applications.

Chapter 2

Literature Review

The goal of this chapter is to present an overview of the basic principles, experimental observations, and modelling approaches to wear and friction. The chapter starts with the explanation of important basic concepts such as tribo-contact, wear mechanisms, and friction fundamentals, followed by a review of historical development in wear and friction modelling from analytical theory to sophisticated numerical models. This background support the following effort in this thesis, which is concerned with development of wear and friction evolution models under dry contact conditions.

2.1 Tribological Contact

Tribological contact has a significant influence on the performance, life, and efficiency of mechanical systems. Surface interaction governs the onset and development of friction and wear [2]. This section presents an introduction to the basics of tribo contact with a focus on classification of contacts by considering mechanical interactions between conformal and non-conformal surfaces and how dry or lubricated conditions influence such interactions. These variations are significant to interpret experimental data and to design systems that behave reliably under a range of mechanical and environmental conditions.

One of the fundamental concepts of tribological contact is the distinction between apparent and real contact area. The apparent area is the visible area of contact, whereas the real area comprises discrete microscopic asperity contacts caused by surface roughness, as shown in figure 2.1 [10].

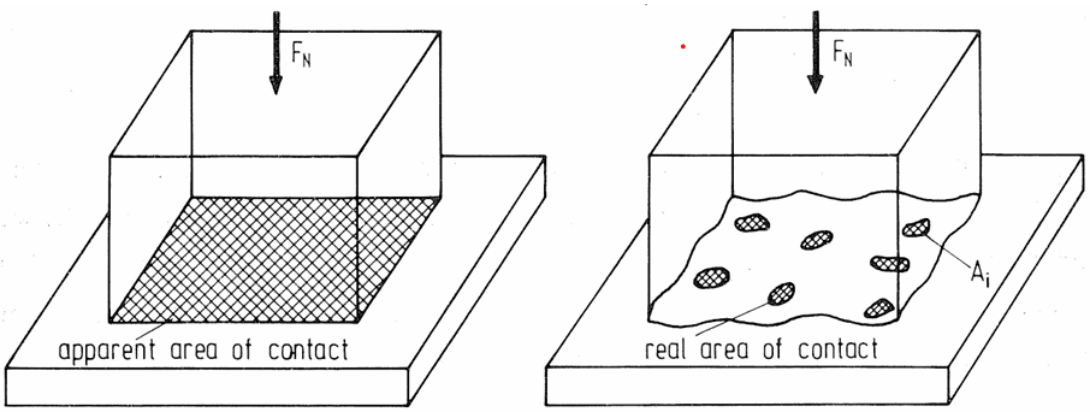

Figure 2.1: Apparent and real area of the contact [10]

Understanding of real contact area is necessary to be able to anticipate interfacial behavior, i.e., energy dissipation, shear strength, and tribofilm formation. It is especially critical in sliding under dry conditions, where junction growth, debris, and third-body effects are continuously changing [9]. This real area having asperities will be the first points to cause the contact between two bodies and

then upon material degradation over prolonged sliding time, causes the evolution of real contact area.

2.1.1 Type of contact

In tribological testing and component design, a distinction needs to be made between conformal and non-conformal contacts because they influence contact behavior and wear development in different ways.

- In conformal contact, the shape of the contacting surfaces provides a large, well-matched contacting area at the initiation of the interaction when two bodies mate ideally or at least very nearly ideally without experiencing any deformation. The contact formed in such a situation involves a large area of the surface of the two bodies. This area is kept constant during the sliding process, and this can facilitate the interpretation of friction and wear in constant conditions. Some examples are linear guide rails, disc brake assembly, journal bearing as shown by figure 2.2 where the load is distributed over a large area [2].

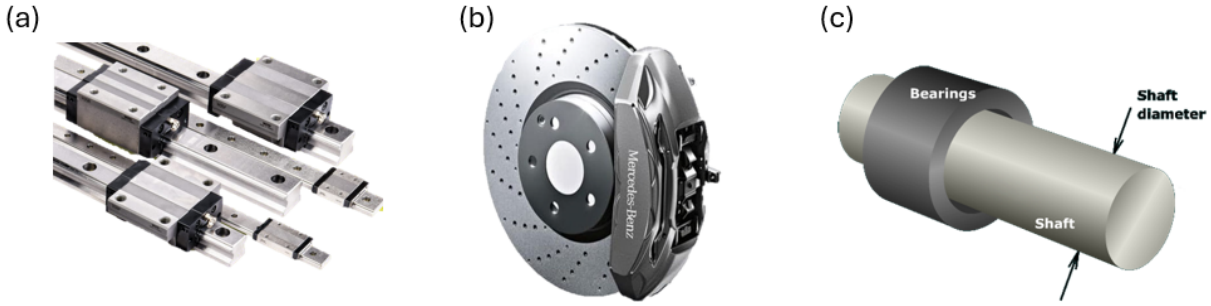

Figure 2.2: Conformal contact applications (a) linear guide rails [11], (b) disc brake assembly [12], and (c) journal bearing [13]

- Non-conformal contact is described as the interaction of bodies having different profiles with respect to one another. In this situation when these two bodies are brought into contact without any deformation, they will start touching at a point (point contact case) or along a line (line contact case). Such arrangements create a small contact area initially, which has a tendency to change during the process of wear. As wear takes place from one or both surfaces, the contact geometry is constantly changing, often generating a larger contact area and altered stress distribution. This can lead to a dynamic contact condition, making wear mechanisms more complex and more dependent on the operating parameters. Common examples of the application of non-conformal contact include cylindrical element bearings and ball bearings as shown in the figure 2.3.

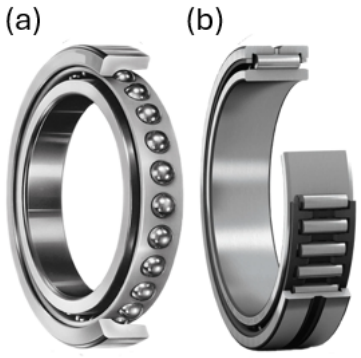

Figure 2.3: Non-conformal contact applications (a) ball bearings, and (b) cylindrical element bearings [14]

2.1.2 Condition of contact

The tribological contacts are also classified on the basis of the nature of the contact conditions into two broad categories: dry contact and lubricated contact, both experiencing different frictional and wear behavior. There is no fluid medium present between the contacting surfaces in dry contact, and hence the surface asperities interact with one another directly. This leads to comparatively higher coefficient of friction and increased wear because of prevailing adhesive and abrasive wear mechanisms. Such kinds of conditions are typically found in high-temperature uses, vacuum, or mechanical systems that are meant to run without lubrication [2]. The following figure 2.4 shows wear intensity against load and temperature for the dry and lubricated conditions.

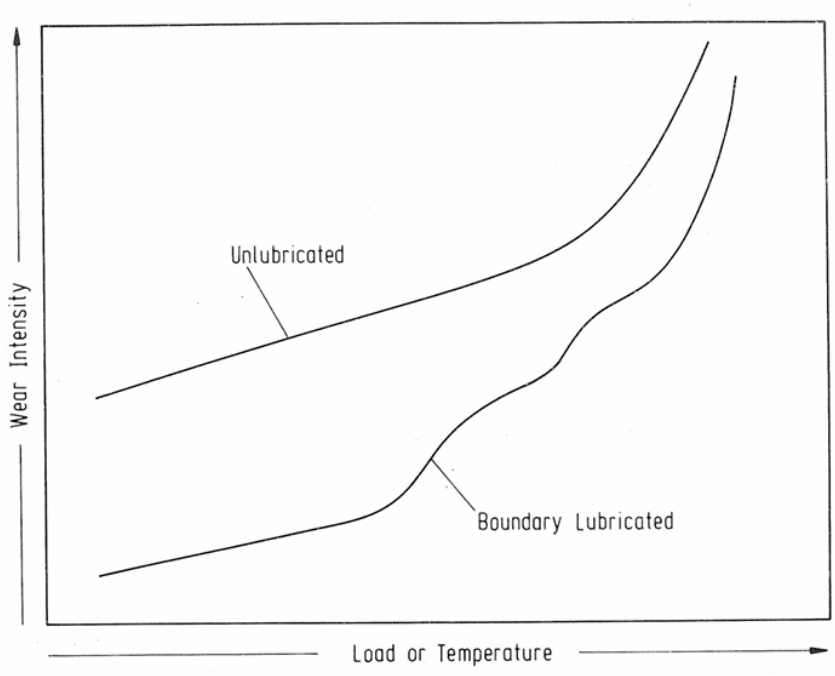

Figure 2.4: Wear intensity as function of load and temperature in dry and lubricated conditions [10]

On the other hand, lubricated contact involves the presence of a film of fluid (oil, grease, or other lubricants) between the surfaces and has the ability to significantly minimize both friction and

wear. Understanding the nature of tribological contact, whether conformal or non-conformal, dry or lubricated, is important as these conditions dictate the way actual contact areas form during sliding. The way the contact stresses are distributed and how extensive the asperity interactions are have significant impacts on the way material loss initiation occurs at the interface. Therefore, a sensible next step is to examine the wear mechanisms, since they directly result from the contact conditions.

2.2 Fundamentals of Wear

Wear is the gradual surface damage caused by the relative motion between two solid bodies, during which material is progressively detached or deformed from one or both surfaces. Relative motion includes sliding, rolling, impact, and oscillations which produces repeated mechanical interaction at the interface. If not properly controlled, these interactions can change surface profiles over time, deteriorate component functionality, and eventually result in system failure [15] [5] [2].

Wear, while seeming straightforward, is not one mechanism but rather a general term for the presence of numerous different mechanisms, which are explored in the subsection below.

These mechanisms frequently take place in combination or in succession, making wear behavior a very complex and situation dependent phenomenon. Consequently, engineers have to carefully account for wear while designing components like bearings, gears, valves, artificial joints, and cutting tools for which surface integrity is vital for performance and durability [15] [2].

2.2.1 Mechanisms of Wear

The knowledge of wear mechanisms is significant in the design of surfaces and materials with improved durability and performance. The key wear mechanisms are described as follows.

2.2.1.1 Adhesive Wear

Adhesive wear happens when two sliding solid surfaces come in contact with one another and form microscopic junctions via atomic or molecular bonding commonly known as cold welding. These bonds are usually formed under heavy normal loads and small surface separation. The sliding action continues to shear these junctions, transferring material from one surface to the other, or forming wear debris as illustrated in the figure 2.5 [5] [2] [10]. Adhesive wear depends on a number of factors such as surface roughness, material compatibility, and environmental conditions. Adhesion is greatly reduced by the presence of surface films such as oxides or lubricants. For metallic contacts, after protective films have been degraded by heat or repeated asperity contact, adhesive bonding is probable. It can lead to progressive surface damage in the form of scuffing, galling, or even seizure. Scuffing gives moderate roughening and material transfer, whereas galling gives severe plastic deformation and localized welding, which leads to component failure [15].

Mitigation methods involve surface texturing, hard coatings, optimized material pairing, and adequate lubrication to prevent metal to metal contact [5] [2].

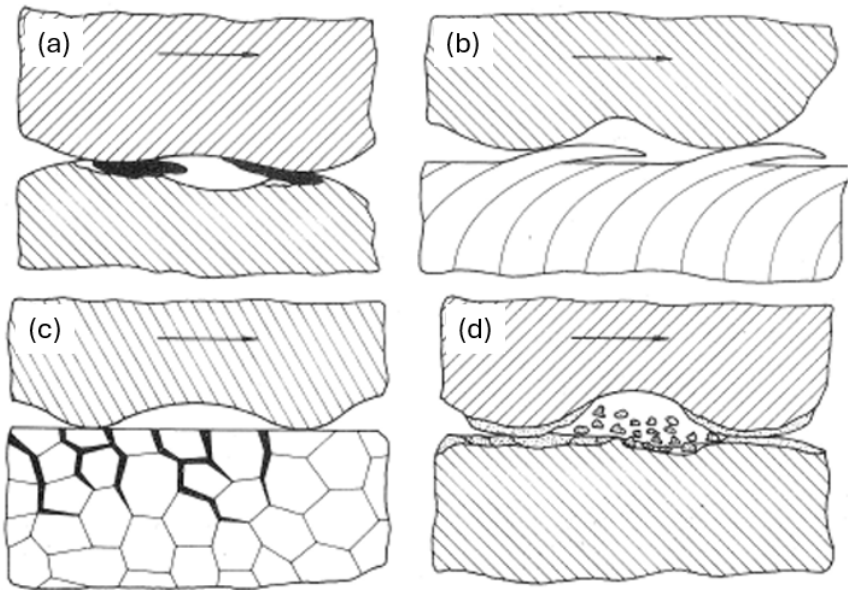

Figure 2.5: Adhesion process: (a) weld joint formation, (b) shear of junctions, (c) crack initiation, and (d) debris formation [10]

2.2.1.2 Abrasive Wear

Abrasive wear occurs due to the mechanical action when hard asperities or particles slide over a softer surface, and the material is cut away by cutting, ploughing, or cracking. There are two categories of abrasive wear, first one is, two-body abrasion where hard particles are embedded in one surface and carve into the other, producing grooves and plastic deformation. Second is three-body abrasion in which loose particles roll or slide between surfaces, generally causing less severe wear [5]. Prevailing abrasion mechanism is dependent on the hardness of the material, shape of the particles, and surface topography. Ductile materials usually suffer microcutting and ploughing, whereas brittle materials can suffer cracking or grain pull-out [15]. Following figure 2.6 shows different modes of abrasive wear mechanism.

Abrasive wear is common under particulate or dusty environments like construction, agriculture, and mining. Examples of some of the applications are crushers, grinding mills, and conveyor belts [2]. Successful countermeasures include hard wear resistant films like ceramics or TiN, and the application of bulk materials like tungsten carbide or white cast iron with high microstructural hardness and toughness [5] [15].

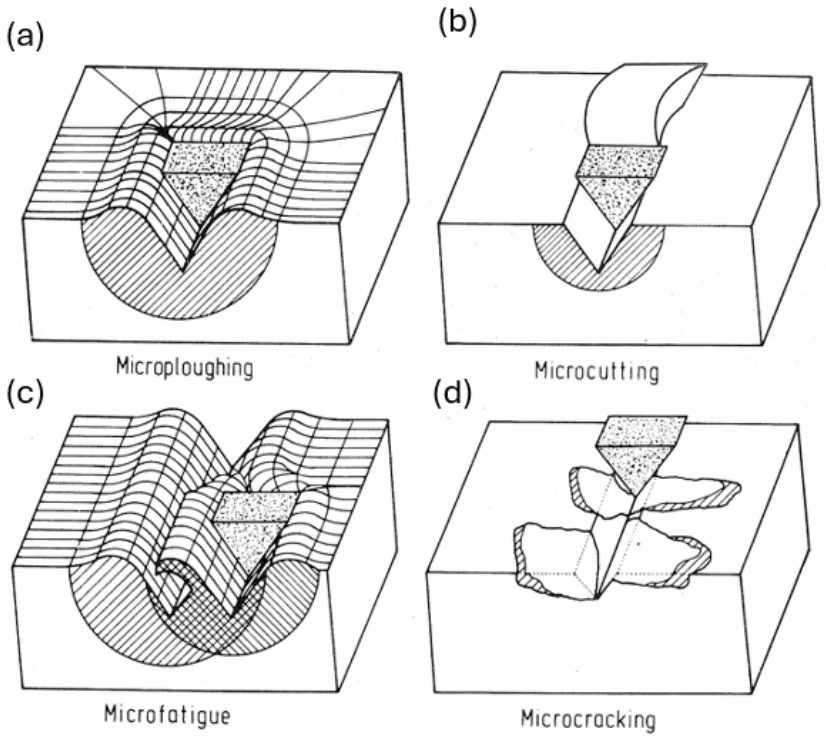

Figure 2.6: Interaction modes: (a) Microploughing, (b) Microcutting, (c) Microfatigue, and (d) Microcracking [10]

2.2.1.3 Other Wear Mechanisms

Besides adhesive and abrasive wear, other wear mechanisms can happen in the certain events:

- Fatigue wear: under cyclic loading, resulting in subsurface cracking and material loss.
- Corrosion (tribochemical) wear: due to chemical reactions of the surface with temperature, humidity, or corrosive substances.
- Erosive wear: caused by high-velocity particle or fluid impingement on a surface.
- Fretting wear: results from oscillatory motion of small amplitude between the surfaces [2] [15] [5].

Determining all the dominant wear mechanisms in a system is important for the choice of the right materials, coatings, and lubrication methods.

2.2.1.4 Wear Stages & Transition Between Wear Regimes

Since, we have established that wear consist of a number of different mechanisms providing a transitional behavior referred to as wear regime transition, is very crucial for analyzing actual world material degradation.

Wear typically goes through three stages: **running-in**, **steady-state**, and, in some cases, **accelerated wear** as shown in figure 2.7. In the running-in stage, the true contact area is caused by initial

asperity contact, micro-welding, and the elimination of surface roughness. This results in unstable, high wear rates, in addition to friction variation when surfaces adapt and tribofilms develop [16, 5].

Then, once stable contact is achieved, steady-state wear is experienced by the system, with reduced and more reproducible wear rates as interactions are stabilized by oxide films or third-body coatings [17, 9]. This stage will usually continue for the majority of the component's life. If protective coatings break down or loads become too high, accelerated wear can be established, with a rapid deterioration of the surfaces and eventual failure [2, 15].

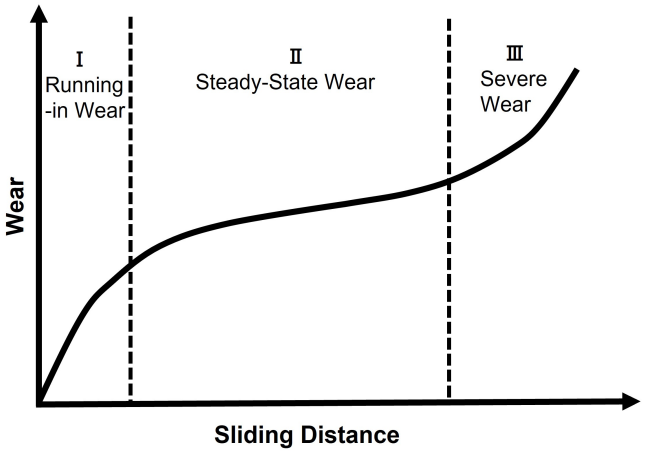

Figure 2.7: Stages of wear progression [18]

While wear has traditionally been characterized by run-in, steady state, and accelerated wear stages, Blau provided a more precise perception via his four-stage cyclic surface degradation theory. According to his theory, wear begins with undamaged surfaces with asperity interaction and mild oxidation at the interface (stage a) and subsequently evolves through surface flow, oxide thickening, and micro-tearing or delamination (stage b). Repetitive sliding forms clear grooves, cracks, and ridges, irregular contact increases stress concentration (stage c) and finally severe damage with deep grooves and spalling where the wear mechanisms change to adhesion or fatigue (stage d) as shown in figure 2.8. The theory is referred to as cyclic because surface layers go through repeated cycles of damage and partial healing, whereas in a purely linear process, there is a steady increase. This perspective thus complements the classical wear stages with a more mechanistic account of regime transitions and their correlation with debris morphology, stress concentrations, and friction, requiring immediate monitoring to avoid severe degradation. [17].

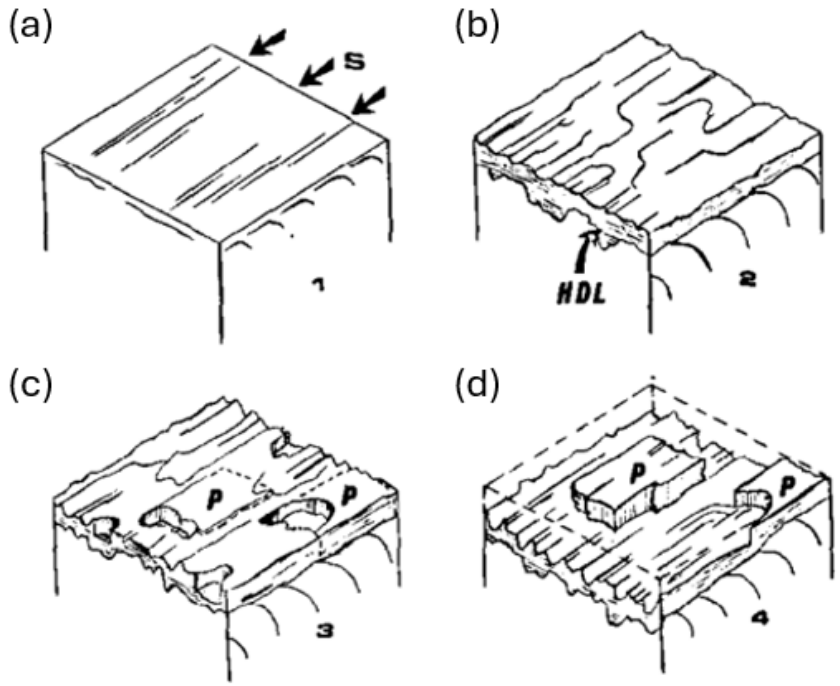

Figure 2.8: Four stages of surface deterioration (HDL: highly deformed layer; P: plateau; S: sliding direction) [17]

Wang *et al.* demonstrated similar transitions in Mo-alloyed sintered steels. With a rise in sliding velocity, wear mode shifted as shown in figure 2.9 (a) from mild oxidative wear to (b) mixed adhesion and abrasion , and finally to (c) melt wear due to thermal softening and local flow [19].

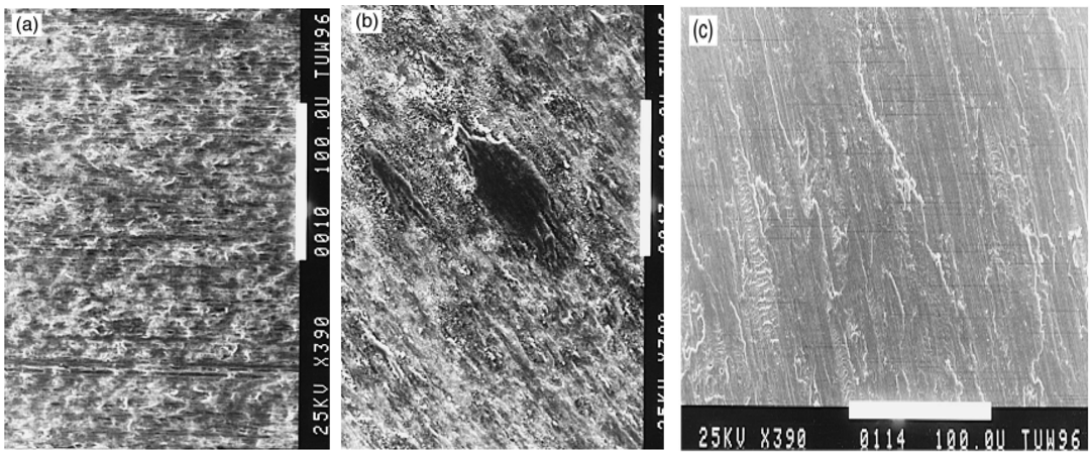

Figure 2.9: Wear transitions in Mo-alloyed steels: (a) Oxidation and adhesion, (b) Mixed regime, and (c) Thermal wear [19]

These findings highlight how transitions within the wear regime are governed by a complex interplay between surface evolution, loadings, and nature of debris which are formed during the sliding. Regulation of these factors is important for optimizing component lifetime and reliability.

2.2.1.5 Impact of Different Parameters

Wear behavior is affected by many parameters at different scale level i.e from macroscopic operational conditions to the microscopic material and surface features. Over 100 distinct parameters have been cited in the literature which impact the tribological behavior. Some major parameters influencing wear behavior significantly are applied load, sliding speed, and surface roughness and impact of these parameters is explained in more details in the following paragraphs .

These parameters heavily influence wear regime transitions, frictional characteristics, and debris morphology under dry sliding. However, experimental parameters that enter into wear analyses are vastly different; empirical models typically involve 4 or 5 variables, whereas some material based models incorporate up to nine parameters. Such a broad and inconsistent parameter selection reflects the immense complexity of wear related phenomena and the practical impossibility of having universally applicable models.

- **Effect of Load**:

  When normal load increases, real contact areas between two surfaces also increases, producing greater frictional heating and subsurface stresses, and hence favor surface deformation and third-body formation. Sahar *et al.* highlighted that, although higher loads shorten the running-in phase, they increase initial wear and shift subsurface shear stress near the surface as shown in figure 2.10, encouraging larger debris and more drastic regime changes [16, 20]. Blau said that increasing load would destabilize oxide films, triggering changes from mild to severe wear [17]. Wang *et al.* also noted a sharp rise in wear rate above 50 N, attributing this to the breakdown of oxides and thermal softening of the interface [19].

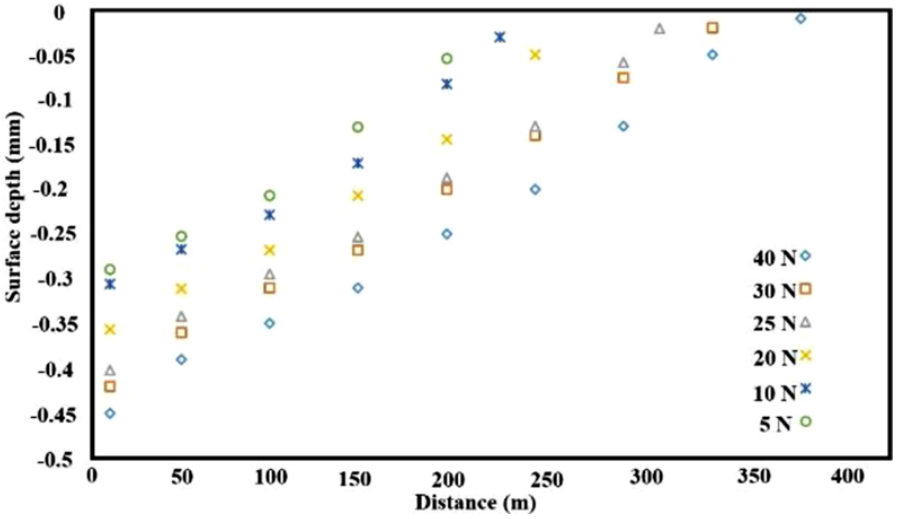

Figure 2.10: Effect of load on the location of maximum shear stress during running-in experiments

- **Effect of Sliding Velocity**:

  Sliding velocity affects wear by modifying temperature due to friction. At lower speeds, oxides form stable films and reduce wear. At higher speeds, however, higher thermal input damages

these films, creating adhesive wear and surface melting. Wang *et al.* recorded extensive smearing at slidnig speed >5 m/s, and highlighted the way the synergy of speed and load affects wear differently depending on the magnitude of load. Sahar *et al.* also found that velocity reduced running-in time but enhanced thermal stress [16]. Blau emphasized the role of velocity in debris removal and oxide film reformation [17].

Consistent with the above researches, a very comprehensive study by Mao *et al.* on a specific experiment series shows that as sliding speed increases, both the drilling fluid temperature and the wear severity rise significantly, very high speeds lead to greater frictional heating, accelerating thermal effects causing softening and promoting deeper wear scars as shown in figure 2.11 (a) and in (b) the wear rate shows a non-linear trend, initially decreasing at moderate speed but sharply increasing at higher speeds, indicating a transition in wear mechanisms (random wear behaviour) [21].

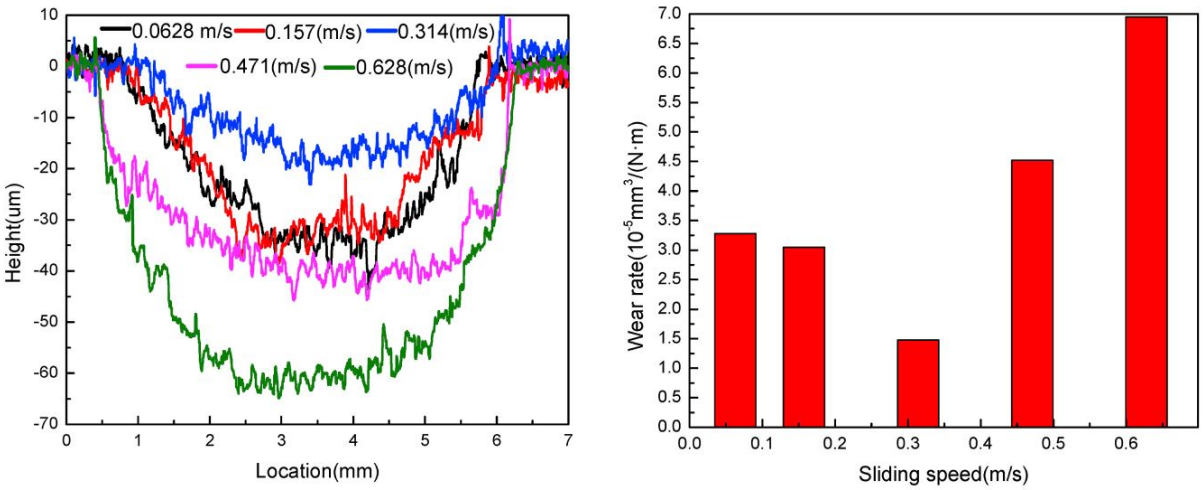

(a) Wear depth distribution

(b) Wear rate

Figure 2.11: Wear depth distribution and wear rate at different sliding speeds: (a) Wear depth distribution; (b) Wear rate [21]

- **Effect of Surface Roughness**:

  Initial surface roughness of the both surfaces in a tribological system influences contact stress distribution, oxide film development, and debris size. Sahar *et al.* observed increased surfaces enhanced subsurface shear stress and produced larger wear particles as shown in figure 2.12 [16, 20]. Smooth surfaces enabled faster adaptation and stabilized wear patterns, which is consistent with Zhang's study using finer abrasives [22].

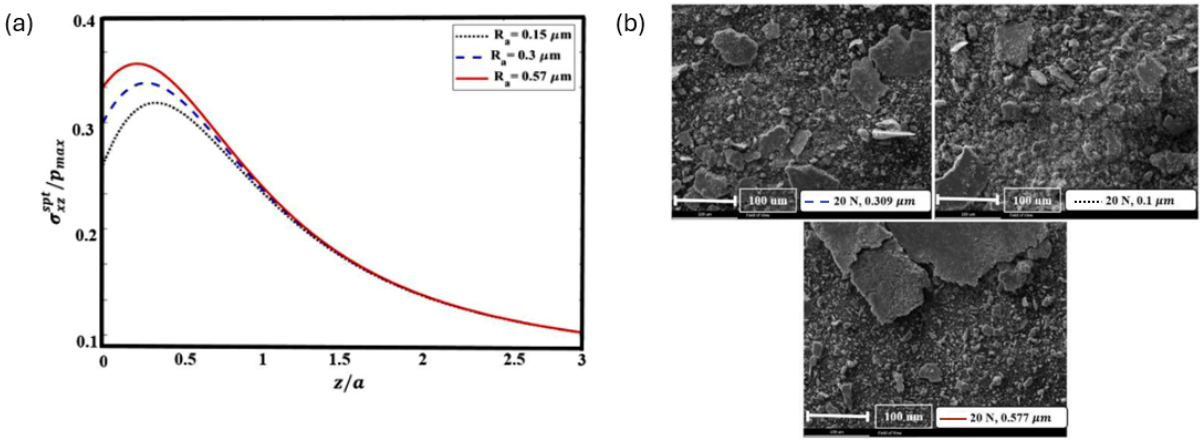

Figure 2.12: Effect of surface roughness on (a) subsurface shear stress location and (b) wear particle size [16]

2.2.2 Wear Maps and Regime Charts

As noted earlier, the pressure–velocity product (PV) is a critical parameter for wear behavior prediction in sliding contacts. It is the input energy per unit area at the interface. Low PV values are generally low loads and velocities where mild wear occurs, and stable oxide films are formed, reducing friction and material loss. As PV increases, mechanical stress and frictional heating rise, leading to oxide breakdown, surface softening, and wear in extreme regimes such as abrasion, delamination, or localized melting [5, 2, 23].

Wear maps are widely used in tribology to represent graphically the way parameters such as pressure and velocity govern wear processes. An early illustration was given by Lim and Ashby (1987) for dry steel sliding. Their map regimes convert behavior into areas such as mild oxidation, delamination, and plastic deformation, based on normalized asperity temperature. Though helpful, maps tend to emphasize high rates of wear, which fail to represent normal engineering conditions. Subsequent versions have expanded to include the effects of lubrication, temperature, and chemistry. Figure 2.13 is a good example of a wear regime map for steel in pin-on-disk geometries [23].

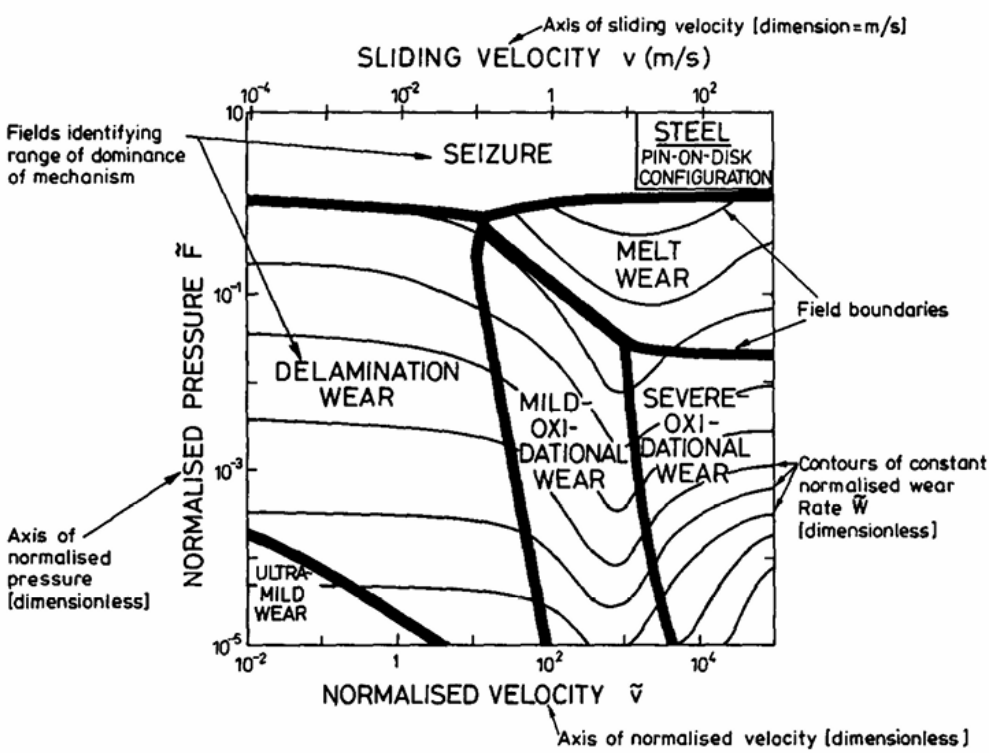

Figure 2.13: Empirical wear mechanism map for steel using a pin-on-disk configuration [23]

Other than load and speed, wear behavior is also influenced by discrete variables like lubrication, debris, and material combinations. While PV-based charts define operating limits, they fail to fully utilize the material's inherent characteristics.

Material microstructure and type also play a significant role in wear resistance even with similar PV conditions. Different types of materials polymers, metals, and ceramics exhibit enormous differences in wear rate based on different hardness, toughness, and tribochemical properties. As the figure 2.14 shows, the wear rate is generally inverse with hardness. Polymers are located in high-wear, low-hardness areas, while ceramics such as SiC and Al_2O_3 have extremely low wear due to high hardness and stability. Metals are between the two extremes, with wear resistance varying with composition and treatment of the alloys [24].

This hardness-based wear map complements PV regime charts by emphasizing materials selection requirements. Effective tribological design must consider both operational and materials factors, especially in aggressive or varying environments.

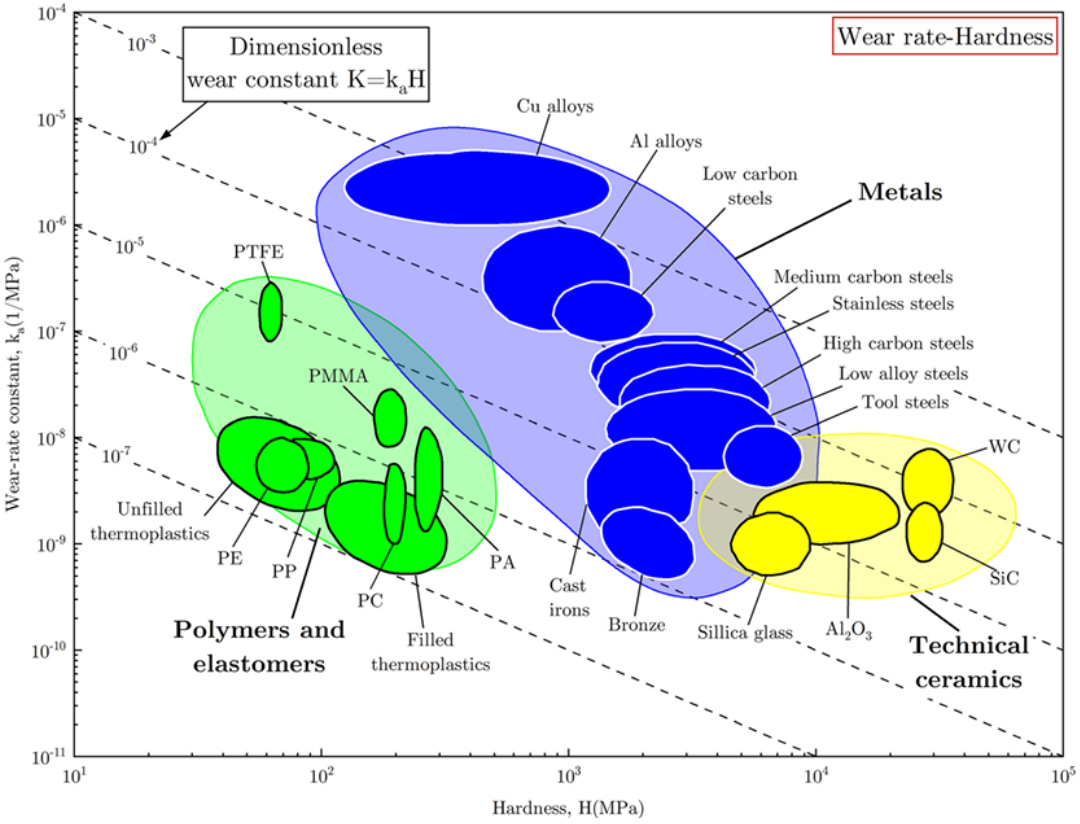

Figure 2.14: Wear-rate constant (k_s) as a function of material hardness (H) for various material classes. Dashed lines show constant dimensionless wear coefficients ($K = k_s \cdot H$) [24]

2.3 Friction Mechanism

The friction force may be described as the resistance to motion of a body sliding over another. This broad definition covers two important classes of relative motion: sliding and rolling. The study of friction has historical roots dating back to Leonardo da Vinci in the 15th century, but the laws that formally characterize the frictional behavior were first outlined by Amontons in 1699 and later refined by Coulomb in 1785. These empirical observations are commonly called the classical laws of friction, and they establish the fundamental principles that govern frictional forces under dry contact [15]:

1. The friction force is proportional to the normal load.
2. The friction force is independent of the apparent area of contact.
3. The friction force is independent of the sliding velocity.

As shown in figure 2.15, a tangential force F_t must be applied to initiate motion either by rolling or sliding, and this force must overcome the resistive frictional force at the interface.

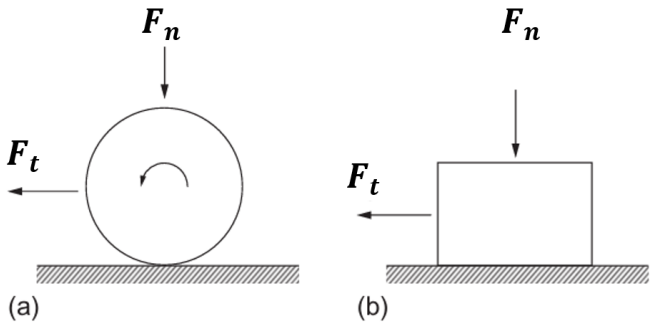

Figure 2.15: A force F_t is needed to overcome friction and cause motion by (a) rolling or (b) sliding [15]

Despite their simplicity, the classical laws of friction are important in core tribology and serve as a reference point to which more advanced, material and condition dependent models are compared. Friction at the interface between two solid bodies is not a function of a single variable but is an integration of mechanisms that vary with surface texture, composition, applied load, and surrounding environmental conditions.

The two primary mechanisms that are the basis for solid friction are *adhesion* and *deformation*. Adhesive friction occurs when the microscopic asperities of one surface make atomic scale contact with another's, causing localized adhesive bonding. As it slides, these contacts must be sheared, and this requires energy and generates frictional resistance [15]. Deformational or ploughing friction arises from the mechanical displacement of material by harder asperities on one surface penetrating or deforming the softer counterface. This mechanism becomes dominant in rough or hard-textured systems where surface topography makes a significant contribution to energy dissipation [2].

For change in frictional behavior, formation of debris also play an important role, it will be explained in more details in the following paragraphs. So, we can say that the frictional behavior exhibited by any system is the result of the complex interaction between material properties, surface topography, interfacial chemistry, and operating conditions.

2.3.1 Fundamentals of the Coefficient of Friction

The coefficient of friction (CoF), μ, is a dimensionless ratio of the tangential friction force F_t (N) to the normal load F_n (N):

$$\mu = \frac{F_t}{F_n} \tag{2.1}$$

Two forms of CoF are widely characterized: static CoF (μ_s) when motion is imminent, and kinetic CoF (μ_k) under ongoing sliding [15]. While classical models assume μ to be constant, in reality it changes with material combination, surface roughness, temperature, sliding velocity, and environmental conditions [2].

For metal contacts at low humidity, μ typically falls in the range 0.2 to 1.0 [2], depending on oxide films, third-body action, and surface alteration due to wear. Microscopic friction is determined by real contact area A_r (m^2) and interfacial shear strength τ (Pa) [9], these being connected to F_t

(N) via:

$$F_t = \tau \cdot A_r \tag{2.2}$$

As A_r and τ evolve due to asperity deformation, wear, or tribofilm formation, so does F_t, and hence μ is not a constant value. Advance models now capture this evolving behavior, beyond the static assumptions of Amontons–Coulomb theory.

2.3.2 Evolution of the Coefficient of Friction Due to Wear

The coefficient of friction is time-dependent due to surface modifications, wear of materials, and development or breakdown of interfacial films. Under the running-in process, CoF tends to be unstable and highly material and test condition dependent [9].

Peter J. Blau's work [17, 25] explains CoF evolution in terms of stages. CoF may first peak when fresh surfaces are in contact, then reduce as the asperities accommodate and protective films form. Abrupt changes in the CoF curve often signal important transitions such as oxide film breakdown, debris entrapment, or shifts in prevailing wear mechanisms.

In some cases, CoF increases with duration if protective tribolayers break down to a more intense regime like adhesive or abrasive wear. Blau's friction curves as shown in figure 2.16 remain a valuable analysis tool in tribological analysis for comparison.

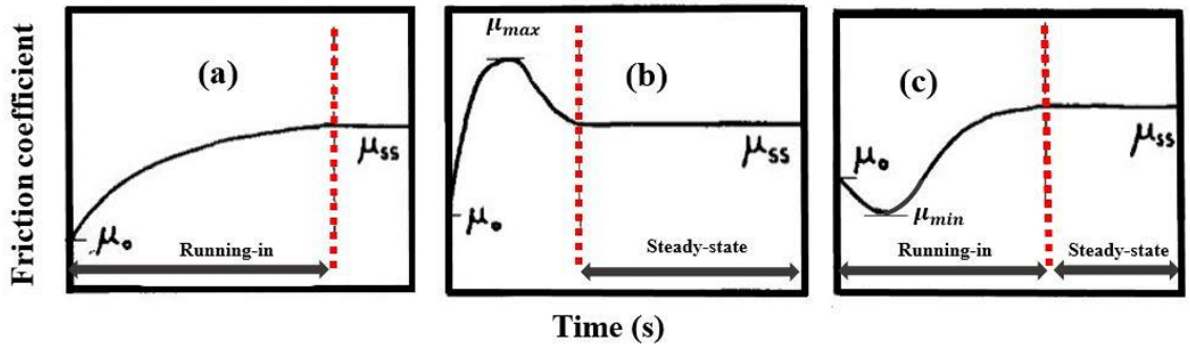

Figure 2.16: Examples of CoF evolution: (a) Transfer layer formation, (b) Surface roughness effects, (c) Compositional changes [25]

In his experiments, Blau also discovered an abrupt rise in CoF from 0.35 to over 1.1 commensurate with the initiation of metallic debris as shown in figure 2.17. The change was a two-body to three-body abrasive wear transition that highlights how debris generation can alter interfacial properties.

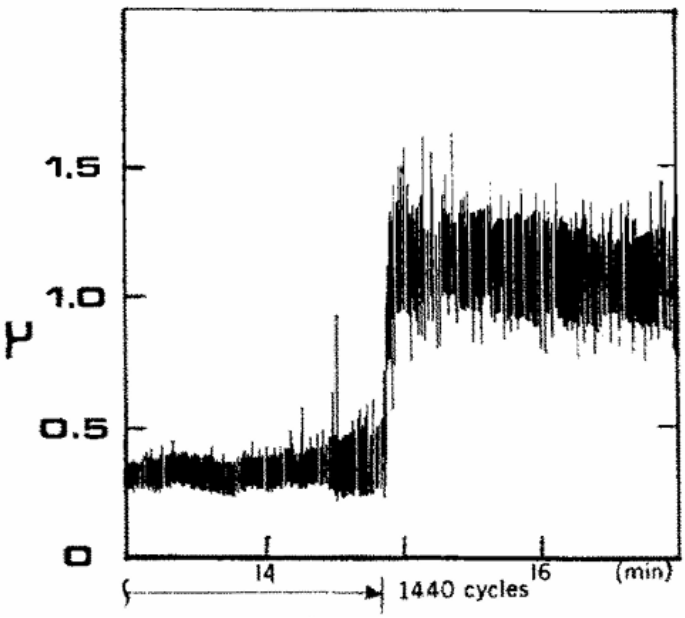

Figure 2.17: Abrupt friction increase due to metallic debris formation [17]

From this standpoint, it can be said that CoF evolution is directly linked to interfacial chemistry, surface roughness, and debris dynamics. Smoother surfaces usually decrease ploughing or abrasive actions, while contamination or peaks of a rough surface can increase friction through micro welding and mechanical interlocking. After the running-in, the CoF can attain steady-state or plateau, marking a wear regime that can be called steady-state. Therefore, interpreting experiments and designing long-life tribological interfaces demand an understanding of this evolution system.

2.4 Modelling of Tribological Contact

As explained in the previous sections, contacting parts apply forces that result in friction, wear, and even failure. Tribological contact modelling is important for understanding how two surfaces interact while they are moving relative to one another. By developing models that mimic interactions, scientists and designers can predict materials performance, and durability, work on design optimization of components, and modelling reduces the costly experiments.

However, tribological modelling is difficult to accomplish, mainly due to real surfaces complexity and variability. Things such as surface roughness, material heterogeneity, and environmental factors impose uncertainties that would hardly be grasped in a single model [5]. Perhaps the worst problem would be that third bodies, like wear debris, step in and change the way surfaces interact with one another in an entirely dynamic manner [9].

Despite these difficulties, continuous advances in computing power and surface characterization techniques have yielded increasingly complex and realistic tribological models. These models now integrate materials science, mechanics, and physics knowledge to provide a more complete understanding of contact phenomena [2] [5].

In the following subsections, wear, contact pressure, and friction coefficient modelling ap-

proaches will be covered, with a comparative critique of their applicability range and limits.

2.4.1 Wear modelling

As mentioned above, wear modeling is unavoidable in predicting material loss and long-term tribological component performance. Over time, numerous models have have been developed, from empirical equations to sophisticated mechanistic and computational models. They differ in the extent of applicability, complexity, and accuracy, and their merits and demerits are briefly listed below.

- In computational techniques such as the *Finite Element Method (FEM)*, the wear depth at each contact node is calculated. Zhihua et al.[26] used this approach well in simulations of disc brakes. However, FEM-based wear prediction is computationally expensive and highly dependent on discretizations quality.
- Mechanistic wear models offer another choice through correlation of the wear with energy stored or released within micro contacts. Son and Molinari [27] developed an energy-based multiasperity model to simulate adhesive wear transitions under a critical length scale d^* (m):

$$d^* = \frac{12\pi\gamma G}{(2-\nu)\sigma_j^2} \tag{2.3}$$

  where γ (J/m^2) is the surface energy, G (Pa) is the shear modulus, ν (dimensionless quantity) is Poisson's ratio, and σ_j (Pa) is the junction stress. This model accounts for the mechanistic mild-to-severe wear transitions as shown in figure 2.18 but is not as appropriate for large-scale applications because it is complex and sensitive to microscale material properties.

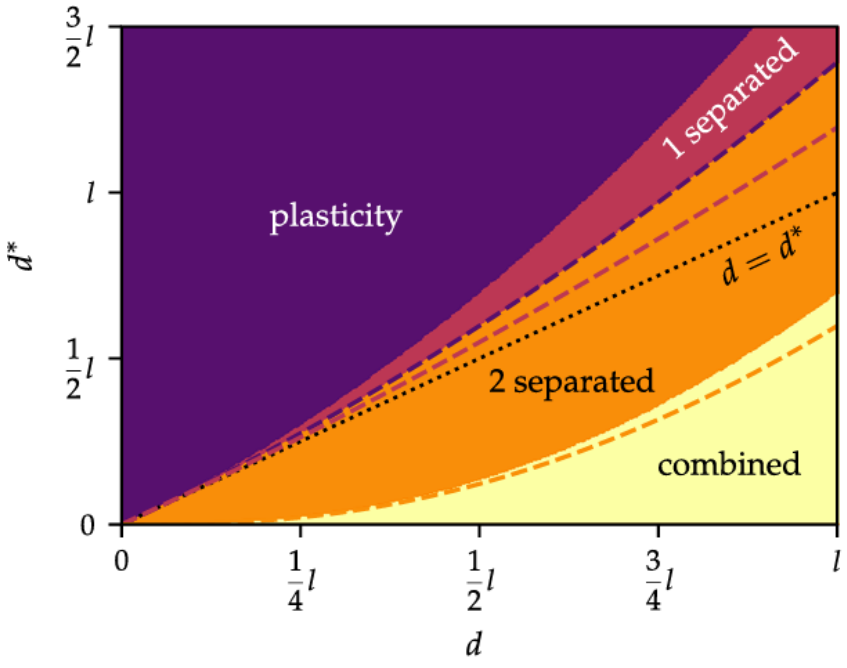

Figure 2.18: Wear map of different cases of wear particle formation under tangentially loaded two micro-contacts [27]

- Archard wear law has been used in different modified versions by scientists along with other theories to make it more reliable. For third-body and abrasive wear conditions, Zhang et al. [22] gave an exponential model that reflects the influence of debris generation:

$$V = \frac{K \cdot F_n}{\alpha} \left(1 - e^{-\alpha L}\right) [mm^3] \tag{2.4}$$

where α (dimensionless ratio) varies with particle volume fraction and size, and L (m) is sliding distance. While this model incorporates the influence of broken particles, its basis on empirical parameters restricts its applicability. For the rough surface case, multiscale models include surface topography explicitly. Varenberg [28] extended Archard's model by including a bearing area function $\phi(h)$ to be expressed as a logistic curve for fitting and dynamic adjustment of the wear rate. Similarly, semi-analytical methods such as the *Winkler wear model* integrate Archard's law over simple contact mechanics. Garcin et al. [29] applied this approach for fretting simulation at the cost of computational efficiency over finer accuracy. While useful, these approaches are usually specialized to contact geometries.

Of these options, the *Archard wear law* [8] is best known for simplicity and longevity. It defines wear volume V (mm^3) as proportional to applied load F_n and sliding distance L, and inversely proportional to hardness H (Pa) of the softer material, with a dimensionless factor K:

$$V = K \cdot F_n \cdot L[mm^3] \tag{2.5}$$

Although it is confined to steady-state conditions and cannot be made to accommodate running-in or varying surface roughness, the Archard law is good enough for the majority of real situations. The simple Archard wear law is used as the best method of choice in this thesis because it provides a simple and computationally efficient mechanism for wear estimation that is preferable to more complex or computationally intensive alternatives. Since Archard's law is in proportion to the applied load and sliding distance, an accurate estimation of local contact pressure is important. The following subsection is thus on how contact pressure is modeled at both macro and micro scale, as this is the foundation for bridging contact mechanics to wear prediction.

2.4.2 Contact Pressure modelling

In tribology, contact pressure modelling finds its foundation, as it corresponds to the deformation of surfaces, real contact areas being formed, friction, and wear behaviors. Due to the multi-scale nature of contact interfaces, from geometry of the bulk body to micro-surface asperities, the method of modelling is conventionally divided into two: macro scale and micro scale contact pressure modelling. Macro scale modelling studies mechanics of load distribution and bulk responses, whereas micro scale modelling focuses on interactions at the level of micro asperities and roughness effects. Following is the in depth details of these two scale contact pressure modelling:

2.4.2.1 Macro Contact Pressure Modelling

An understanding of macro scale contact pressure models assumes two nominally smooth geometries in contact, which are subjected to bulk deformation and load distribution. The foundation is provided by the classical Hertzian contact theory, which gives analytical solutions to idealized smooth elastic bodies [6, 7]. But Hertzian theory is incapable of describing realistic problems such as plasticity and changing geometries. To overcome these limitations, more advanced models have been derived.

Sophisticated techniques such as the *Finite Element Method (FEM)* and the *Boundary Element Method (BEM)* extend the applications of Hertzian theory. Pressure distribution is computed from the application of the equilibrium conditions to discretized volumes using the penalty or Lagrange methods for contact constraints. This enables accurate modelling of changing contact areas, plasticity, and stress fields. Zhihua et al. [26] employed BEM to simulate disc brake contact and predict wear in braking cycles. Even though they were precise, both FEM and BEM are computationally intensive and less preferred to simulate long-term wears. Conversely, *energy-based elastic models*, or mechanistic models, examine deformation by tracing stored elastic energy implicitly rather than computing explicit contact pressures. The models are more physically meaningful but are mathematically intensive and less convenient for scaling up to tribological applications.

As a trade-off between accuracy and computational efficiency, the *Winkler elastic foundation model* has been employed extensively. It approximates the surface as an array of independent vertical springs to reduce computational cost at acceptable accuracy. With progressing wear, the nominal area of contact increases as shown in the figure 2.19 .

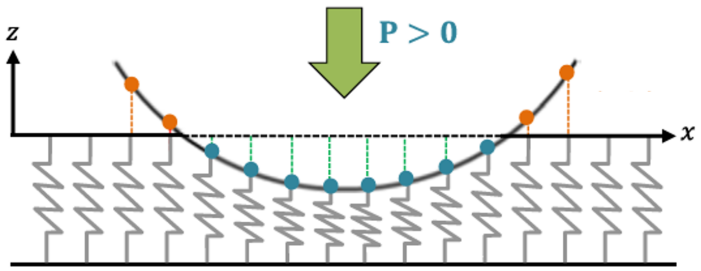

Figure 2.19: Illustration of the Winkler contact model for a 2D cylinder-on-flat contact configuration [29]

With increase in the contact area, more springs at the worn surfaces get activated. Some of these springs can be de-activated due to departure from contact when surface shape changes. This repetitive de-activation and activation of springs enable the Winkler model to replicate variation of contact area and load distribution with wear without losing simplicity. The local pressure is given as:

$$P = K_N \cdot u_z [Pa] \tag{2.6}$$

where K_N (N/m^3) is the normal stiffness per unit area and u_z (m) is the vertical spring deformation. Põdra and Andersson [30] calibrated K_N using Hertzian theory:

$$K_N = C_W \cdot \frac{E^*}{b_H} [N/m^3] \tag{2.7}$$

where E^* (Pa) is the effective elastic modulus, b_H (m) is the Hertzian semi-width, and C_W is a dimensionless geometry-dependent constant. Calibration of K_N by this method allows Winkler's model to compute pressures without losing its simplicity at the macro scale. Winkler model was successfully applied in simulations by Garcin et al. [29] for fretting contacts. Whereas it underestimates maximum pressures at first, precision improves as surfaces settle through wear. Garcin et al. demonstrated computational speedup of up to 300$\times$ over FEM with errors of less than 5% after run-in.

In summary, contact pressure modeling has evolved from simple Hertzian theory to complex FEM, BEM, and energy-based models that each compromise accuracy to varying degrees for computational cost. Of these, the Winkler elastic foundation model offers the best compromise between efficiency and accuracy and is therefore selected in this work as the method of choice for macro scale contact pressure modeling.

2.4.2.2 Micro Contact Pressure Modelling

Micro scale contact pressure models approach contact mechanics at the asperity level, where surface roughness determines the true area of contact, pressure, and deformation.

Greenwood–Williamson (GW) model [31] assumes asperities to be spherical caps with normally distributed height and contact area and load computed under elastic deformation. It is the basis for more advanced models but does not account for plastic deformation.

To correct this shortcoming, the Zhao–Maietta–Chang (ZMC) model [32] incorporates a smooth elasto-plastic transition and more accurately predicts pressure and contact area at moderate to large loads. The Jamari–Schipper model [33] extends this concept with elliptical asperities and experimentally confirmed elastic–plastic behavior. This model selects surface peaks deterministically and scales pressure accordingly and is particularly suited for anisotropic or directional surfaces.

Other approaches, such as the Greenwood–Tripp solution and numerical solutions using the Boundary Element Method (BEM) with Boussinesq–Cerruti equations, are more accurate but at the expense of very large-scale computing facilities, limiting their use for commercial applications.

Another optimum solution for the micro contact pressure modelling is *bearing area curve rough contact model*, which models the real contact area by cutting off surface profiles at a predetermined depth. This method is simple, effective, and of sufficient accuracy for engineering surfaces and is therefore a useful tool for the prediction of contact area evolution with wear.

To summarize, micro-scale contact pressure models provide insightful information regarding local asperity mechanics, where material failure, wear, and friction are triggered. Statistical models like Greenwood–Williamson are easy to compute but more advanced models like ZMC and Jamari–Schipper are more realistic via elastic–plastic transitions. Numerical methods like BEM provide high accuracy at very high computational expense, the optimum solution is the rough contact model which is also used in this study.

2.4.3 Modelling the Evolution of Coefficient of Friction Due to Wear

While it is very much established that the coefficient of friction (CoF) alters with sliding contact, traditional and most contemporary wear models still treat it as a constant input parameter. Re-

searchers such as Sahar et al. [20], Son and Molinari [27], and Varenberg [28] detail complex wear development but retain CoF as static and don't model it as a dynamic state variable. This does enhance computational efficiency but doesn't consider the alteration in CoF due to surface modification and material degradation.

In order to overcome this deficiency, several publications have actually coupled friction and wear.

- Qin et al. [34] investigated the tribological behavior of TiN-coated surfaces and proposed a two-term model

$$\mu = \mu_a + \mu_p \tag{2.8}$$

where μ_a represent the adhesive action and μ_p accounts for ploughing. They proposed an experimentally driven expression to better describe the role of the trapped debris:

$$\mu_{pc} = N_{pc}\rho^{\lambda}\mu_{pc1} \tag{2.9}$$

In this model, ρ is the normalized wear particle density, μ_{pc1} is the ploughing friction from a single particle, and all of the parameters like μ_{pc1}, ρ, and scaling behavior are derived from experimentally determined debris morphology, density, and wear track shape. This contribution contributes to the total friction only when ρ is larger than a critical value, which indicates large-particle entrapment. The model successfully replicates friction formation via wear processes, following high early CoF due to the ploughing caused by debris, followed by stabilization as the surface smooths and effects of debris diminish. This behavior is best exhibited in the plot of CoF against time in figure 2.20, with simulation closely tracking experimental trend across different loads, confirming the ability of the model to simulate debris-activated frictional behavior but main limitation is that, it is highly dependent on the experimentally collected data as model is designed by empirical fitting of data.

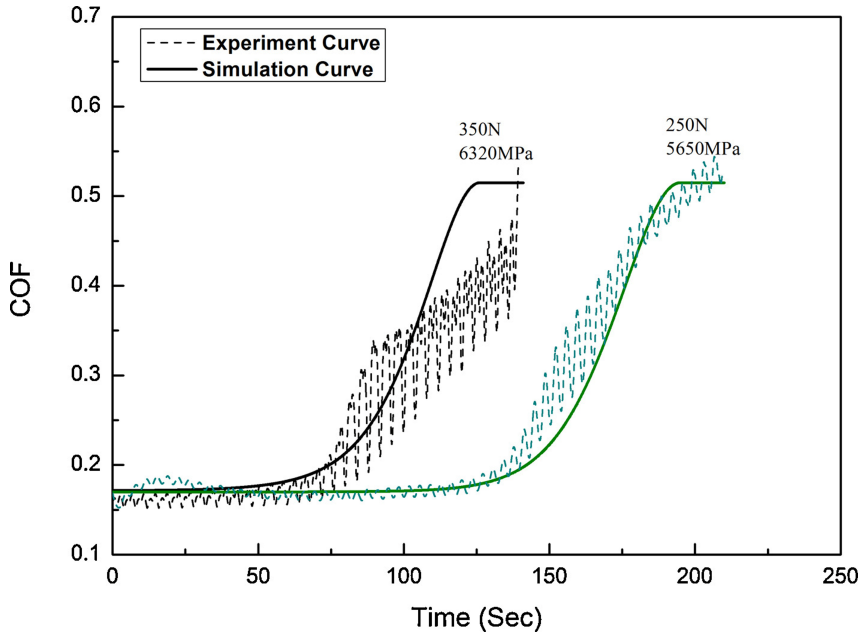

Figure 2.20: Simulative and experimental fiction coefficient curves of the sample under 250 N and 350 N [34]

- Hu et al. [35] proposed an interactive friction model for aluminum–steel sliding with CoF evolution through the development of a transfer layer. Though it considers adhesive wear phenomena and dynamic material coupling, being empirical, it doesn't have spatial resolution along the interface and is not applicable to non-uniform geometries.
- Tian et al. [36] introduced a data-centric approach combining FEM and DNNs to forecast CoF evolution under acoustic emissions. It can be used for real-time monitoring with reasonable accuracy but bypasses physical wear mechanisms and relies significantly on the quality of training data. Its performance in unseen conditions or other material combinations is unknown.
- Yang et al. [37] developed a semi-empirical galling model under non-uniform contact pressure, attributing the increase in CoF to roughening, adhesion, and third-body dynamics. The model, however, assumes uniform pressure and does not consider microscale evolution and local debris impact, limiting predictability in heterogeneous or transient contacts.

These findings indicate a shift in strategy in friction modelling to account for the dynamic nature of contact interfaces. Later work is emphasizing that friction cannot be treated as an independent parameter, but that it must be linked to wear-induced alterations, contact morphology, or material rheology.

Another simple approach is to relate the coefficient of friction to the true contact area varying under wear, junction shear strength, and applied normal load:

$$\mu = \frac{\tau \cdot A_r}{F_n} \tag{2.10}$$

In this expression, τ is shearing strength at asperity junctions, A_r is the true area of contact formed as surfaces wear, and F_n is the applied load. This approach incorporates the effect of surface evolution via A_r, and is computationally accessible and physically intuitive. It avoids the complexity of multi-term phenomenology, but retains the wear-friction coupling through micro-scale contact evolution to macroscopic friction response.

2.4.4 Comparison of Modelling Approaches

In order to make a comparative assessment of the tribological friction and wear models currently available, a structured set of assessment criteria has been established. Table 2.1 comprises of this comparison across five primary set of criteria: (i) type of wear addressed, (ii) wear theory, (iii) evolution of contact pressure, (iv) explicit CoF evolution due to wear, (v) surface roughness inclusion, and (vi) experimental validation. Presence/absence of each of these characteristics in each model is assessed. Green cells represent elements of modelling that have been thoroughly investigated in previous research. Cells with "✗" represent elements that needs to be researched further, representing potential research gaps.

The table highlights that a number of researches fails to add the models of changing CoF as a result of wear and surface roughness, which are crucial in capturing real tribological behavior. A number of studies also have no experimental validation, reducing confidence in their applicability to practice. Furthermore, while the Archard wear model is most widely applied, it is often applied without regard to changing contact pressure or changing wear mechanism, leading to oversimplification.

The comparative context demonstrates the fragmented nature of contemporary modelling strategies and emphasizes the demand for more synthesized models that reflect the dynamic, multi-dimensional character of wear phenomena, particularly with complicated loading and contact conditions. Filling these listed research gaps can appreciably advance the physical realism, predictive capability, and engineering applicability of future tribological simulations.

Table 2.1: Comparative summary of wear and CoF modelling approaches

Reference Details	Wear Type	Wear Theory	Evolving Contact Pressure	Evolution of CoF due to Wear	Roughness Inclusion	Experimental Validation
Pōdra & Andersson (1997): Wear Simualtion with the Winkler surface model [30]	Undefined	Archard Wear Model	✓	✗	✗	✗
Guojia Ma et al. (2015): The friction coefficient evolution of a TiN coated contact during sliding wear [34]	Adhesive and Abrasive	Empirical fit	✗	✓	✗	✓
Y. Hu et al. (2019): Development of an interactive friction model to predict aluminum transfer in a pin-on-disc sliding system [35]	Abrasive and Oxidative	Archard Wear Model	✗	✓	✓	✓
Sahar et al. (2020): Experimental and Numerical Study of the Running-In Wear Coefficient during Dry Sliding Contact [20]	Adhesive	Archard Wear Model	✓	✗	✓	✓
Son and Molinari (2021): Adhesive Wear Regimes on Rough Surfaces and Interaction of Micro contacts[27]	Adhesive	Mechanistic Wear Model	✓	✗	✓	✗
Varenberg (2022): Adjusting for Running in: Extension of the Archard Wear Equation [28]	Undefined	Archard Wear Model	✓	✗	✓	✓
Garcin et al. (2022): Fretting wear modelling of 3D and 2D Hertzian contacts with a third-body layer using a Winkler elastic model [29]	Fretting	Archard Wear Model	✓	✗	✗	✓
Zhihua et al. (2022): Wear calculation and life prediction model of disc brake based on elastoplastic contact mechanics [26]	Adhesive + Abrasive	Archard Wear Model	✓	✗	✓	✓
Yang et al. (2022): Experimental and modelling study of interaction between friction and galling under contact load change conditions [37]	Adhesive	Archard Wear Model	✓	✓	✗	✓
Wattel et al. (2024): A story of two transitions: From adhesive to abrasive wear and from ductile to brittle regime [38]	Adhesive → Abrasive	Mechanistic Wear Model	✗	✗	✗	✗
Tian et al. (2025): Real-Time Prediction of Wear Morphology and Coefficient of Friction Using Acoustic Signals and Deep Neural Networks in a Tribological System [36]	Adhesive	Archard wear equation + Deep Neural Network	✗	✓	✗	✓
Ciavarella (2025): Some Remarks on a Recent Wear Theory [24]	Fatigue	Mechanistic Wear Model	✓	✗	✓	✗

Chapter 3

Methodology

This chapter presents the methodology put into the practice for the study of CoF evolution due to wear in dry sliding condition. Addressing the pre-existing gaps in literature, the methodology relates tribological testing at the experimental level with the modelling frameworks.

3.1 Scientific Research Gap

As it has been discussed in previous chapter that many research studies have been done on wear and friction modelling, but most of the models take CoF as a constant and fail to treat its evolution due to surface degradation. Such models lacks the coupling of wear evolution to CoF behaviour, and sometimes these studies do not incorporate contact pressure modelling or roughness effects. This thesis addresses these research gap by developing integrated models supported by experiment, connecting together variables such as contact pressure, wear, and the evolution of the CoF.

3.2 Experimental Test

This research study started with a systematic experimental study to analyze the tribological behavior of a material pair under dry sliding condition. One of the main objective of this research was to investigate whether increased sliding speed affects wear volume and evolution of the coefficient of friction (CoF). One of the main aspects was to acquire the wear coefficient K under dry test condition and understand whether wear is controlled by sliding distance rather than sliding speed. Confirmation is required, as in applications at specified speeds, any attempt to accelerate the test must ensure that K is independent of sliding speed in the range of this study.

The experimental investigation yielded vital information and data i.e. wear rates, surface evolution, and CoF trends, that were subsequently employed to guide and calibrate the modelling framework. The experimental tests involved material preparation, tribological test setup, and post test surface analysis.

3.2.1 Materials and Sample preparation

Material pair utilized in this experimental tests are chosen due to their industrial importance as they represent realistic tribological contact conditions found in engineering components. Following table 3.1 represent the material pair and dimensions.

Disc samples of stainless steel as shown in figure 3.1 were prepared by a three-tooth milling cutter (under lubricated conditions) in two-step milling operation which are discussed in table 3.2 with the set of parameters to achieve surface roughness (R_a= 3μm) close to that in the most common

Table 3.1: Material pair & its dimensions

Material	Geometry	Dimensions
Stainless Steel	Disc	Diameter: 30 mm, Thickness: 15 mm
Inconel alloy	Spherical Ball	Diameter: 6 mm

industrial components. The Inconel alloy spherical ball was pre-polished by the manufacturer and was used after a simple cleaning procedure.

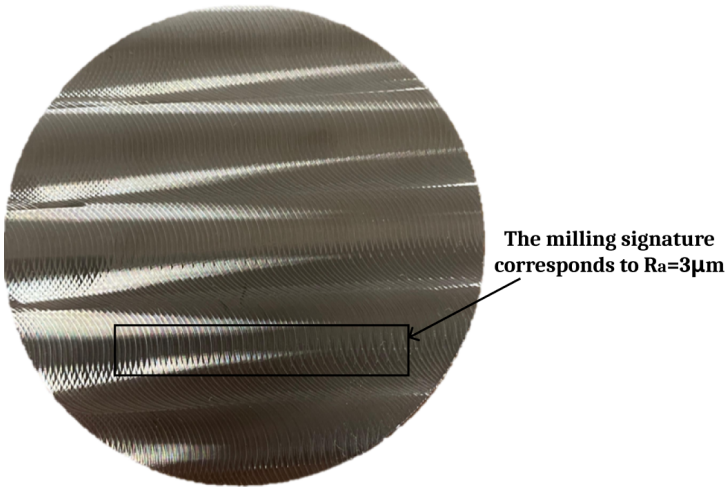

Figure 3.1: Prepared stainless steel disc sample

Table 3.2: Milling parameters for stainless steel disc preparation

Operation	Cutting Speed (m/min)	Feed Rate (mm/tooth)
Roughing	120	0.25
Finishing	80	0.65

To validate the surface roughness value close to R_a= 3μm close to most common in many engineering components, surface was analyzed with a contact profilometer as well as an Focus Variation Microscope (Alicona), methodology adopted for the measurements is discussed in detail in the section 3.2.3. Before testing, both samples disc and spherical balls were cleaned to remove contaminants. Cleaning was done by ultrasonic cleaning in an ethanol bath for 3 minutes, followed by rinsing in distilled water and drying with hot air blower.

3.2.2 Tribological Test Setup

After cleaning the samples, to perform the tribological test, both specimens were mounted on an Rtec Multi-Function Tribometer with a ball-on-flat disc reciprocating setup as shown in figure 3.2 where a spherical ball is mounted in a stationary holder which comes in contact with a reciprocating stainless steel disc mounted on a transnational X-Y stage as shown in the complete test setup configuration figure 3.3. This setup was chosen to replicate unidirectional sliding contact conditions typically encountered in mechanical assemblies.

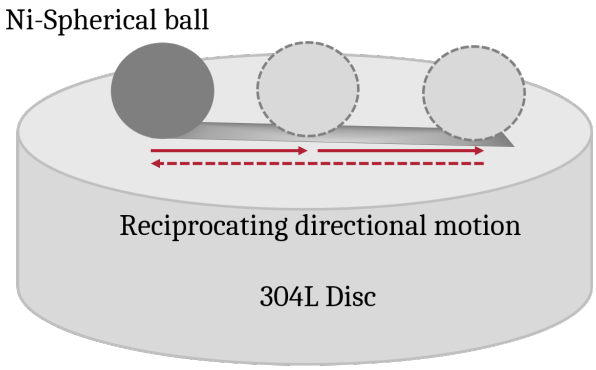

Figure 3.2: Reciprocating configuration to be used in test

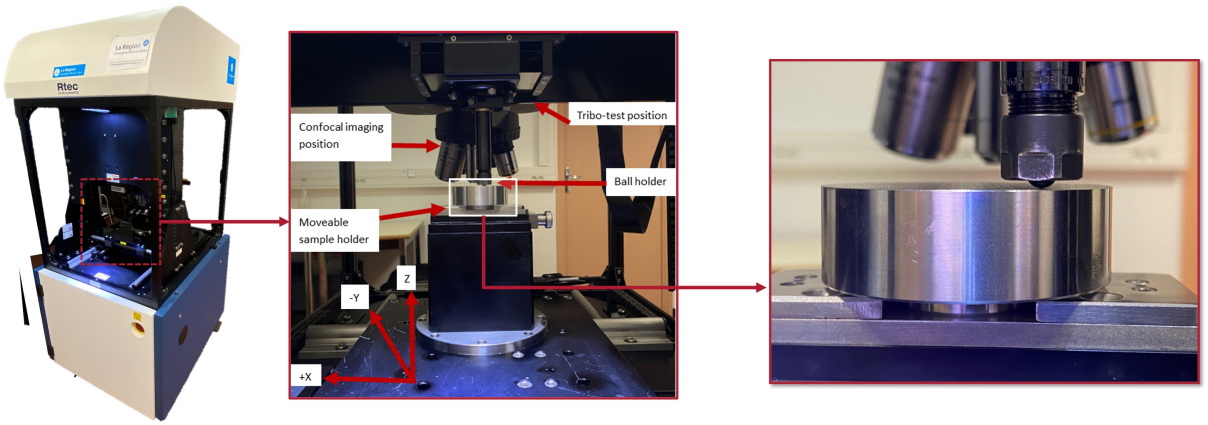

Tribo test setup on Rtec instrument

Tribo test position with sample placement and Confocal microscope position

Nickel ball in contact with the 304L disc leading to reciprocating sliding

Figure 3.3: Tribological test setup

Before testing, the system was subjected to a typical three-step protocol:

- Calibration of displacement sensors, so confocal microscopy can be utilized to capture before and after wear test topography.
- Placement and alignment of samples as shown in figure 3.3.
- Running of the test program via Rtec control interface, command of velocity, load and sliding distance parameters was defined at this stage.

Through the Rtec control interface, the reciprocating motion of the disc was controlled along the X-axis, allowing linear back-and-forth sliding motion at a predefined stroke length, load and velocity. Total number of back-and-forth motions are set in a way to have the same sliding distance for all varying velocities. Following table 3.3 shows the constant parameters in the experiments: Four different velocities were selected as shown in table 3.4 to explore a broad range of contact conditions, from mild to relatively aggressive sliding. Test durations were adjusted accordingly to

Table 3.3: Constant parameters for tribological tests

Parameter	Value
Force (N)	8
Back and forth motion distance (mm)	60
Number of back-and-forth motions	40

ensure a constant sliding distance, following the relation:

$$\text{Test Time (min)} = \frac{\text{Total Sliding Distance (mm)}}{\text{Velocity (mm/min)}}$$

Table 3.4: Variable parameters for tribological tests

Velocity (mm/min)	Test Time (min)	Sliding Distance (mm)
10	240	2400
20	120	2400
50	48	2400
100	24	2400

This test design provides uniform wear tracks and controlled contact conditions, enabling accurate analysis of the coefficient of friction (CoF) and wear behavior over time for all samples. This approach allowed for direct comparison of the frictional response and wear evolution across varying velocities under identical load and contact conditions. During the test, friction force, displacement, and normal load were measured continuously at high frequency, allowing real-time monitoring of CoF evolution. These data served as the foundation for both experimental analysis and model calibration in the following sections.

3.2.3 Surface and Wear Characterization

This part of methodology is focused on characterization techniques applied in the research work, first after sample preparation of stainless steel disc, roughness measurements are investigated and stored using two analyzing techniques profilometer and focus variation microscope. Table A.1 in appendix 5 gives the parameters and standards for analyzing surface roughness using a profilometer and focus variation microscope. It discusses the profile and length of sampling, and the cutoff value employed to determine the spatial frequency of surface features to be measured. The table also references significant ISO and ASME standards employed to guide such measurements for conformity to globally adopted procedures. This is to achieve precise and standard measurement of surface roughness, a necessity to determine the quality and performance of manufactured parts.

Surface and wear characterization was performed using a set of optical and electron microscopy techniques to analyze both the stainless steel disc and Inconel alloy ball after tribological testing.

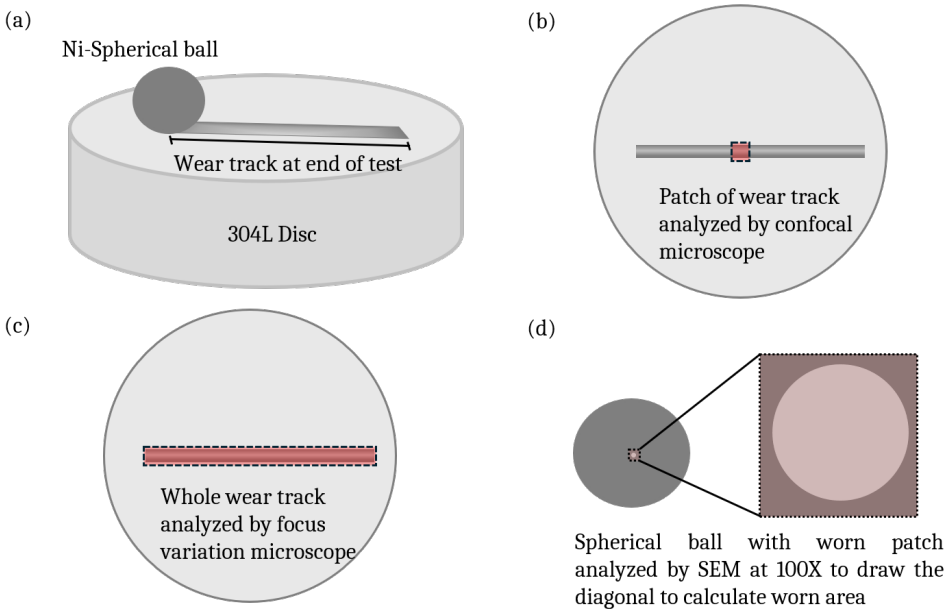

Figure 3.4: (a) 3D view of sphere on disc after the completion of test, (b) 2D view of disc with wear track showing the patch analyzed by confocal microscope, (c) 2D view of disc with wear track showing the whole track analyzed by focus variation microscope, (d) Spherical ball with worn patch analyzed by SEM at 100X

For the disk samples, wear track morphology and surface topography were characterized mainly by confocal microscopy which is integrated in the Rtec tribometer [1] set up. In addition, a Focus Variation Microscope[2] was used. These systems allow for three-dimensional reconstruction of the wear tracks at high resolution. Confocal imaging was carried out right after the test, it scan the surface at 20X objective on a small region of wear track as shown in figure 3.4 (b), whereas focus variation microscopy analyzing were used for more accurate post-test analysis for the complete wear track at 20X objective as shown in figure 3.4 (c). All topography information of the wear track were processed on with MountainsMap® software, under which standardized analysis was performed. From such analysis, wear depth profiles, and volume loss, were examined and quantified, procedure for this analysis has been given in appendix 5 (figure A.1).

For Inconel alloy balls, precaution was taken to avoid contamination or artifacts due to handling. Post-test surface of sphere was examined by Scanning Electron Microscope (SEM) to capture high-resolution images of the contact area. The degraded area on both balls was defined on the grounds of variations of contrast as shown in figure 3.4 (d), and the height of the worn patch was determined by constructing two perpendicular diagonals on the patch, as illustrated in appendix 5 (figure A.2), and from the following geometric relationship:

$$h_{\text{worn}} = R_{\text{sphere}} - \sqrt{\left|R_{\text{sphere}}^2 - a^2\right|}[m] \tag{3.1}$$

where R_{sphere} is the sphere's radius and a is a mean of the two diagonals. This multi-instrument

[1] MFT 5000
[2] Alicona InfiniteFocus V2

approach yielded consistent characterization of wear tracks and accurate quantification of contact wear and damage volumes on both materials, allowing for a valid correlation between modelling endeavors and experimental phenomena that will be discussed in the following sections.

3.3 Modelling Framework

Based on the gap in research highlighted, this study develops a tribological modelling structure consisting of three key elements: **contact pressure modelling**, **wear modelling**, and **evolution of the coefficient of friction (CoF)**, as illustrated by figure 3.5. Unlike previous studies, which discussed these mainly in isolation, the present work integrates these into one system. This blended approach is the foundation for the method presented herein to measure tribological performance under dry sliding conditions.

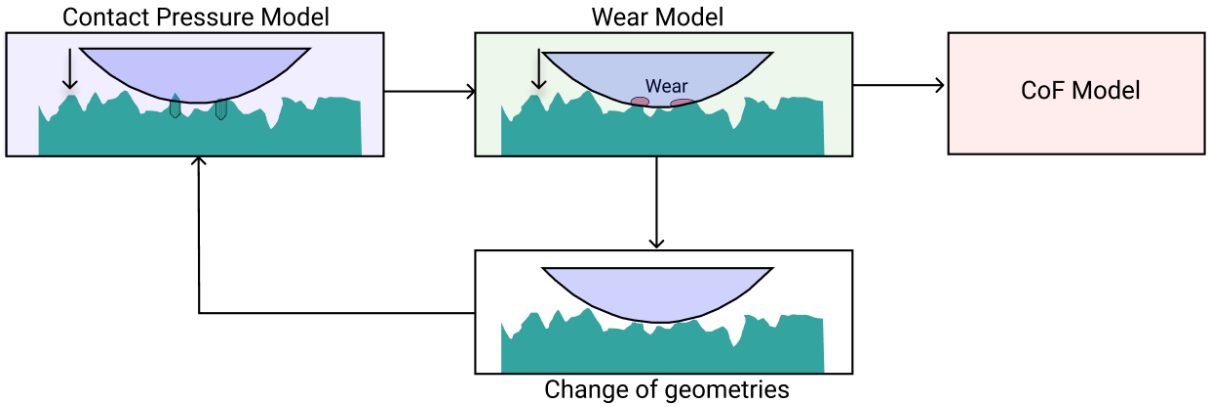

Figure 3.5: Essential components of a tribological model: contact pressure modelling, wear modelling, and CoF evolution

Although the above items give a sound starting point, the one basic issue remains: *how to incorporate surface roughness into the modelling formulation?* Surface roughness plays a vital role in both the real contact area and the occurrence and progression of wear, especially with dry contact. However, conventional contact pressure models operating at the macroscale cannot treat micro-scale topography features, which restricts their ability to model real contact behavior.

To overcome this limitation, the present research extends the modelling approach with a two-scale formulation in which contact pressure is evaluated at the macro- and micro-scales, pressure is then applied to wear modelling to calculate the worn depth and capture the evolution of geometry, based on the contact area CoF is modelled. This methodological contribution is central to the current research and enables a more accurate representation of the interaction among contact mechanics, surface roughness, and wear evolution.

3.3.1 Modelling Output

The overall output target of the models is to track the evolution and development in the wear behavior, pressure distribution, and the coefficient of friction over time. The models can generate

a variety of key outputs that represent an informed foundation of understanding the tribological interactions between the two components.

The first significant output is the coefficient of friction (CoF), which is monitored throughout the simulation. The CoF is measured in terms of time and sliding distance, and plotted in terms of time-dependent curves.

A second significant output is the pressure distribution in the contact area. This distribution of pressure is necessary in achieving the local conditions of contact in wear. The model determines the pressure distribution at each iteration, and the result is stored and plotted as 3D, 2D, and curve plots. These distribution curves and pressure maps show the pressure variation within the contact region and provide useful information for wear behavior under various conditions of load.

The wear distribution on the sphere and the disc is also a necessary output. Local wear at every iteration is calculated by the model under the applied load and pressure distribution. Wear on the sphere and disc over a period of time and sliding distance is tracked and depicted using 3D surface maps. Wear evolution along the entire sliding distance is also plotted in 3D, 2D, and curve plots that depict topographical variations in the contact region and distinctly represent material loss on both surfaces.

Apart from the local wear, the models also accumulate the global wear volume of the sphere and disc during the entire simulation period. The cumulative wear is plotted against time to indicate the cumulative amount of material loss throughout the process of wear.

These outcomes, derived by means of multiple iterations, present a comprehensive view of the wear and friction phenomenon, enabling material behavior during simulation to be more comprehended.

Chapter 4

Results and Discussion

This chapter provides both computational models development and experimental study result analysis. The workflow of cahpter is as follow: first, the experimental results obtained from surface analysis and tribology tests are presented. Next, development of the numerical models is described, followed by the corresponding results. Finally, experimental results comparison with numerical results are presented, including, discussions regarding model performance, limitations, and implications for tribological behavior.

4.1 Experimental Results

First it is necessary to validate that surface roughness from the milling operation is approximately R_a= 3μm, following figure A.3 in appendix 5 shows the results of Ra by profilometer and by focus variation microscope.

As explained in section 3.2.2, tribological tests were performed at four different velocities, as detailed in table 3.4. The following figure 4.1 shows the disc with wear tracks created by these velocities, with the corresponding speeds marked in front of each track. These tests provided valuable insights into the evolution of the coefficient of friction (CoF), wear volume, and surface morphology of the materials under dry sliding conditions. After analyzing the data obtained from the Rtec tribometer during the tests, the following results were observed.

The normal force remained constantly at $8\,\mathrm{N}$ for all the test velocities, with no significant fluctuations as shown in appendix 5 (figure A.4). This constancy is a witness that the Rtec Tribometer was properly calibrated and that the tests were carried out under well-controlled experimental conditions.

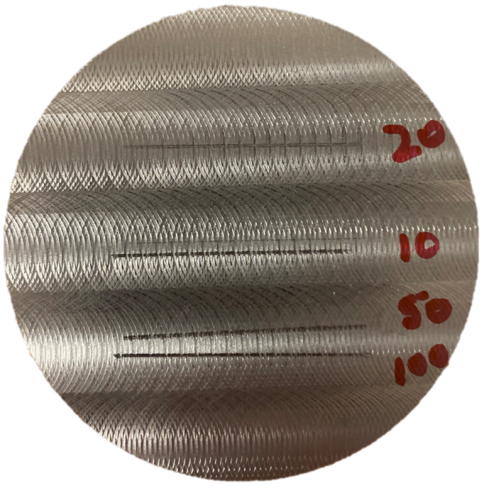

Figure 4.1: Stainless steel disc with wear track at four different velocities

The evolution of the coefficient of friction (CoF) was studied in terms of both cumulative sliding time and cumulative sliding distance for each test velocity. Figure 4.2 graphs the CoF as a function of cumulative sliding time for disc sample "S1" at four sliding velocities: 10 mm/min (red), 20 mm/min (blue), 50 mm/min (green), and 100 mm/min (orange) (these curves are obtained after applying a filter on data to eliminate the noise). At higher sliding speeds, the same total sliding distance was achieved in a shorter duration of time, which also means at a higher frequency of back-and-forth motion of the spherical counterbody. Despite these differences in time scales, the CoF variation was small, and all the curves could reach almost the same peak value. The arrows in the figure indicate that the curves have to be extended up to the total sliding distance for comparison. These results suggest that, while sliding time controls the rate of completion of a given distance, it is not a controlling parameter for comparing CoF development, which more directly relates to cumulative sliding distance.

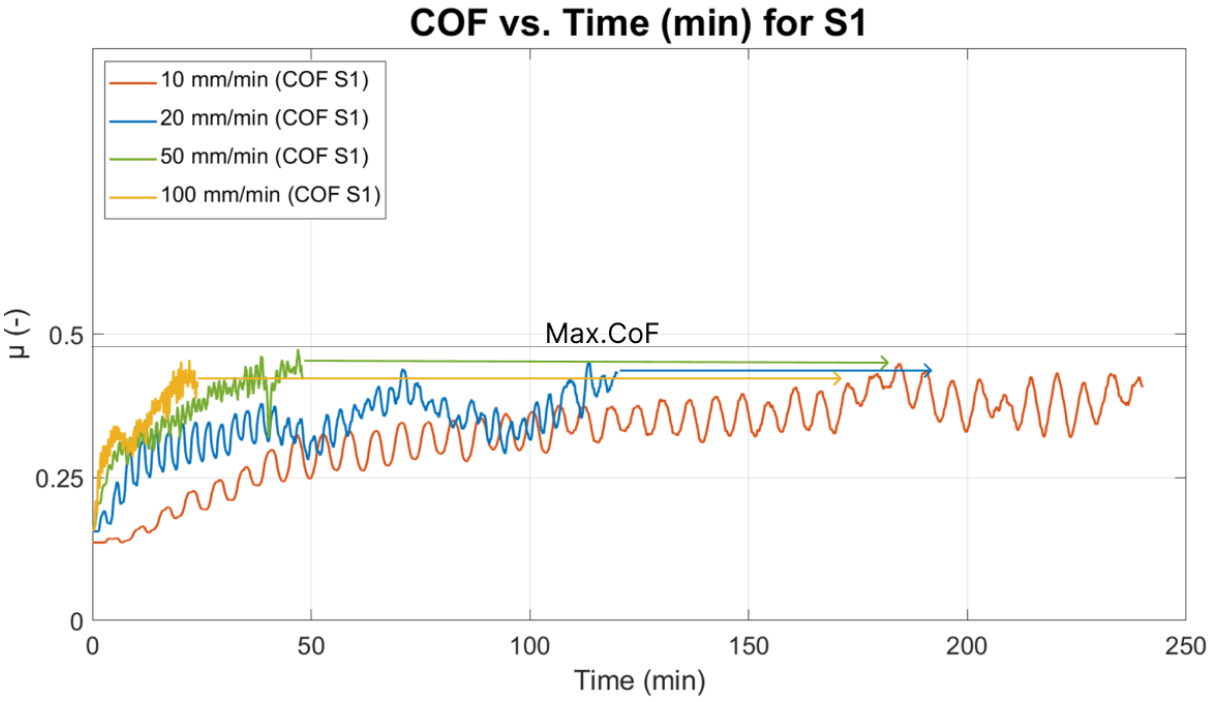

Figure 4.2: CoF for different velocities with varying sliding time

Figure 4.3 presents the CoF plotted versus cumulative sliding distance for the same test conditions. The sinusoidal form of the curves is a consequence of the reciprocating motion of the spherical counterbody, with each direction reversal resulting in an oscillation in friction as the ball decelerates, stops, and then accelerates in the opposite direction. The CoF increased rapidly at the beginning of the tests because of asperity deformation and removal from the surface. As sliding persisted and the surfaces smoothened, CoF changes became insignificant and the values stabilized, increasing only at a slow rate. While higher velocities influenced the initial CoF, no doubt due to abrupt surface topography changes on first contact, the overall CoF evolution had no visible, consistent velocity dependence on sliding velocity. This indicates that CoF behavior is dominated primarily by the reciprocating motion and wear dynamics of the contact rather than being dictated by sliding velocity

alone.

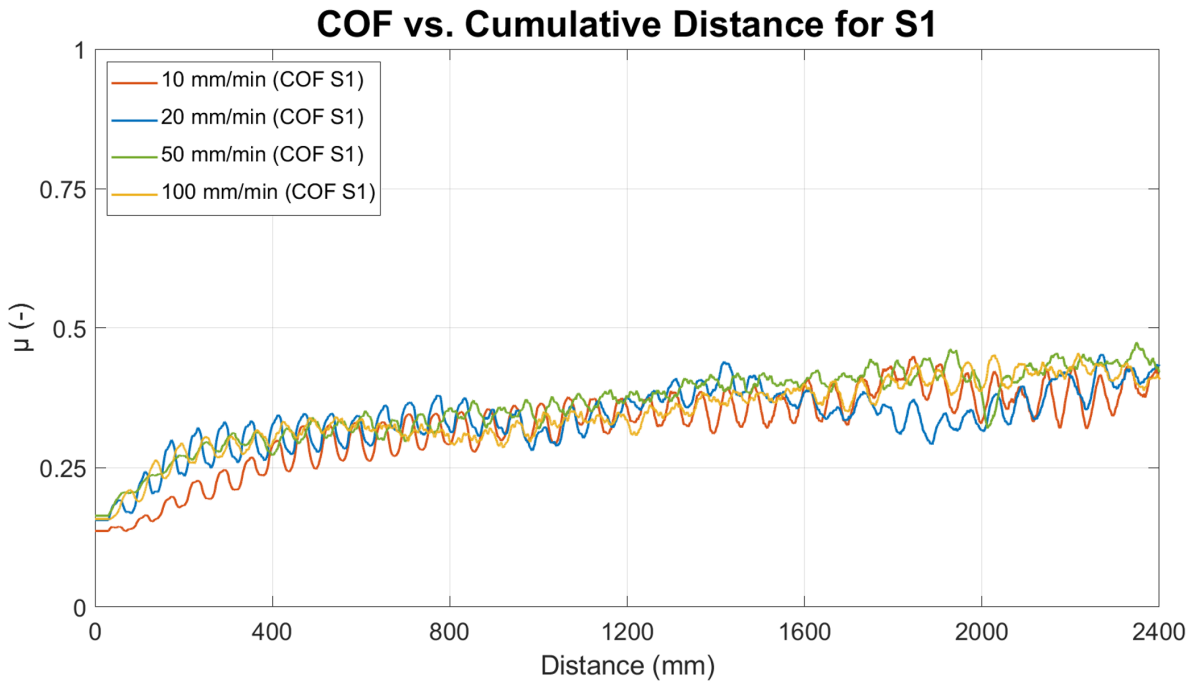

Figure 4.3: CoF for different velocities with cumulative sliding distance

Since the normal force remained the same for all the tests, thus the contact pressure on the interface was the same as well. Sliding velocity was the only adjustable in the system and regulated the PV product (Pressure $\times$ Velocity) as outlined in Section 2.2.2. For each of the test conditions, the PV product was then compared with a classical steel wear regime map [23], which is shown in figure 4.4. The plot indicates that each of the four combinations of PV lies in roughly the same regime of wear (mechanical wear). The plot is also useful for evaluating the generated power at sliding contact and, as a result, the total dissipated energy within the system.

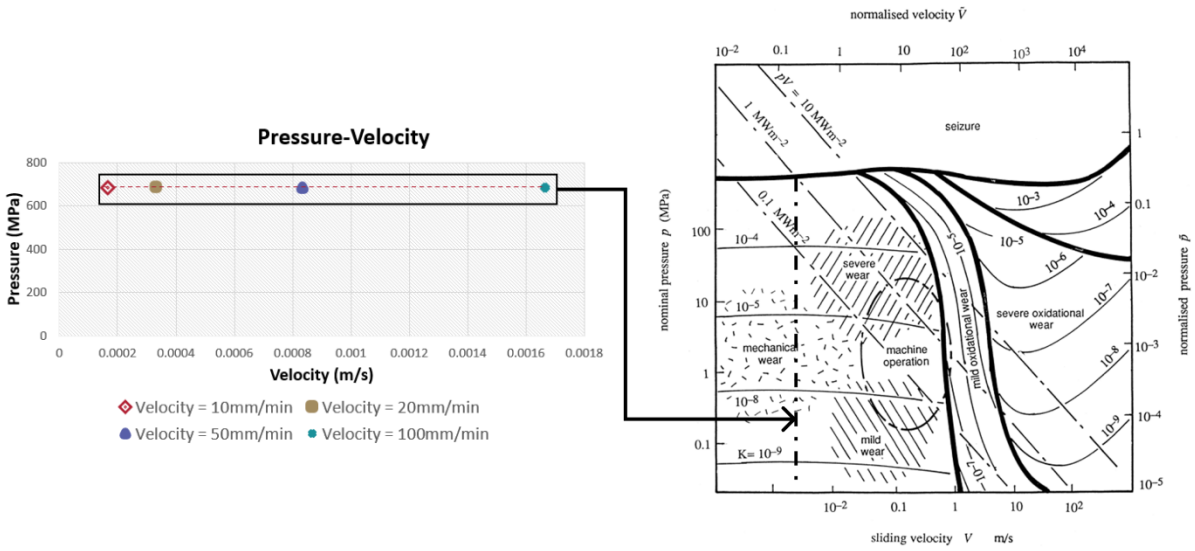

Figure 4.4: PV wear map to observe the effect of velocity and pressure on the type of wear regime

With the rise in sliding velocity, the duration for which the same sliding distance is covered is reduced due to the reason that more distance is traversed in a unit time. Therefore, although the velocity was altered, the total energy consumed is relatively unchanged as shown in appendix 5 (figure A.5). This means wear is not too sensitive to sliding velocity in situations where total sliding distance remains unchanged.

Post-test characterization of the spherical counterbody was conducted by SEM as explained in section 3.2.3. Contact area on the nickel ball varied from sample to sample but was not correlated with test velocity. The percentage of iron particles adhered to the ball surface varied between 31% and 38%, so sliding velocity did not control iron material transfer (appendix 5 figure A.6).

Figure 4.5 presents the volume of wear for the spherical ball at the four test speeds. No detectable influence of sliding speed on volume of wear was observed, further supporting the conclusion that, with constant sliding distance and load, velocity has minimal influence on the wear behaviour overall.

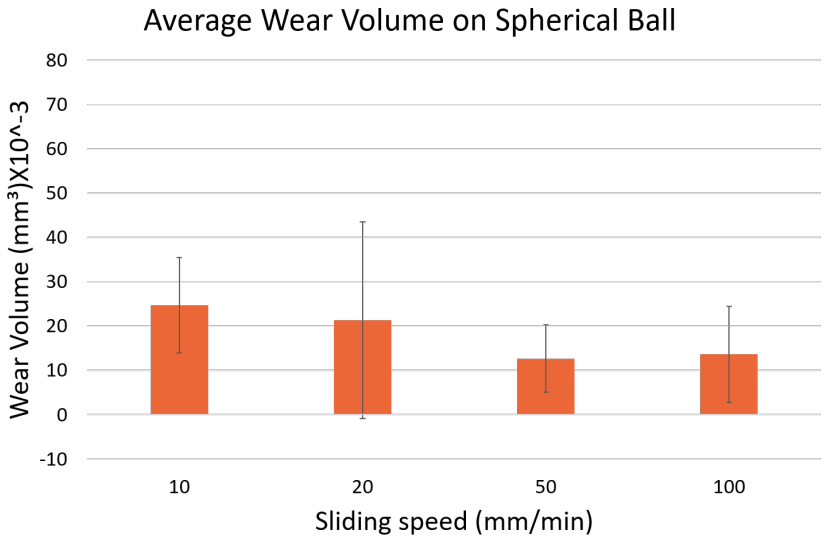

Figure 4.5: Calculated wear volume on the spherical ball

For stainless steel disc samples, as outlined in section 3.2.3, two characterisation techniques were used to measure wear volume. The result given by both methods is presented in figure 4.6. Confocal microscopy analysis was performed on a thin segment of the wear track with a width of approximately 0.6 mm. The volume of wear was determined by multiplying the cross-sectional valley area by the total track length. The technique overestimates wear volume as it also records surface features such as the milling signature. This is in contrast to using focus variation microscopy to the entire 30 mm wear track, and in doing so provided a direct volumetric measurement. This method eliminates the process of extrapolation in the confocal method and gives a more realistic measurement of the wear volume.

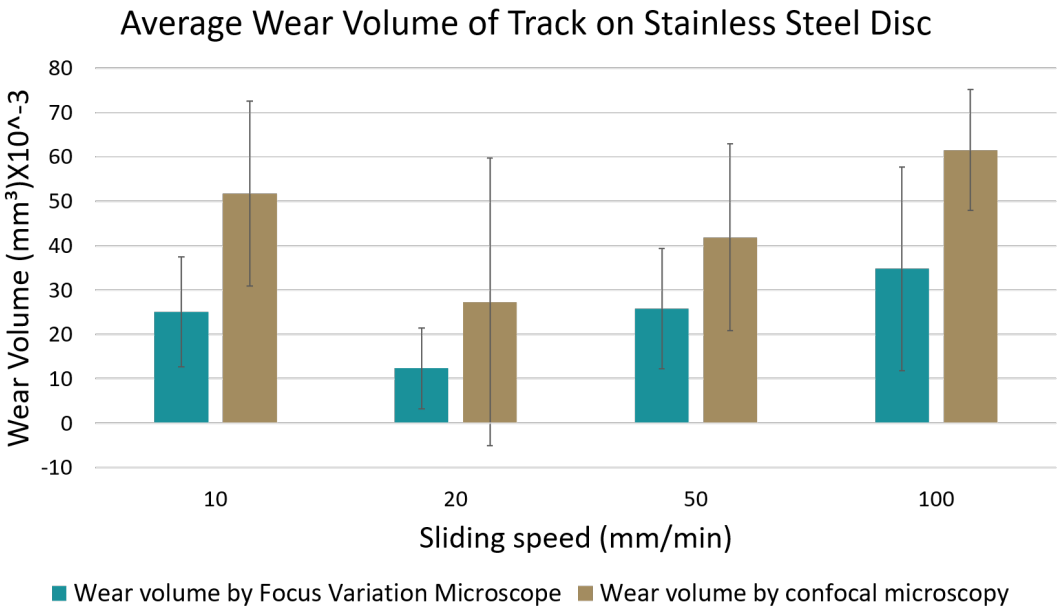

Figure 4.6: Wear volume on stainless steel disc using two analysing techniques with standard error bars

Wear coefficients are a principal input to the numerical wear modelling. From the measured wear volumes of both nickel sphere and stainless steel disc, the wear coefficient (in units of $\mathrm{mm}^3 \cdot \mathrm{N}^{-1} \cdot \mathrm{m}^{-1}$) for both materials ($K_{\text{Sphere}}$ and K_{Disc}) was calculated using Archard's wear law (equation 2.5). The results are summarized in table 4.1.

Material and Analysing technique	**Wear Coefficient ($\mathbf{mm^3.N^{-1}.m^{-1}}$)**
For spherical ball (Analyzed by SEM)	9.4×10^{-4}
For disc (Analyzed by focus variation microscope)	12.7×10^{-4}
For disc (Analyzed by focus confocal microscopy)	23.7×10^{-4}

Table 4.1: Wear Coefficient Values

From the results, some important conclusions can be made:

- Wear is random by nature and no trend in the coefficient of friction (CoF) is found on varying the sliding velocity.
- Tribological testing can be speeded up to reduce analysis time and cost without sacrificing wear assessment.
- K for the ball is less than the K for the stainless steel disc in dry contact.

4.2 Models Development

Following sections presents the methodology of development of V1, V2 and V3 versions of models with the results and comparison for each version of models and experiment, most important results are contact pressure evolution, wear volume and worn geometry, and CoF evolution.

4.2.1 Computational Approaches and Initialization

As stated earlier, models are developed at two scales level as explained below:

- **Macro-scale model:** A tribological model based on the Winkler elastic foundation that calculates global pressure distribution, wear evolution by archard equation, and CoF evolution with time, assuming a nominally smooth interface. The following figure 4.7 is the flowchart illustrating the steps that have been followed in order to develop the model.
- **Micro-scale model:** A micro scale model with contact pressure model that uses surface roughness (through the bearing area curve) explicitly to calculate the real contact area, local pressures, and their effects on wear and CoF development. The following figure 4.8 is the flowchart illustrating the steps that have been taken to create the model.

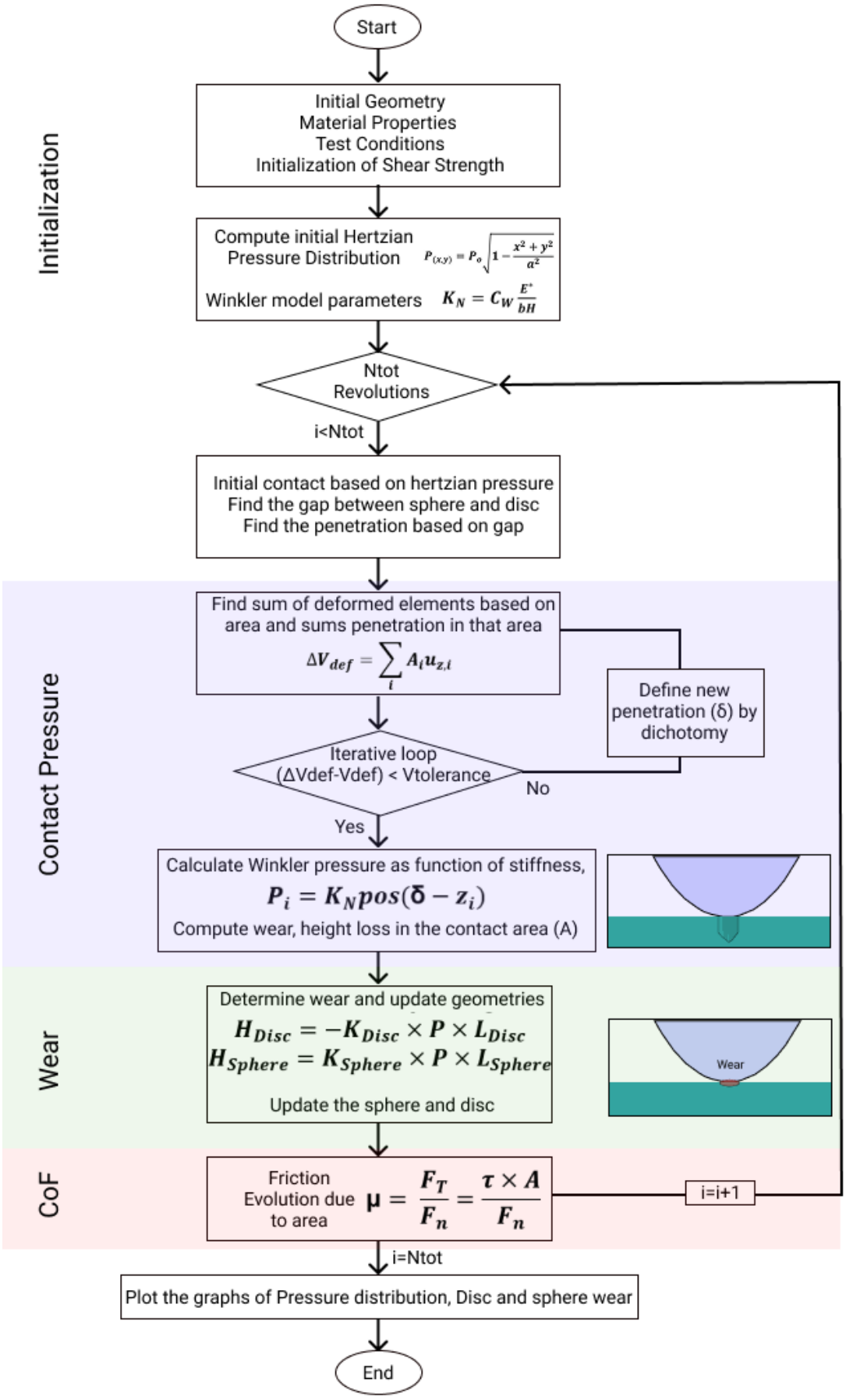

Figure 4.7: Flowchart for Macro Scale Model

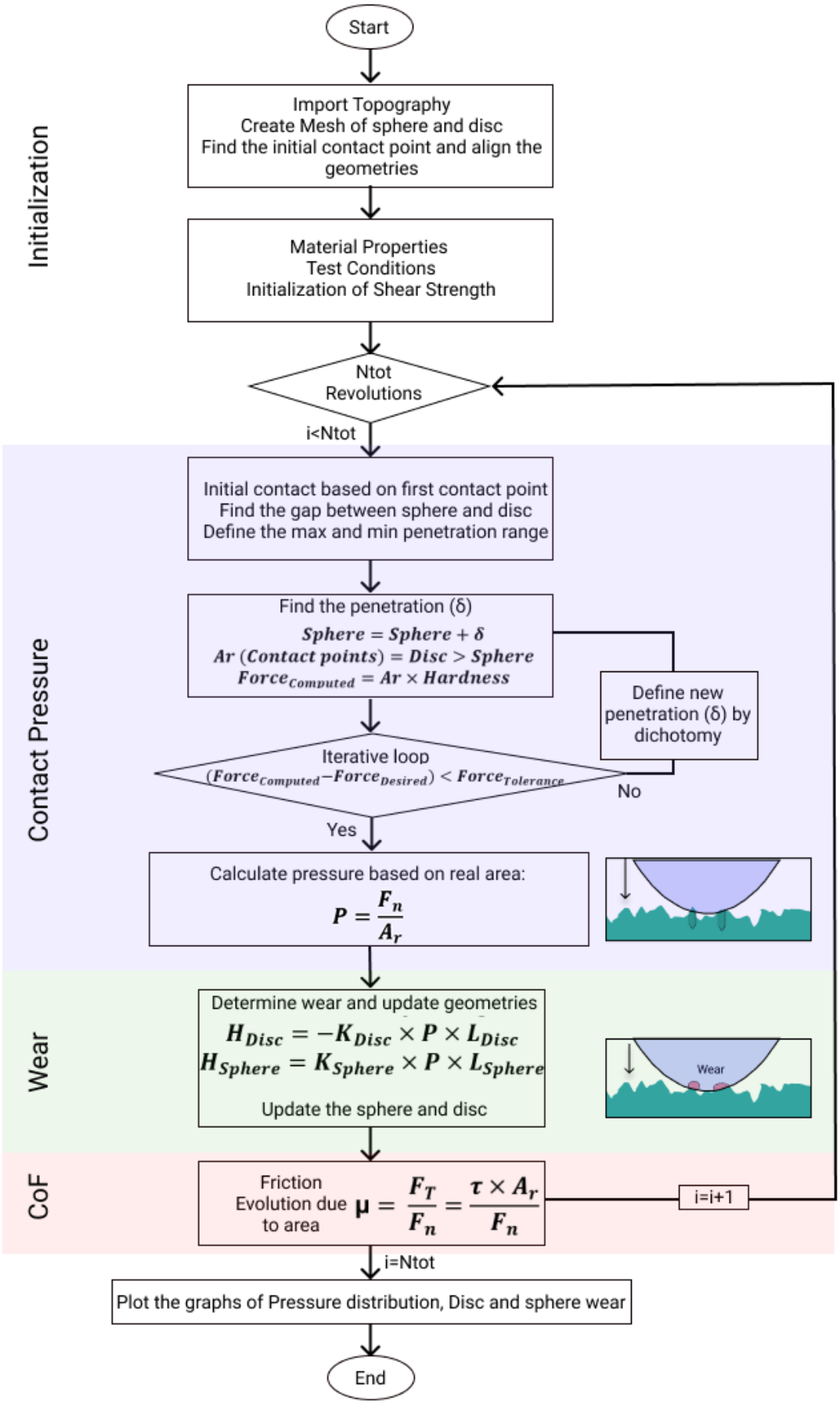

Figure 4.8: Flowchart for Micro Scale Model

Initialization is the first step in the development of the model which is to generate the mesh and geometries, in MATLAB, the process of mesh generation begins with defining the grid within a region centered around the sphere. The grid spacing in the x- and y-directions is specified using the values of dx and dy, respectively. The function `meshgrid` is used to create the 2D matrices X and Y from these ranges of coordinates. These matrices hold the x- and y-coordinates of each of the points in the grid. The grid is discretized to a fine resolution by adjusting dx and dy, which is essential for the precise representation of the disc and sphere geometries in the given region. Following figure 4.9:

- **(a) 3D View**: Shows the sphere on the disc with the direction of motion indicated.
- **(b) 2D View**: Displays a side view focusing on the sphere's position on the disc which is used to take a highlighted portion of whole geometry (area is confined to the diameter of sphere to get more fine mesh as shown in figure 4.9 (c)) for the final mesh.
- **(c) Disc and Sphere Interaction**: Illustrates the final geometry mesh showing contact between the sphere and disc, with one discretized element (`dx`, `dy`).

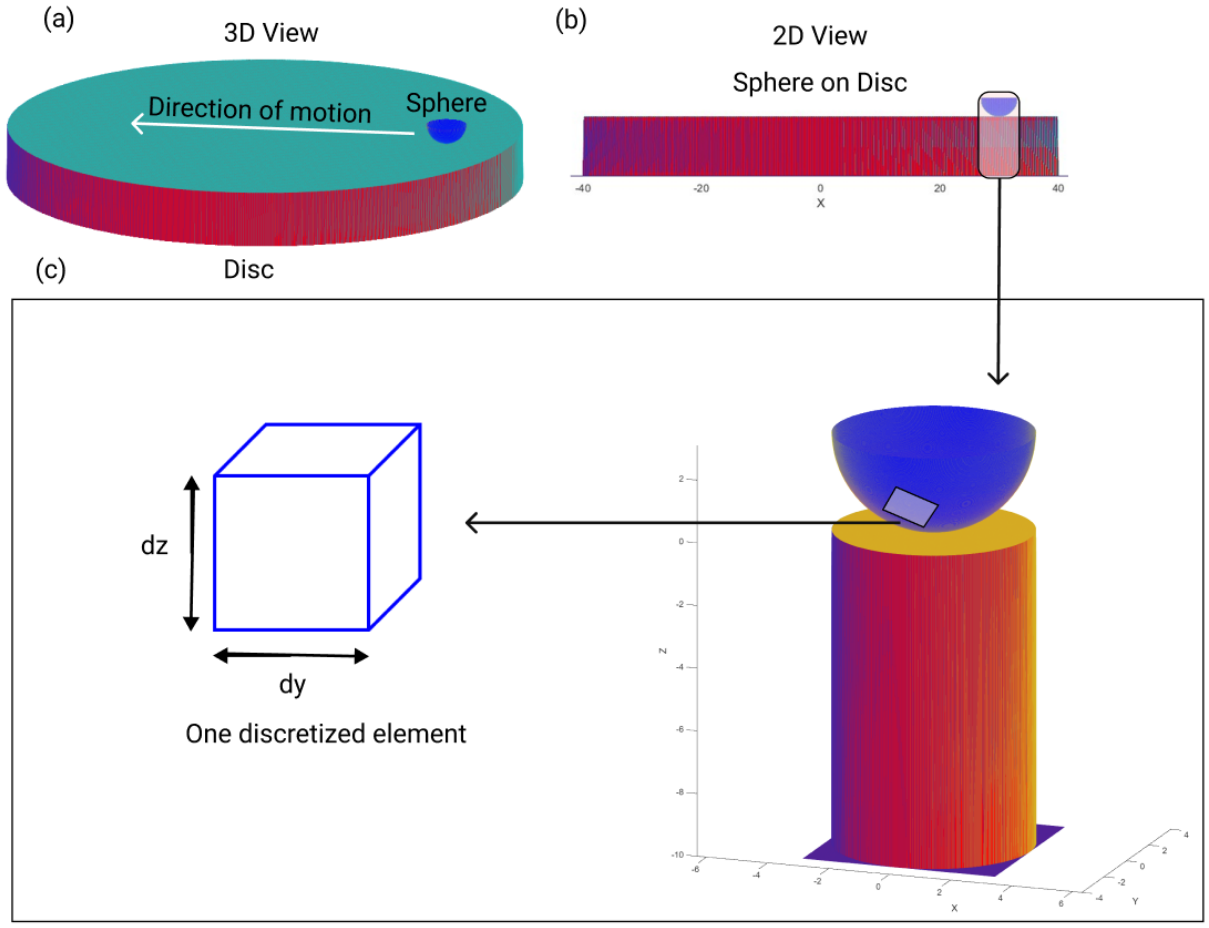

Figure 4.9: (a) 3D View, (b) 2D View, (c) Meshed section of geometry to be used in modelling, with illustration of one discretized element.

Both scale level models use the same wear model and friction equation so that methodological consistency is preserved throughout the framework. Global trends are given by the macro model, and local behavior dictated by surface texture is captured by the micro model. Subsequent sections describe the development methodology of models in detail.

4.2.2 Contact Pressure Modelling

4.2.2.1 Macro Contact Pressure Modelling

In macro scale tribological model, contact pressure distribution of a spherical indenter and a flat disc is simulated based on the Winkler elastic foundation model which has been explained in section 2.4.2.1. The model simplifies the contact mechanics issue through the treatment of the contact interface as a system of independent, vertically acting linear springs with a sphere on top as counter-body as illustrated in figure 4.10, thus ignoring lateral interactions between neighbouring surface elements. Equation 2.6 is used to calculate effective stiffness of every spring which can be used to calculate the total elastic deformation volume under an applied load as:

$$V_{\text{def\_tolerance}} = \frac{F_n}{K_N}[mm^3] \tag{4.1}$$

representing the vertical displacement needed by the elastic foundation in order to equilibrate the external load, it is initially assigned as volume tolerance to be utilized in bisection loop as follows.

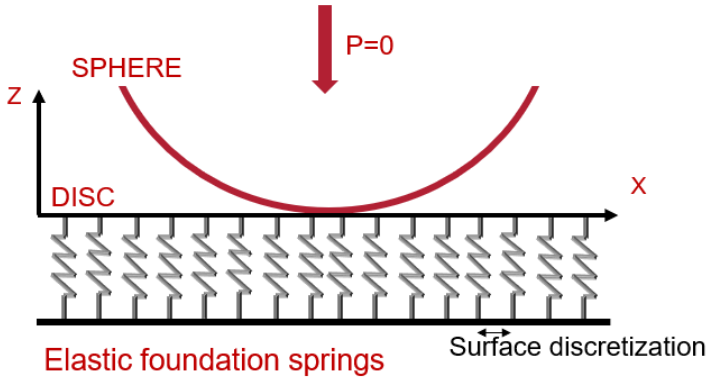

Figure 4.10: Illustration of sphere on disc consisting of vertical springs

In order to determine the actual penetration δ corresponding to the applied load, an iterative **dichotomy** method is used. The dichotomy method (Step 1 to Step 6) is an iterative root-finding algorithm that successively narrows the solution interval by halving the search interval repeatedly between a lower limit (Z_{min}) and an upper limit (Z_{max}). The midpoint is tested in each iteration, and the interval is varied based on whether the current estimate is greater than or less than the desired value. This enables convergence to the proper penetration δ to within the specified tolerance. The local gap (this GAP_Z determine the Z_{max} and Z_{min} penetration range for the dichotomy loop) between the sphere and disc surfaces is given as

$$\text{GAP}_Z = Z_{\text{sphere}} - Z_{\text{disc}} \tag{4.2}$$

The procedure to compute the deformed volume corresponding to specific penetration can be divided into the following steps:

Step 1: Loop Condition

The loop is repeated as long as the absolute difference between the deformed volume for the current penetration ($V_{\text{def\_delta}}$) and the target deformed volume (V_{def}) is larger than the volume deformation tolerance defined ($V_{\text{def\_tolerance}}$):

$$|V_{\text{def\_delta}} - V_{\text{def}}| > V_{\text{def\_tolerance}} \tag{4.3}$$

Step 2: Find the midpoint of Z_{min} and Z_{max}

The value of δ is calculated as the average between Z_{min} and Z_{max}:

$$\delta = \frac{Z_{\text{min}} + Z_{\text{max}}}{2} \tag{4.4}$$

Step 3: Find the Penetration

The penetration is calculated as the difference between δ and the gap (GAP_Z):

$$\text{penetration} = \delta - \text{GAP}_Z \tag{4.5}$$

Step 4: Binary Indicator for Positive Penetration

An indicator function $BIN_{\text{penetration}}$ is used to mark elements with positive penetration:

$$BIN_{\text{penetration}} = \begin{cases} 1 & \text{if penetration} > 0 \\ 0 & \text{otherwise} \end{cases}$$

Step 5: Calculate Deformed Volume for a Given δ

The deformed volume for the given penetration δ is computed as:

$$V_{\text{def\_delta}} = d_x \cdot d_y \cdot \sum_i \sum_j \left(BIN_{\text{penetration}}[i,j] \cdot \text{penetration}[i,j] \right) \tag{4.6}$$

where d_x and d_y are the element dimensions in the x- and y-directions, respectively.

Step 6: Update Z_{min} and Z_{max}

The values of Z_{min} and Z_{max} are updated based on the comparison between $V_{\text{def\_delta}}$ and V_{def}:

- If $V_{\text{def\_delta}} > V_{\text{def}}$, then:
$$Z_{\text{max}} = \delta$$
- Otherwise, if $V_{\text{def\_delta}} \leq V_{\text{def}}$, then:
$$Z_{\text{min}} = \delta$$

At loop end, volume displaced by springs beneath the present penetration estimate will have positive contact nodes in the form of BIN_penetration ensures that only contacting nodes contribute to the

pressure as illustrated in figure 4.11. So, upon convergence, the local pressure field is recovered as

$$P_{\text{Winkler}} = K_N \cdot |\text{penetration}| \cdot BIN_{\text{penetration}}[Pa] \tag{4.7}$$

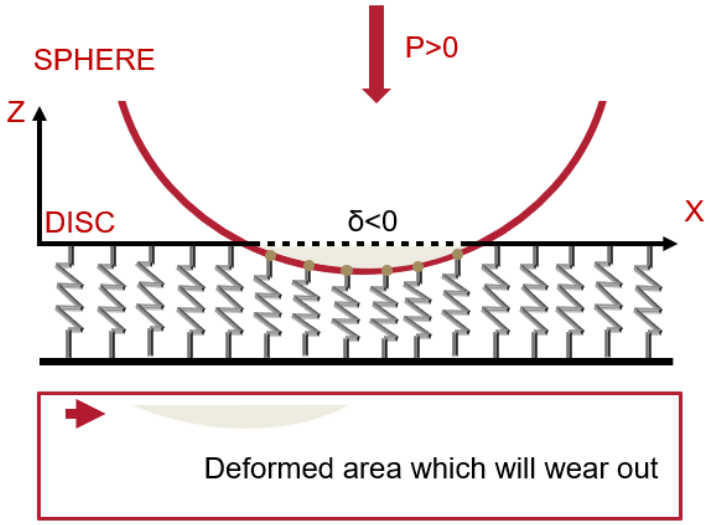

Figure 4.11: Illustration of sphere on disc with deformed volume of vertical springs

This pressure profile is then utilized to calculate wear depth on both the sphere and the disc using Archard's wear law that is explained in the next section 4.2.3. In short, at first, the sphere is in contact over the undeformed elastic foundation (springs) with zero pressure as in figure 4.10. As the sphere penetrates, springs compress where the penetration δ is greater than the local gap, generating pressure at the contact nodes in those locations as in figure 4.11. The deformed area represents the region subjected to wear. As sliding continues as in figure 4.12, this region changes, worn material is taken away, and deformation of new regions occurs in the adjoining areas. This represents the sequential wear behavior in several passes showing cumulative progressive wear. Relative to full finite element simulations, this method achieves a considerable saving in computational expense without sacrificing the capacity to resolve key features of macro-scale contact evolution.

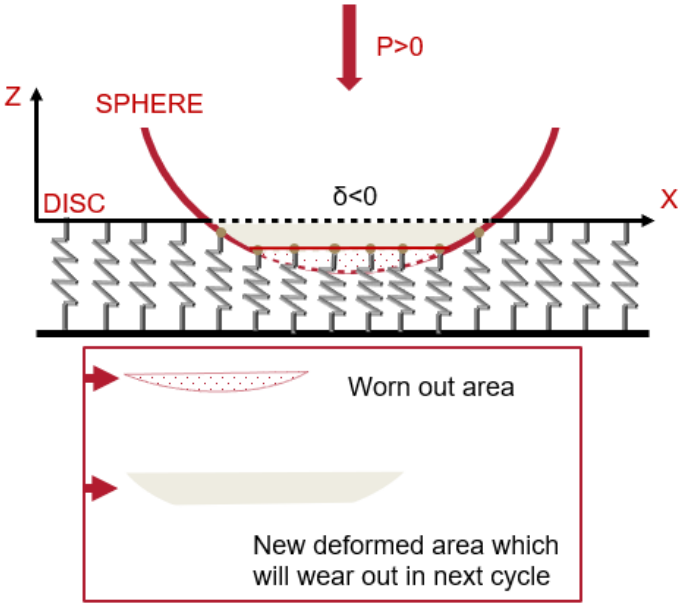

Figure 4.12: Illustration of sphere on disc with accumulation of wear

Compared to full finite element simulations, this approach offers a significant reduction in computational cost while maintaining the ability to capture essential characteristics of macro-scale contact evolution.

4.2.2.2 Micro Contact Pressure Modelling (Rough Contact)

In MATLAB, a contact model of roughness was developed in depth to simulate pressure distribution and wear evolution at the surface between a rough disc and smooth spherical counterbody. The model begins with importing true surface topography from MountainsMap as a 3D point cloud, which is then restructured into a structured surface matrix for the definition of the rough disc geometry. This roughness profile is graphed upon a plane disc of given thickness and radius, space-recentered to coincide with the axis of symmetry of the sphere. A spherical surface of given radius is generated with a spherical equation, allowing controlled, repeatable penetration into the disc surface as sliding distance is applied. The disc is repositioned so that point of initial contact is set as shown in the figure 4.13.

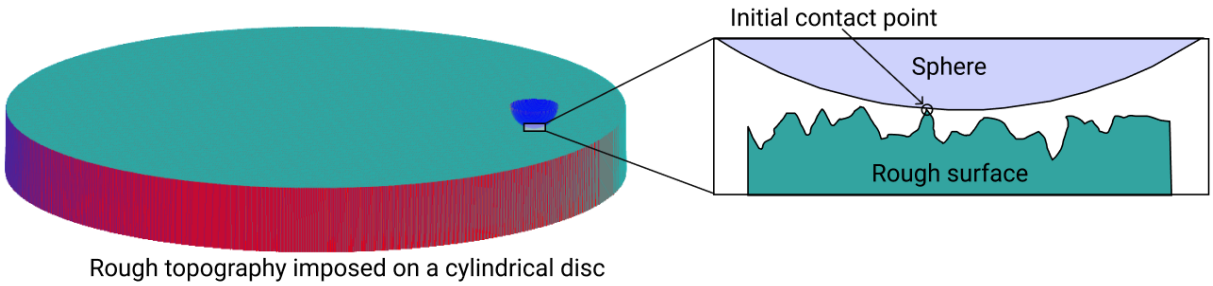

Figure 4.13: Illustration of sphere on rough surface disc with initial contact point

The process of iteration begins by calculating the penetration depth δ, which is considered as an

average of the maximum and minimum values of penetration:

$$\delta = \frac{\text{max\_penetration} + \text{min\_penetration}}{2} \tag{4.8}$$

This penetration depth is used to displace the sphere by adding the calculated penetration depth to the surface height that will shift the sphere downwards providing new sphere position Z_{Sphere_new}.

Then the real contact area A_{real} is computed by determining the number of contact cells that are the locations where the new sphere position Z_{Sphere_new} and disc intersect. Area is found by dividing the number of contact elements by area:

$$A_{\text{real}} = \text{elements\_contact} \times d_y \times d_x [mm^2] \tag{4.9}$$

The new force $F_{\text{penetrate}}$ is then calculated by the product of the real contact area and the material hardness H:

$$F_{\text{penetrate}} = A_{\text{real}} \times H[N] \tag{4.10}$$

The dichotomy loop then iteratively adjusts the penetration depth until the penetration force converges to the applied force F_n. The loop continues until the difference between the applied and calculated penetration forces is within an acceptable margin of 0.5 N:

$$|F_n - F_{\text{penetrate}}| < 0.5$$

Once this condition is fulfilled, the final penetration depth δ is recorded that is a match with penetration under applied normal load as depicted in following figure 4.14, and the loop ends here. The model proceeds with further calculations, including determination of contact pressure P via real contact area:

$$P = \frac{F_n}{A_{\text{real}}} [Pa] \tag{4.11}$$

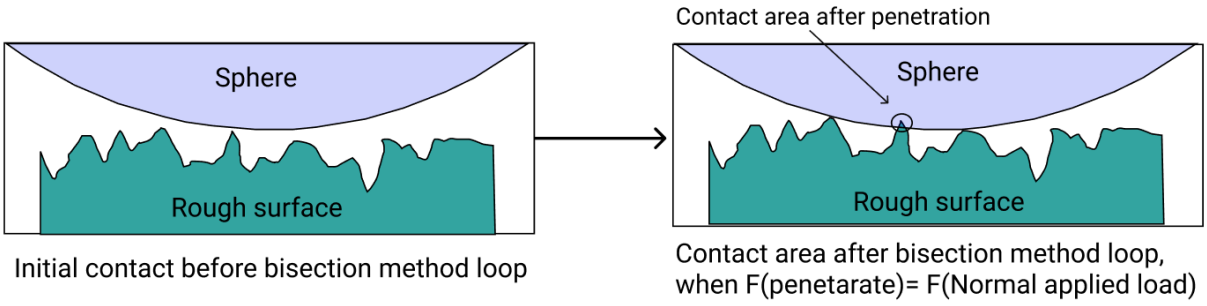

Figure 4.14: Illustration of sphere on rough surface disc with contact point when penetration due to normal load is achieved

This iterative procedure provides a correct computation of the pressure distribution and wear development along the surface between the rough disc and the spherical counterbody. The model tracks wear progress based on Archard's law, smoothing the disc and sphere geometries after

every step of sliding as discussed in section 4.2.3. Through solving contact at the asperity level and iteratively smoothing the emerging surface geometries, this model is able to effectively trace the transient and localized pressure distribution behavior in rough contact conditions.

4.2.3 Wear Modelling

As discussed earlier, both models offer a different degree of detail in capturing the pressure distribution, and both models are utilized to simulate wear under different conditions. After the macro-scale contact pressure P_{winkler} and micro-scale contact pressure $P_{\text{rough contact}}$ is calculated, the wear at every point on the surface is computed using Archard's wear law that connects the wear volume V with the applied load F_n, the hardness of the material H, and the sliding distance L. The simplified form of the equation is:

$$\frac{V}{L} = K \cdot \frac{F_n}{H} \tag{4.12}$$

Hardness H is a key factor in the determination of the wear resistance of the material. In most situations, the wear coefficient K can be thought of as a composite parameter that encompasses the influence of hardness. So, wear coefficient K is adjusted to include the hardness of the material, resulting in a new expression K' that is a function of the hardness H. The adjusted wear coefficient K' is given as:

$$K' = \frac{k}{H}$$

The correlation between the initial wear coefficient and the material's hardness enables the wear model to be more precise, particularly if different materials or surface treatments are being compared. By including hardness in the wear coefficient and once again expressing it as K for convenience, the wear equation is:

$$V = K \cdot F_n \cdot L[mm^3] \tag{4.13}$$

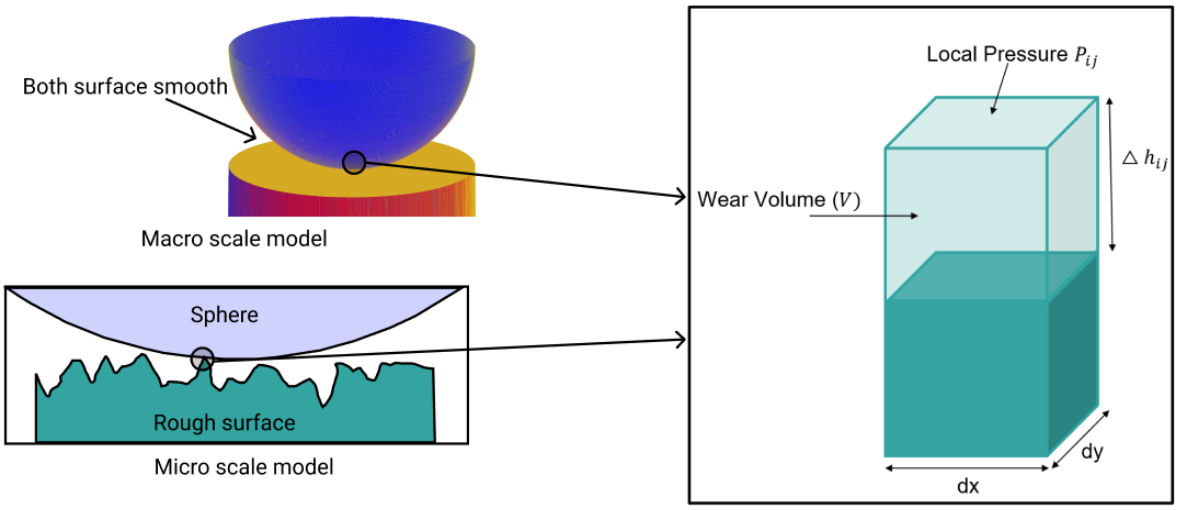

Figure 4.15: Illustration of macro and micro scale models with similar discretization, where Archard's wear law is applied to analyze wear volume at element level

In order to describe wear in more localized regions, the wear equation can be further developed by discretizing the surface. For small areas of contact, the wear rate can be modelled for every discrete element with dx and dy dimensions, and it is same for both scale of models as shown in the following figure 4.15. Here, we define the depth of wear at the i, j-th point, δh_{ij}, and pressure and velocity for the localized contact area. The wear rate at a localized point is given by:

$$\frac{\Delta h_{ij}}{\Delta t} = K \cdot P_{ij} \cdot V_{ij}[mm/s] \tag{4.14}$$

where:

- $\Delta h_{ij}$is the wear depth change at the localized region,
- P_{ij} is the local pressure at the contact region,
- $V_{ij}$is the local sliding velocity at the contact region,
- Δt is the time step.

This formula is based on the fact that wear is local in relation to the pressure and velocity at each surface point, which are constantly updated during the evolution of the contact.

The sliding velocity V_{ij} is the distance travelled at the contact region per unit time. The sliding distance L_{ij} over a small time interval Δt is connected with the velocity by:

$$L_{ij} = V_{ij} \cdot \Delta t[mm]$$

Substitution of this expression for the sliding distance into the wear rate equation yields:

$$\frac{\Delta h_{ij}}{\Delta t} = K \cdot P_{ij} \cdot \left(\frac{L_{ij}}{\Delta t}\right)[mm/s] \tag{4.15}$$

Simplifying the equation, gives the final equation for the change in wear depth Δh_{ij} at a localized contact point is:

$$\Delta h_{ij} = K \cdot P_{ij} \cdot L_{ij}[mm] \tag{4.16}$$

This formula points out that the depth of wear at a localized contact spot is directly proportional to both the local pressure P_{ij} and the sliding distance L_{ij}.

In summary, through the application of Archard's wear law, wear can be predicted both at the macro (based on the contact pressure across the whole surface) and micro to gain an integrated insight into the wear process for different conditions. Using of winkler model at the macro scale enables computationally efficient calculation of the wear over large contact areas, and implication of the rough contact model at the micro scale gives a more realistic description of the wear at local areas of the contact interface. The comparison between the two models ensures that wear predictions are consistent and reliable across contact scales and enhances the insight into the wear process, enabling the optimization of modelling framework.

4.2.4 Evolution of CoF Modelling

In this work, the coefficient of friction (CoF) is not considered as a static input but as an adaptable parameter which varies with the sliding surface condition. The main assumption in this work is that friction arises due to the interaction between real contact area and interfacial shear strength, both of which contribute to the resistance to sliding. This is inspired by experimental data showing that surface modification and asperity deformation significantly influence frictional behaviour. The instantaneous friction force F_t is represented in a simple shear law:

$$F_t = \tau \, A_r [N] \tag{4.17}$$

where τ is the effective interfacial shear strength and A_r the real contact area. The coefficient of friction then follows as:

$$\mu = \frac{F_t}{F_n} = \frac{\tau \, A_r}{F_n} \qquad [Dimensionless] \tag{4.18}$$

with F_n the applied normal load. This simple equation state that the real area of contact variability directly corresponds to the CoF variability, provided τ is constant.

Initialization of shear strength

The model is adapted to the experimental end-of-test wear test data. The effective shear strength τ_0 is computed from the end-of-test measured CoF μ_0 and associated contact area A_0:

$$\tau_0 = \frac{\mu_0 \cdot F_n}{A_0} [Pa] \tag{4.19}$$

This τ_0 is a simulation-wide constant parameter to be tuned to simulate different materials or contact conditions.

Dynamic update during wear

As wear increases, the true area of contact changes because asperities are flattened and new areas make contact. At each simulation step the new contact area A_{new} is computed, and the CoF is re-computed as:

$$\mu_{\text{new}} = \frac{\tau_0 \cdot A_{\text{new}}}{F_n} \tag{4.20}$$

Thus, CoF evolves dynamically with geometry change, but shear strength remains constant. Figure 4.16 illustrates this idea, On the left-hand side, the disc–sphere contact begins with an initial small real area of contact Ar_1 and corresponding shear strength τ_1, which creates a relatively low tangential force F_t. On the right-hand side, after wear has built up, the area of contact increases to Ar_2. A greater real area allows greater shear force ($\tau_2 Ar_2$) to be created, which increases F_t and thus the CoF. The scheme shows friction is regulated along with interfacial shear strength and real contact area: both are required to define CoF evolution.

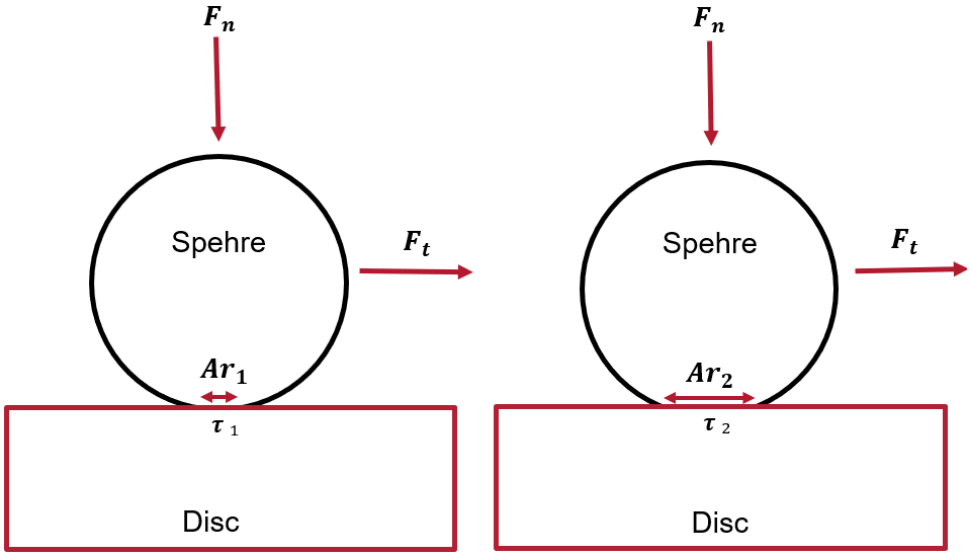

Figure 4.16: Schematic representation of CoF evolution

This modelling framework provides an explicit method of coupling friction and wear, the CoF varies as contact area does under constant wear conditions. While this does not model potential fluctuations of τ due to transfer films or chemistry, it does indicate the dominant process through which surface evolution due to wear alters frictional resistance.

4.3 Models Results & Analysis

4.3.1 Version 1st Results

First version of developed model is based on winkler elastic foundation model to calculate the pressure which is used in archard wear law to calculate the worn height and based on the area where that pressure is applied, simple CoF equation has been used, so in each iteration different types of values and outputs are stored. First, as discussed in section 3.3, initially Hertzian pressure was applied to initiate the contact, as soon as initial penetration is determined which is used to find the deformed volume, winkler pressure is calculated. Initially at start, winkler pressure is approximately equal to Hertzian pressure. When sphere travel a distance of 240mm which is equal to 80 Ntot in the model (1 Ntot = 100 iterations of update), due to wear contact area increases pressure reduces and get flatten at the contact surface. Following figure 4.17 shows the pressure distribution results at initial point by Hertzian pressure and at increased contact area after 2400mm sliding distance by winkler pressure (calculated on basis of the penetration).

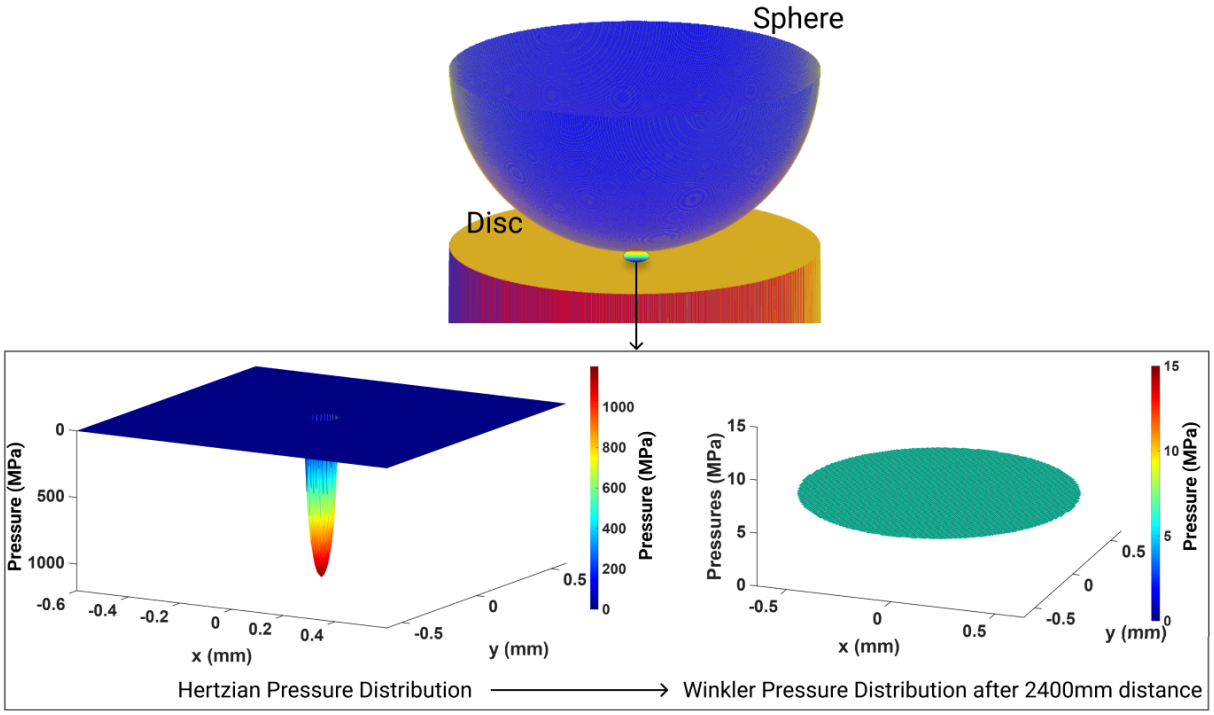

Figure 4.17: Change of pressure distribution from Hertzian to Winkler pressure distribution after 2400mm sliding distance on contact area

Over the whole 2400mm sliding distance, contact radius keep increasing due to wear which decreases the contact pressure at next iteration, change in both quantities is very high at the start then the rate of change is relatively very low (Approximately, after 0.1m sliding distance, rate of change of contact area and mean pressure is slowed down) as shown in the figure:

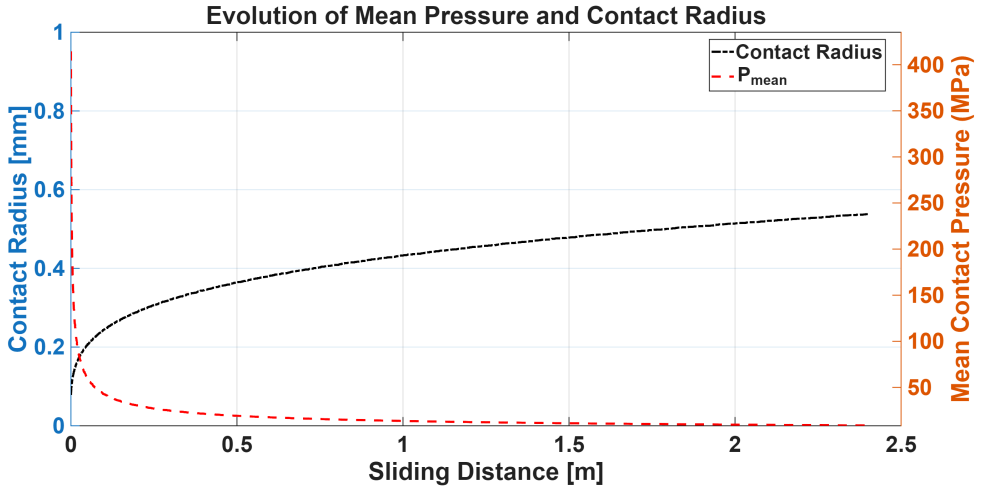

Figure 4.18: Evolution of contact pressure and contact radius over 2400mm sliding distance

When in each iteration, winkler pressure is applied to the arcahrd wear law (wear coefficient for disc and sphere are applied), worn height is calculated and stored, following figure 4.19 (x-axis sphere radius and y-axis Disc wear (mm)) is the results for disc wear evolution at different Ntot corresponding to different intervals of sliding distance (1 Ntot=30mm, 20 Ntot=600mm, 40

Ntot=1200mm, 80 Ntot= 2400mm). As it can be seen that as sliding distance passes, wear height increases on disc but also contact area of worn height also increases. Figure A.7 in appendix 5 is evident that disc wear depth evolution is non-linear (same results from sphere wear evolution).

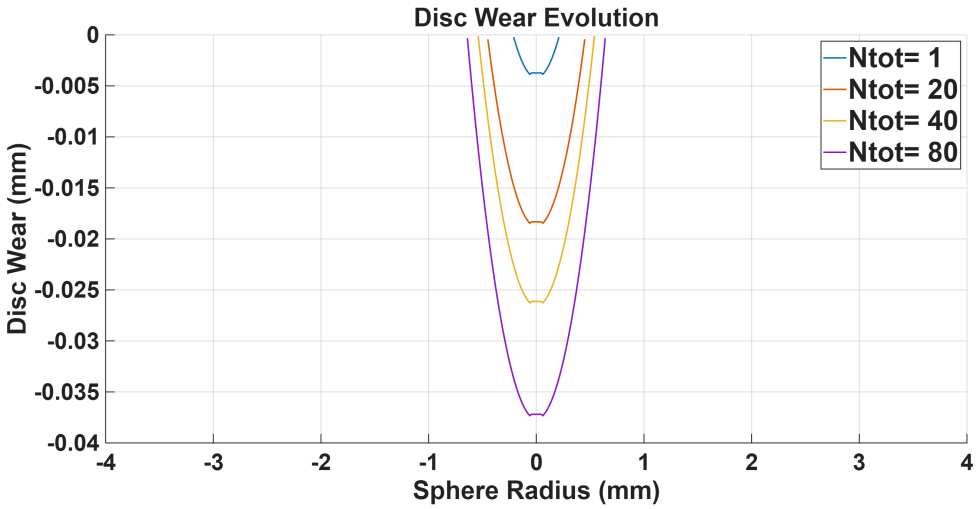

Figure 4.19: Disc wear evolution

Figure (a) and (b) shows that final worn track on the disc and worn patch on sphere geometry respectively.

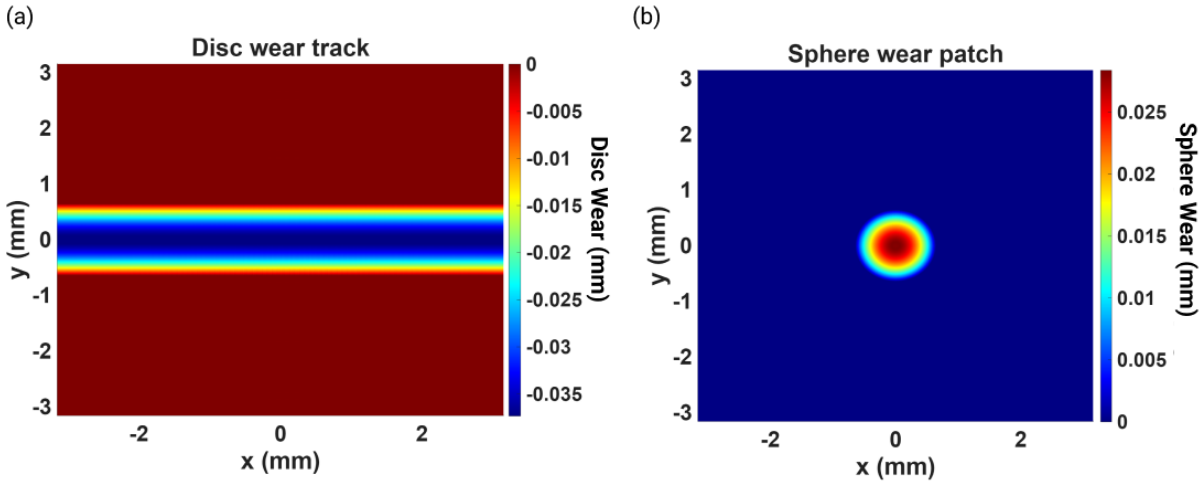

Figure 4.20: Final wear (a) track on the disc and (b) patch on the sphere

Model also accumulate the wear volume for both disc and sphere, total wear volume follows the archard wear law and shows linear behaviour over sliding time as shown in following figure 4.21:

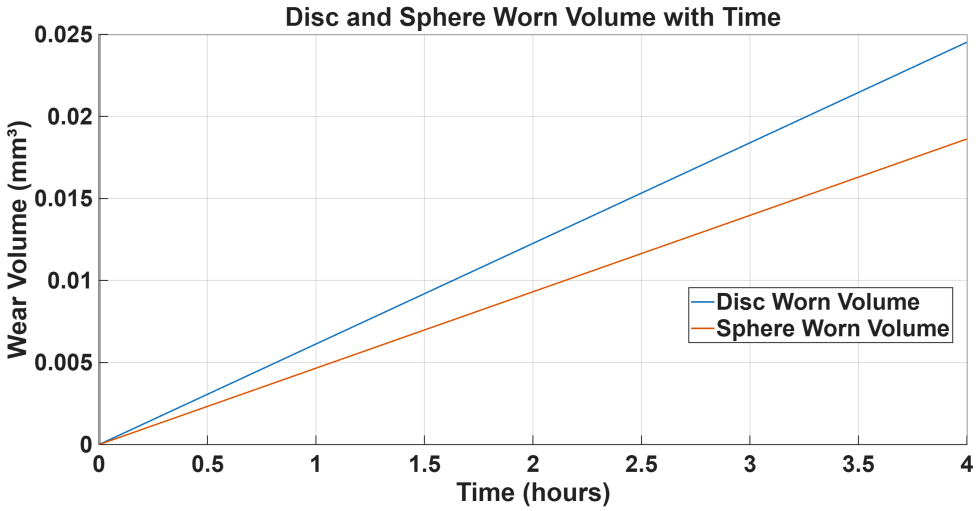

Figure 4.21: Total wear volume of disc and sphere over sliding time

For the CoF modelling, most important output is the evolution of CoF over sliding time as shown in figure 4.22, it is important to note that most critical parameter for the calculation of CoF in each iteration is the tunable shear strength. In experiments or real application, shear strength is also changing during the wear process but it cannot be modelled that easily, so its kept as constant to give rough idea of CoF evolution depending upon the contact area. Depending upon the test condition if initial shear strength is optimised or tuned, CoF evolution can be optimised too.

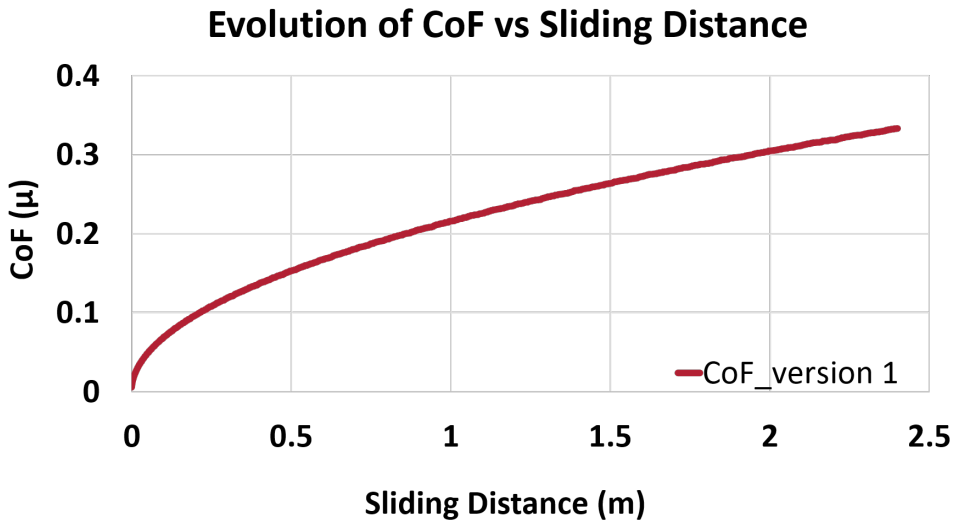

Figure 4.22: CoF evolution at contact between sphere and disc over total sliding distance

In 1st version the main questions which arises are what about the roughness of the disc, how vital it is for evolution of wear over sliding distance and CoF evolution over time but other than this another important limitation of version 1st is sliding distance, right now it has been assumed that sliding distance for each point on disc is 2400mm but in reality its not true, with the curvature of sphere, sliding distance on disc will change. Mesh points of disc which will be in interaction with

sphere centre will be covering more sliding distance than mesh points of disc which re interacting with sides of curvature of sphere during the sliding motion. To solve this limitation a factor is needed which will compensate this effect and make sliding distance function of sphere curvature, version 2 has been developed with this factor which is explained in the following section.

4.3.2 Version 2nd Results

Sliding distance which is one of the most important input for the Archard wear law is not constant across all points on the disc. Points that are farther away from the center of the sphere will travel a shorter distance compared to points closer to the center. This variation in sliding distance can be explained using trigonometric ratios, as shown in the following figure 4.23.

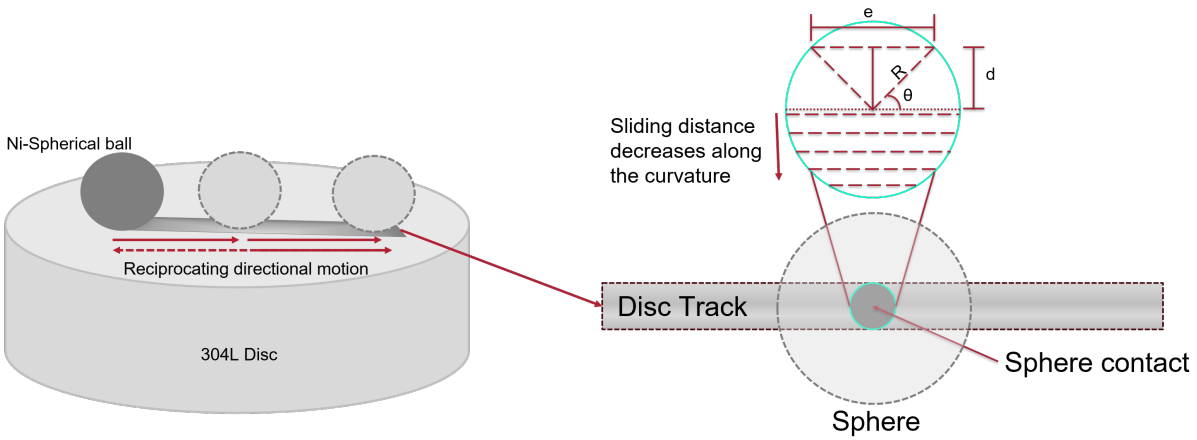

Figure 4.23: Geometric representation of the sphere-disc interaction, showing the variation in sliding distance (e) across the disc surface based on the radial distance and contact angle

To calculate this, first determine the radial distance of all points from the center of the sphere on both sides. Once the radial distance is known, corresponding contact angle θ is calculated using the equation:

$$\sin\theta = \frac{d}{R} \tag{4.21}$$

where d is the radial distance from the center of the disc to the point of contact, and R is the radius of the sphere. The sliding distance ϵ at any given point is then calculated as:

$$e = 2R\cos\theta[mm] \tag{4.22}$$

This relationship shows that as the point of contact moves farther from the center, the contact angle θ increases, and the sliding distance "e" decreases. Thus, the wear distribution across the disc is not uniform, and points closer to the center experience greater sliding distances compared to those farther away. This geometric approach effectively models the wear progression and provides insight into how the sphere's motion affects the wear distribution on the disc. Figure 4.24 shows the difference between the effect of "e" on the sliding distance travel by disc contact points. Based on this new sliding distance following are some results, first of all due to variation of sliding distance,

wear will not be constant along all points in y direction for the disc, due to this there will be variation in pressure distribution profile as compare to first version of model. Following figure 4.25 shows the comparison between initial Hertzian pressure distribution and winkler pressure distribution after 2400mm sliding distance at the contact area of interaction.

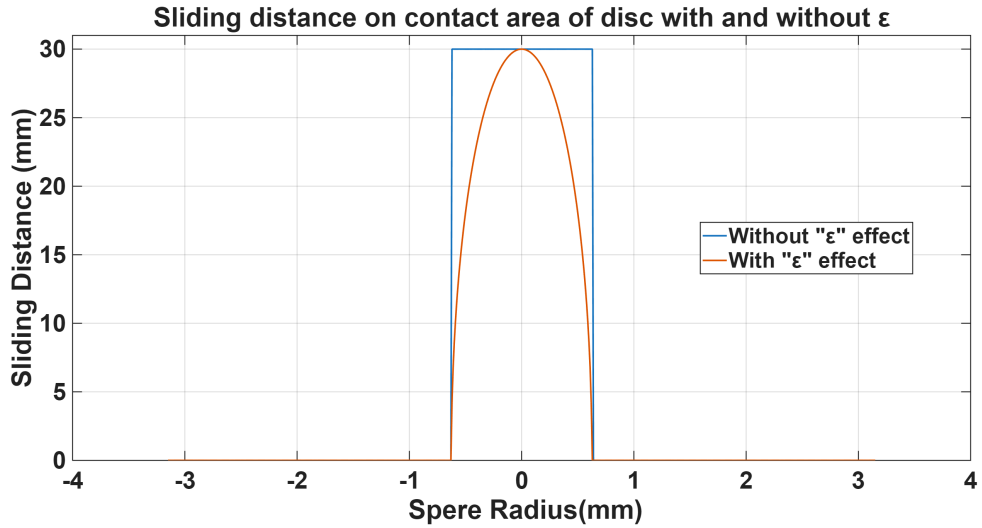

Figure 4.24: Difference between sliding distance for the disc contact points with and without effect of ”e”

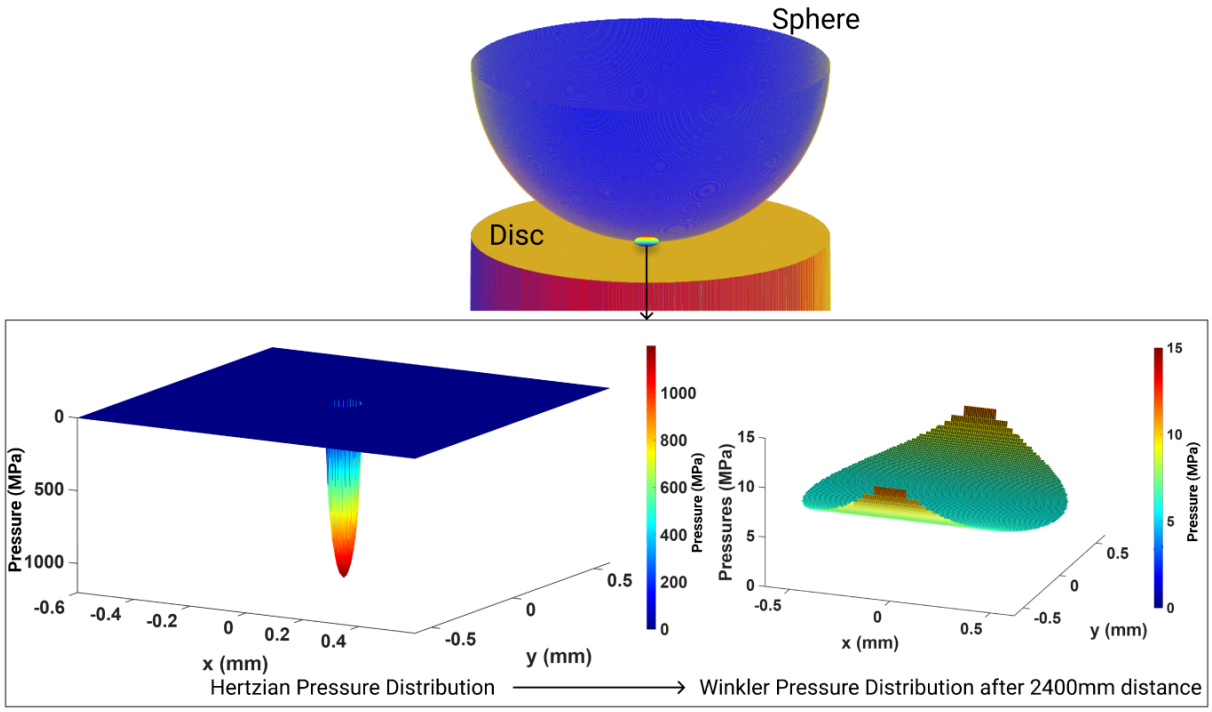

Figure 4.25: Change of pressure distribution from Hertzian to Winkler pressure distribution after 2400mm sliding distance on contact area

Following figure 4.26 shows the results for the accumulated total volume for disc and sphere, as compare to version 1st, since all contact points on disc are not covering same sliding distance, total

wear volume on disc will be less than version 1st, it will be compared in section 4.4. Since, there is no effect of epsilon on the sliding distance of the sphere, total volume of sphere is same (only minor effect observed on wear patch on the sphere surface as shown in figure A.9 in appendix 5), this pattern is probably due to the sequence of points which comes in interaction with disc mesh points.

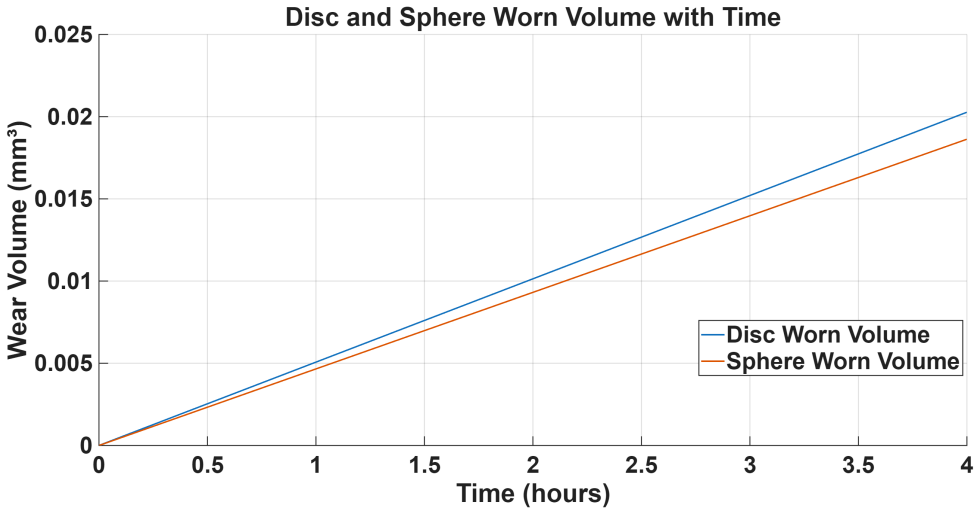

Figure 4.26: Accumulated total volume on sphere and disc with the effect of "e".

Although the overall total wear volume and worn height is approximate same, there is a major impact of "e" can be seen in the evolution of CoF curve, it is due to variation in worn height sequence which slightly impacts the contact area evolution. Following figure 4.27 shows the evolution of CoF due to contact area which is influenced by wear, trend of CoF is same as 1st version, it increases rapidly as contact area increases rapidly then it stabilizes and increase linearly at very low rate.

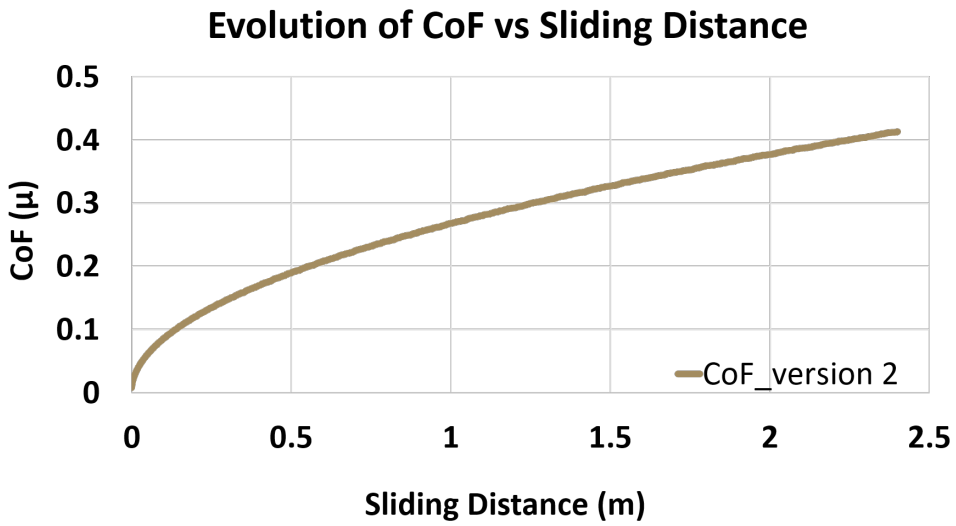

Figure 4.27: Evolution of CoF due to wear with the effect of "e"

Version 2 presents more realistic situation than the version 1, hence these results can be considered more close to practical application.

4.3.3 Version 3rd Results

Version 3 is the micro scale model based on rough contact model with Archard's wear law as presented in section 4.2.2.2, this developed model first find the penetration which is due to normal force of 8N to mimic the experimental force, based on this penetration, pressure is calculated which is applied on real contact area and then Archard wear law is applied on that real contact area with that calcualted pressure. Following are some important results from version 3.

For the pressure, since the mesh element is in size of 10 micron dx and dy, as shown in figure 4.15 on which dichotomy approach find the contact points on surface which will bear 8N load and in all iteration number of contacts points will be same that means pressure applied by sphere on those contact points will be same and it is the main limitation of the rough contact model on MATLAB due to mesh size limitation. So, pressure is always between 580 to 600 MPa which is function of number of contacts points as shown in figure 4.30(c).

Following figure 4.29 shows the (a) tribological model geometry setup with topography and (b) extracted area of disc which will undergo continuos sliding distance (for mesh limitation has to restrict the area) and (c) Extracted worn disc patch at different stages of sliding distance. After analysing the video generated of disc wear evolution from version 3 model, it is clear that wear process is random depending upon the height of peaks or valleys which comes into contact.

This version provide more realistic evolution of wear but there are some limitations as explained earlier due to mesh size limitation on MATLAB platform, increase of contact area is completely linear due to this evolution of CoF due to wear is also linear as shown in figure A.10 in appendix 5. There is no impact on the accumulated wear volume of sphere since all the model uses value of wear coefficient but in this model after applying the impact of epsilon on the sliding distance, wear volume on disc is higher than the version 2 which is developed at macro scale. Following figure 4.28 (a) shows the final worn track on disc rough surface and (b) final worn patch on the sphere surface after 2400mm sliding distance, it is evident that sphere has worn pattern due to high peaks interaction with sphere smooth surface which will be worn out more.

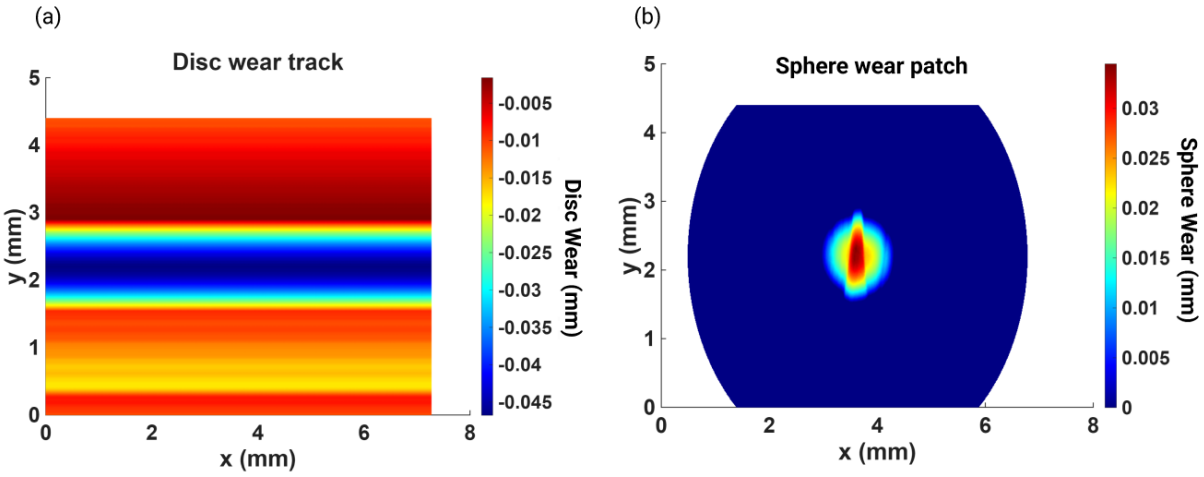

Figure 4.28: Final wear (a) track on the rough disc and (b) patch on the sphere

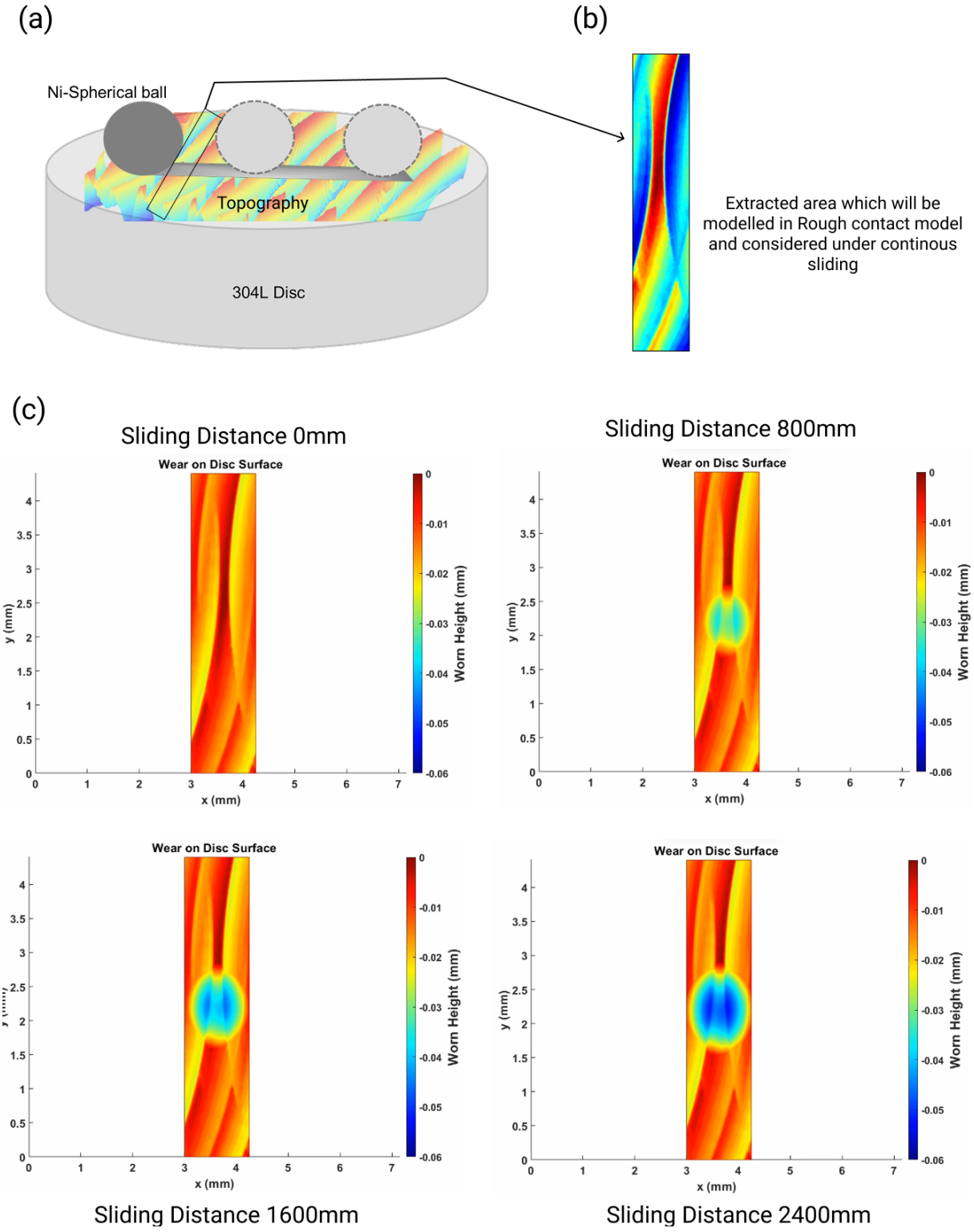

Figure 4.29: (a) Tribological model geometry setup with topography and (b) extracted area of disc which will undergo continuous sliding distance, and (c) extracted worn disc patch at different stages of sliding distance.

4.4 Comparison between Model Versions

In this section, comparison of the results of 3 versions of the developed models has been presented and discussed, which defines the strong and weak points of each model. First most important results are the pressure map on the interaction at the end of the total sliding distance 2400mm, following figure4.30 (a) the pressure map for 1st version which is constant pressure at all points in contact between two bodies, (b) the pressure map for version 2 which is not constant, a curve along the y direction due to varying wear rate at different position due to epsilon effect on the sliding distance and (c) the pressure map for the version 3, which is basically the pressure points on the surfaces mesh which will be worn out at the last iteration which come out due to real area at 8N force and it is the main limitation of coarse mesh in MATLAB.

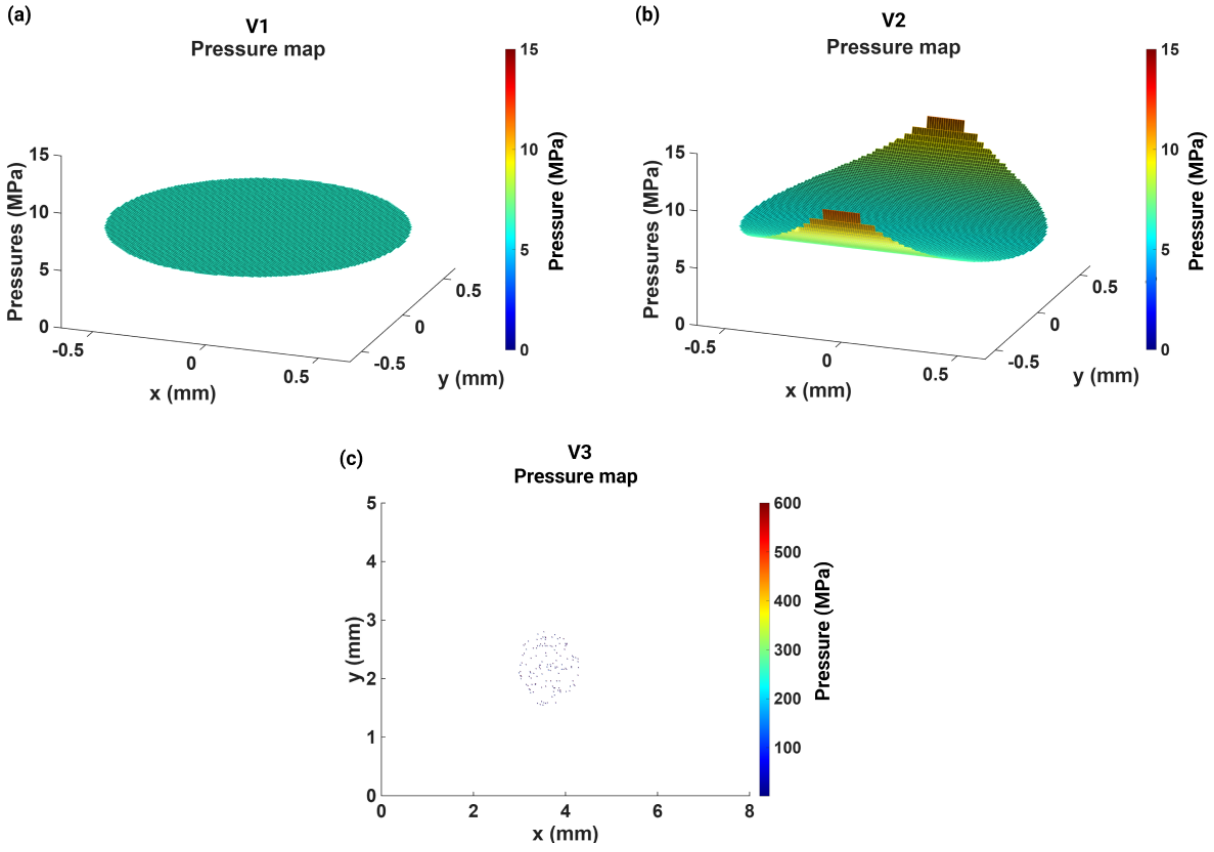

Figure 4.30: Pressure distribution between sphere and disc (a) the pressure map for version 1st which is constant same pressure at all points in contact between two bodies, (b) is the pressure map for version 2 which is not constant due to epsilon effect and (c) is the pressure map for the version 3, which are the pressure points on the surfaces mesh which will be worn out at the last iteration

Another important comparison is the worn height if seems from the y direction to analyse how does worn height of wear track on disc looks like after 2400mm sliding distance for all 3 versions, following figure 4.31 shows (a) worn height of disc track for the version 1st, (b) worn height of disc track for version 2, which is almost same as version 1st, and (c) worn height of version 3 which had real topography of disc sample, its evident that worn height and contact area is larger than both previous versions of the models and reason is high constant pressure which is approximately 600

MPa on the surface in all iterations.

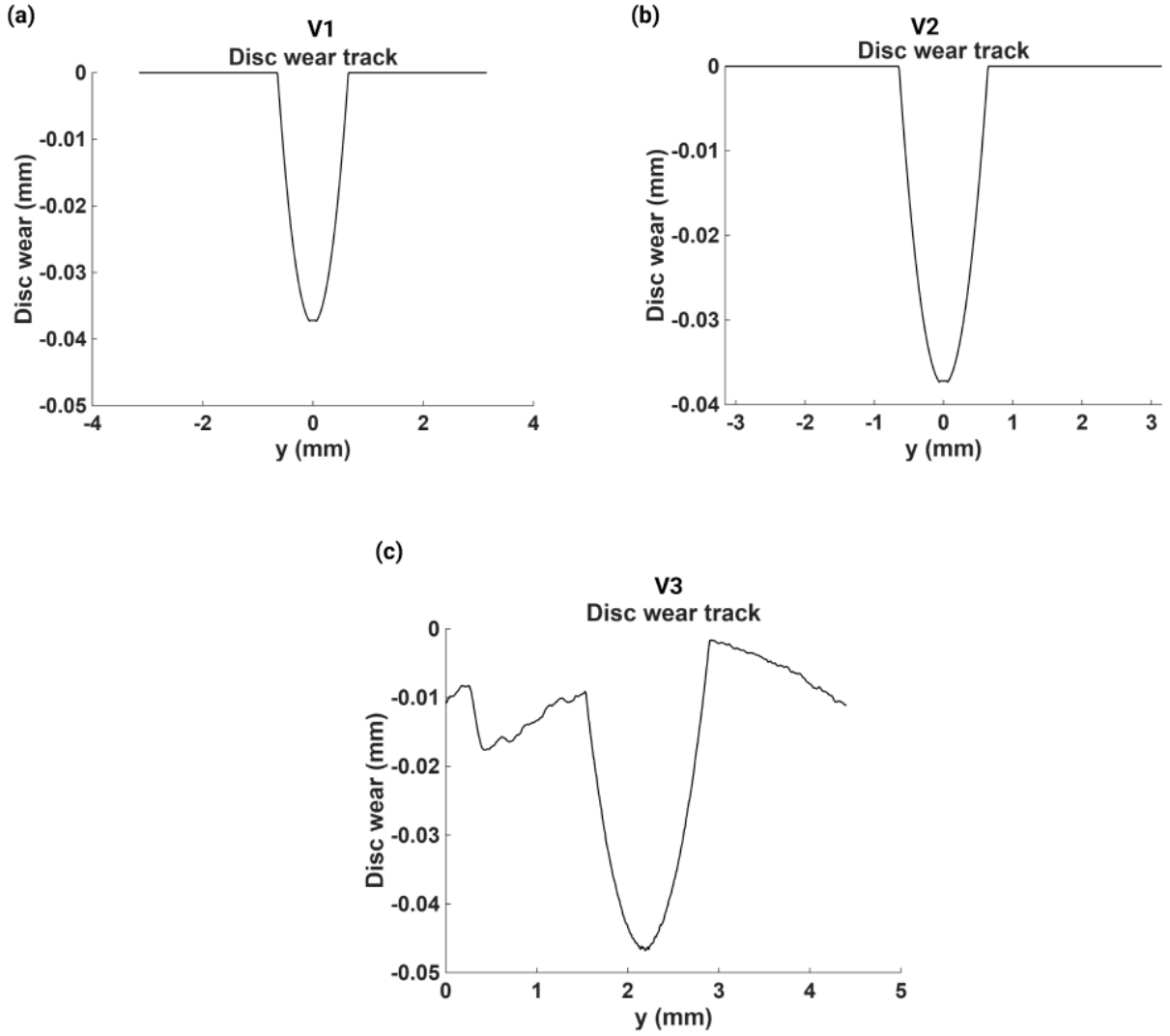

Figure 4.31: (a) worn height of disc track for the version 1st, (b) worn height of disc track for version 2, and (c) worn height of version 3

Sphere worn geometry is compared for three developed models, important observation to be made here is the worn geometry shape and contact diameter after 2400mm sliding distance, following figure 4.32 shows (a) the sphere worn patch for version 1 with worn diameter 1.28mm, (b) the sphere worn patch for version 2 with worn diameter which is also 1.28mm but important thing to notice here is the structure of worn geometry due to epsilon effect on sliding distance instead of being spherical, worn geometry is skewed for version 2, and (c) sphere worn patch for version 3 after sliding 2400mm on rough disc, worn patch will have high worn zones where there were peaks in contact and overall contact diameter is also higher 1.37mm, even though sphere wear coefficient is same for all models, this variation in geometry of worn patch is important to show the way this wear is accomplished and how close it is to real application. Comparison of this worn geometry on sphere with experiment will be discussed in next section 4.5.

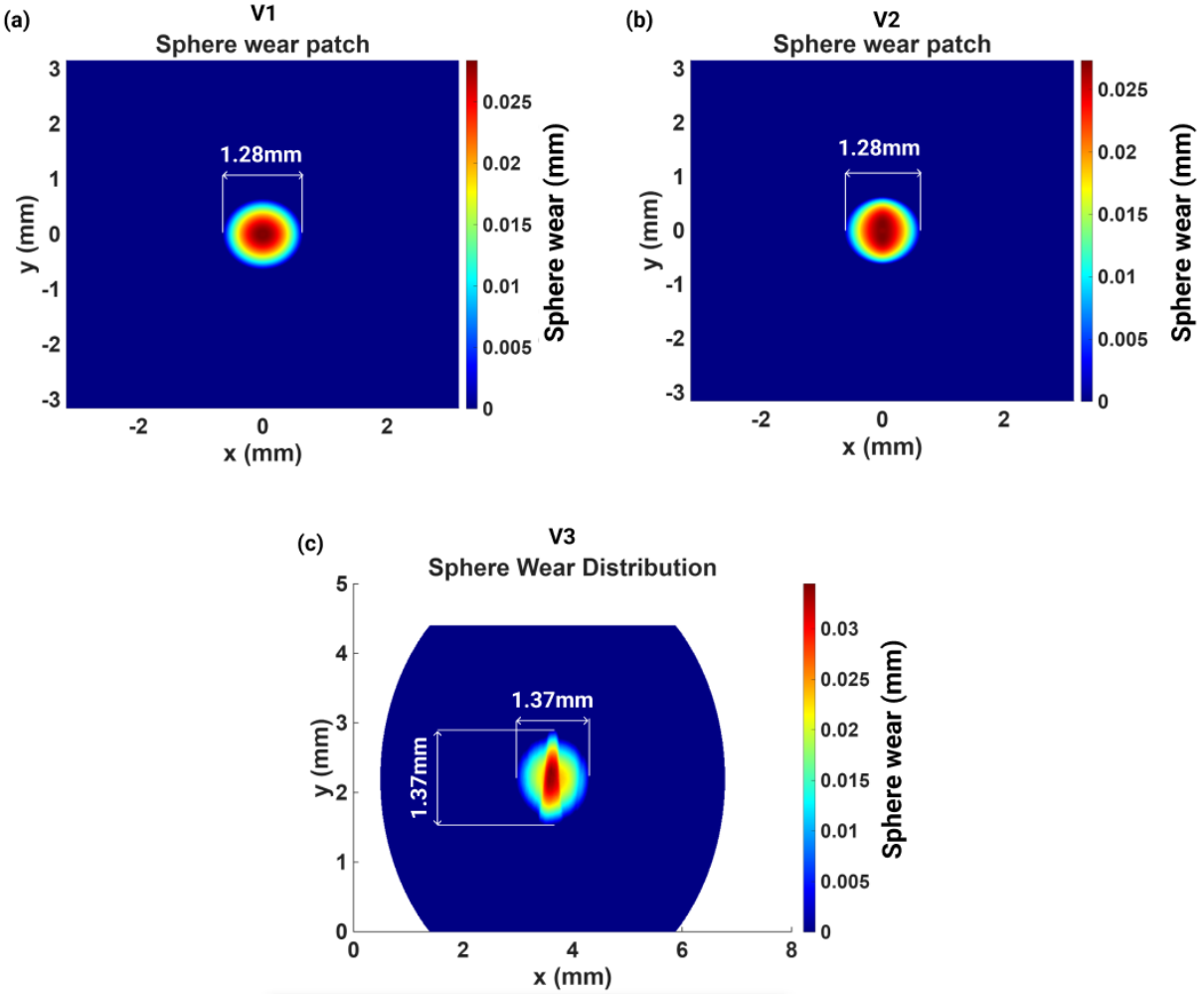

Figure 4.32: (a) sphere worn patch for version 1 with worn diameter 1.28mm, (b) sphere worn patch for version 2 with worn diameter 1.28mm, and (c) sphere worn patch for version 3 with worn diameter 1.37mm.

Graph in the following figure 4.33 shows the comparison of total wear volume of disc for all three versions of developed models, there are small changes which have been noticed in the total wear volume. Version 2 has impact of epsilon on sliding distance on mesh contact points so some points will travel less distance than those in version 1st so total wear volume on disc is slightly lower, but in 3rd version which is micro scale rough contact model with epsilon impact, total wear volume increased and the reason for this increase is same as explained in previous paragraph that pressure is higher and constant in all iterations which gives high wear volume from the Archard wear law.

One of the most important comparison is between the evolution of CoF curves of three developed models, as shown in figure 4.34, version 3 gives very high CoF and it shows linear increase and very high unrealistic values, in case of version 1 and 2, CoF evolution depending upon the contact area between two smooth surfaces as explained in above sections 4.3.1 4.3.2 which are more realistic.

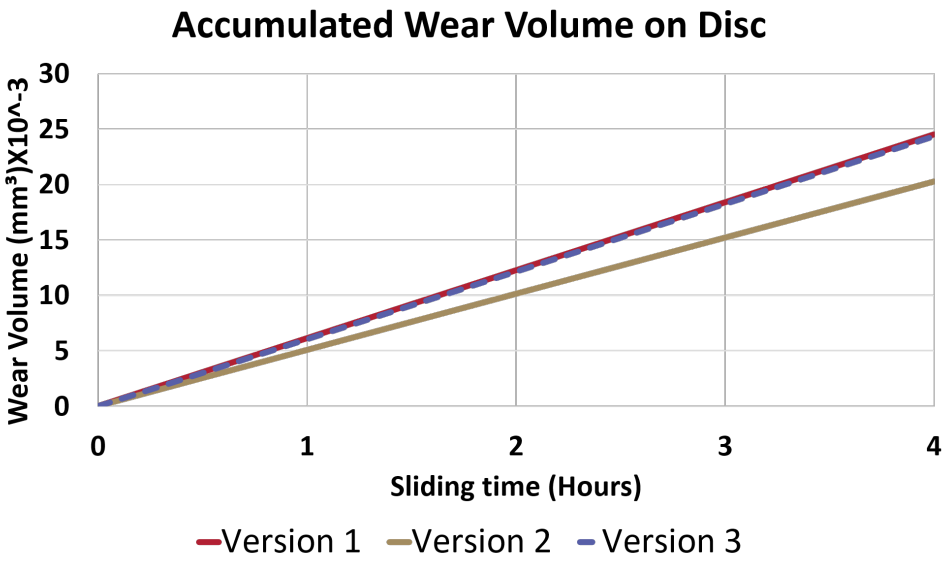

Figure 4.33: Accumulated total wear volume on disc for all three versions of models

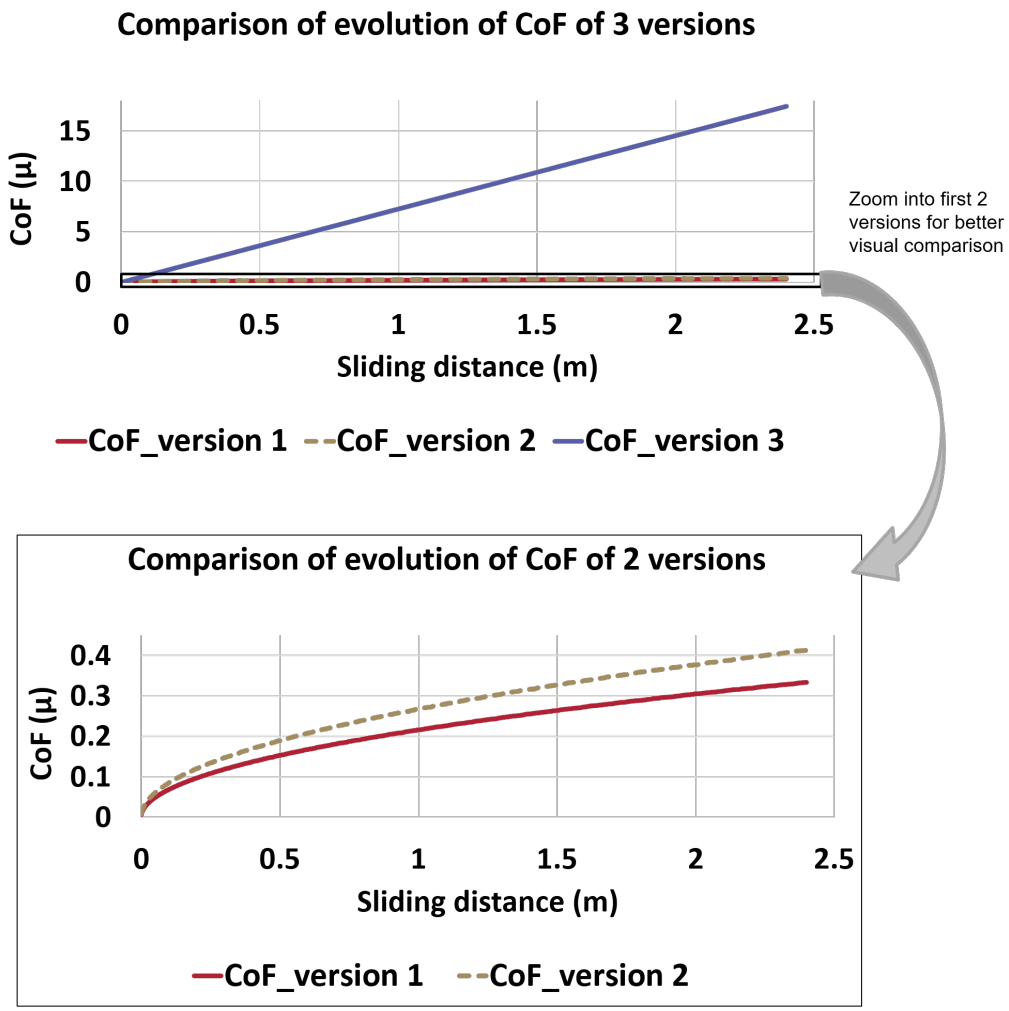

Figure 4.34: Comparison of evolution of CoF curves of three versions of models

4.5 Comparison with Experimental Results

It is also important to compare the results with the experimental tests output, since there is no actual data recorded for pressure evolution form experimental test, its not have been compared, followings are some main comparisons between experimental tests and 3 versions of models: comparison of worn height of disc, comparison of sphere worn patch diameter, comparison of total wear volume on disc and most important is comparison of evolution of CoF curves. Following figure 4.35 shows the comparison of disc worn height, data for 12 experiments were averaged out after analysing on the MountainsMap software as explained in section 3.2.3 of result of experiments, this comparison shows that results from three versions of models are within error bar range of the experiments. Results for models worn height of disc are extracted from the y axis of wear track as shown in figure 4.31.

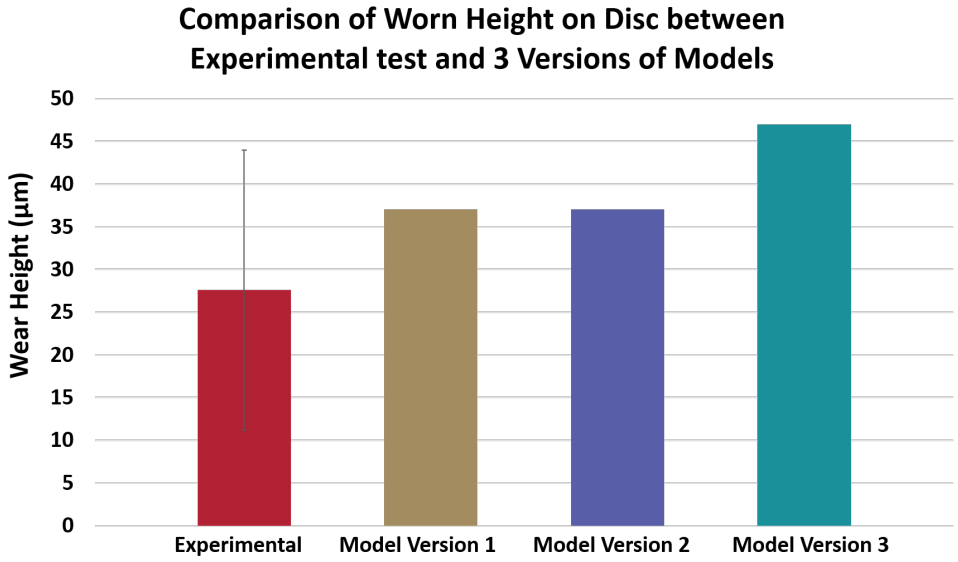

Figure 4.35: Comparison of disc worn height between experimental test and three versions of models

Next comparison is between the sphere worn patch diameter which also signify the final contact diameter between both bodies in the modelling but in experimental tests this statement may not hold as disc surface is rough and contact can occur at any point on the sphere surface in the possible region of contact zone as shown in figure A.6 in appendix 5. Following figure 4.36 shows comparison of sphere worn patch diameter and its clear that results from models are comparable to the results of experiments. Finally, the most important comparison is of the evolution of CoF curves which was extracted from experimental test and from three versions of models, it explains how CoF vary with the sliding distance, in case of expriment CoF is recorded by the Rtec tribometer and for models it is the fucntion of contact area (for the version 3, since we have established that linear increase of contact area is not the best output due to limitation of mesh size in MATLAB).

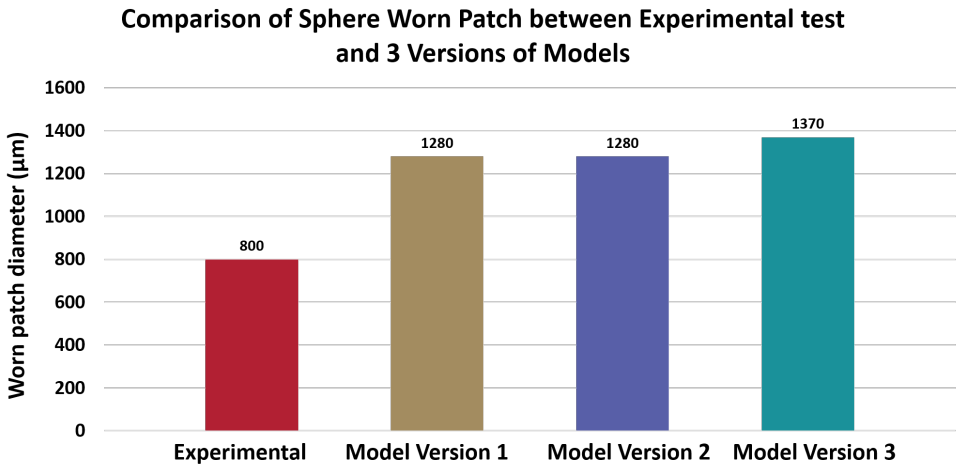

Figure 4.36: Comparison of sphere worn patch between experimental test and three versions of models

Following figure 4.37 shows this comparison and its evident that results from the version 1 and 2 are very close to the experimental values in term of evolution and data points, one important point is that initial point of curve for model output and experimental output are different, this is due to the fact shear strength of material is real in case of experimental while in case of model it has been calculated as function of hardness. That's why its important to work on the tuning of the shear strength value to make it close to real shear strength value of the material and its important to note that shear strength of sphere material which is nickel alloy will also play an important role for the evolution of CoF.

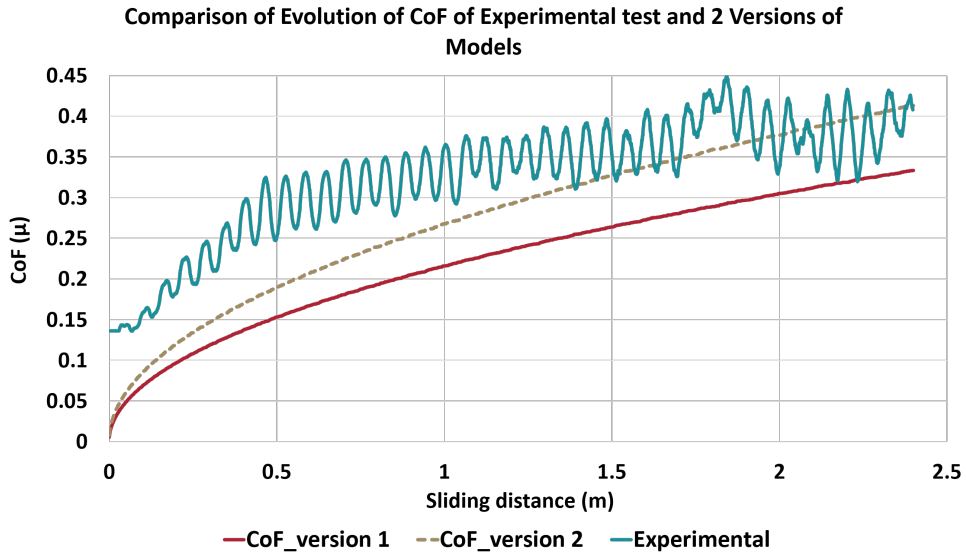

Figure 4.37: Comparison of evolution of CoF curves between experimental test and three versions of models

4.6 Discussion

The three forms of the numerical models developed in this research were compared with experimental results obtained from tribometer testing in terms of worn height, sphere worn patch diameter, total wear volume, and the evolution of the coefficient of friction (CoF). In all versions, the models were given a wear coefficient (K) derived from the experimental wear volumes in order to obtain consistency between input data and experimental wear levels. While the magnitudes of wear agree well with experiment, it must be remembered that part of this agreement arises from calibration of K to the same data, which limits the demonstration of true predictive power. Furthermore, whereas the models give detailed pressure evolution maps, there were no experimental measurements of contact pressure, so this aspect of the model results is unconfirmed.

Limitations

The existing models are beset by some limitations as follows:

- The constant τ_0 assumption ignores potential interfacial shear strength changes from running-in, debris generation, or material property development, giving rise to the noted initial CoF offset.
- Version 3's micro-contact treatment is afflicted with coarse discretisation and a set number of contact points, which unrealistically limits pressure distribution and contact area development.
- Models are verified for a single material pair and a single operating condition set, and thus their generalisability is proved to a limited extent.

Chapter 5

Conclusion & Future Work

The objectives of this thesis were threefold: (i) to develop computational models for wear and evolution of the coefficient of friction (CoF) with the effects of contact pressure, real contact area, and surface roughness; (ii) to compare these models with test data, i.e., worn geometries, volumes of wear, and CoF trends; and (iii) to identify the most significant parameters linking contact conditions, wear mechanisms, and frictional behavior in tribological systems.

These objectives were met as described. First, three progressively advanced computational models were developed. Versions 1 and 2 employed a Winkler-based contact pressure model with smooth geometry to simulate wear development and CoF evolution, Version 3 introducing a micro-contact model utilizing surface roughness input to simulate asperity-scale pressure distributions (which is limited due to mesh limitations). Taken together, these models addressed the multi-scale character of contact pressure and real contact area in governing wear and friction.

Second, experimental verification indicated that all three models successfully replicated the global experimental trends in worn height profiles, sphere worn patch diameter, overall wear volume, and CoF development. Versions 1 and 2 were capable of capturing global wear quantities and CoF evolution but Version 3 added extra fidelity for the simulation of local contact pressure and asperity-scale phenomena.

Third, the modelling work set significant parameters governing tribological behavior: actual contact area as a prime force behind CoF fluctuations, shear strength as a governing parameter of frictional resistance, and wear coefficient as a crucial input towards quantitative accuracy. These parameters uniquely connect contact conditions, wear mechanisms, and friction responses in dry sliding.

Briefly, the development, simulation, and verification of the three models enhance the insight into wear–friction coupling in tribological systems. Despite restrictions such as assuming constant shear strength, coarse discretisation at the micro-scale, and use of calibrated wear coefficients, the modelling framework provides a robust and computationally efficient foundation for prediction of wear and CoF development in industrial contexts.

Summary of Main Findings

The main findings of this study can be summarized as below:

- **Experimental analysis output:** The tribological behavior of a material pair under dry sliding was systematically investigated in the experimental research and proved that sliding distance rather than sliding velocity controls wear. The wear coefficient (K), wear volume, and coefficient of friction are independent of sliding speed so tests can be accelerated without altering the outcomes.

- **Coefficient of Friction (CoF) behavior:** In the initial running-in, coefficient of friction increased rapidly which became steady as the surfaces accommodated. This occurred well with the Winkler-based models (Versions 1 and 2) whose simulated CoF was very close to experiments, but the micro-contact rough-surface model (Version 3) produced a linear behavior due to mesh discretization sensitivity. As wear continued to increase, the true contact area increased, with the friction coefficient also increasing, displaying the physical connection between contact geometry and friction response.
- **Wear behaviour:** Experimental data revealed increasing wear with rising numbers of sliding cycles, e.g., worn height, wear patch diameter, and total volume. All the developed models were capable of simulating global wear volumes and wear patch development fairly satisfactorily.
- **Role of e (epsilon):** On the disc surface, not all points move the same distance on sliding, points close to center travel longer distance than points away from center. Local wear thus varies across the surface: areas sliding further have greater material removal, while areas shorter in travel wear less. This uneven sliding is responsible for wearing away the patch unevenly, directly affecting the patch's shape and total wear volume.

Future Work

To address the limitations, future research should focus on a coupled two-scale strategy in which micro-scale simulations resolve asperity geometry, deformation, and real contact area development and feed inputs to macro-scale wear and friction models with dynamic updating of geometry. This would be made possible through a uniform approach, aided by improved discretisation, wear and shear parameter measurements independently. This would merge the benefits of all three variants to yield a physically reasonable, predictive, and generalisable tool for modelling of broad range of materials and conditions.

Appendix A

Supplementary images

Table A.1: Roughness measurement for stainless steel disc samples

Roughness measurement by profilometer and focus variation microscope	
Parameters	Profile length (L_t) = 15mm L_s = 8µm Cutoff = λ_c (L_c) = 2.5mm
ISO standard applied	ISO 4288 and ISO 16610-21 ASME B46.1-2002
Use	λ_c = 3mm for coarser roughness range (2mm to 10mm) L_t = N x λ_c, where N=5

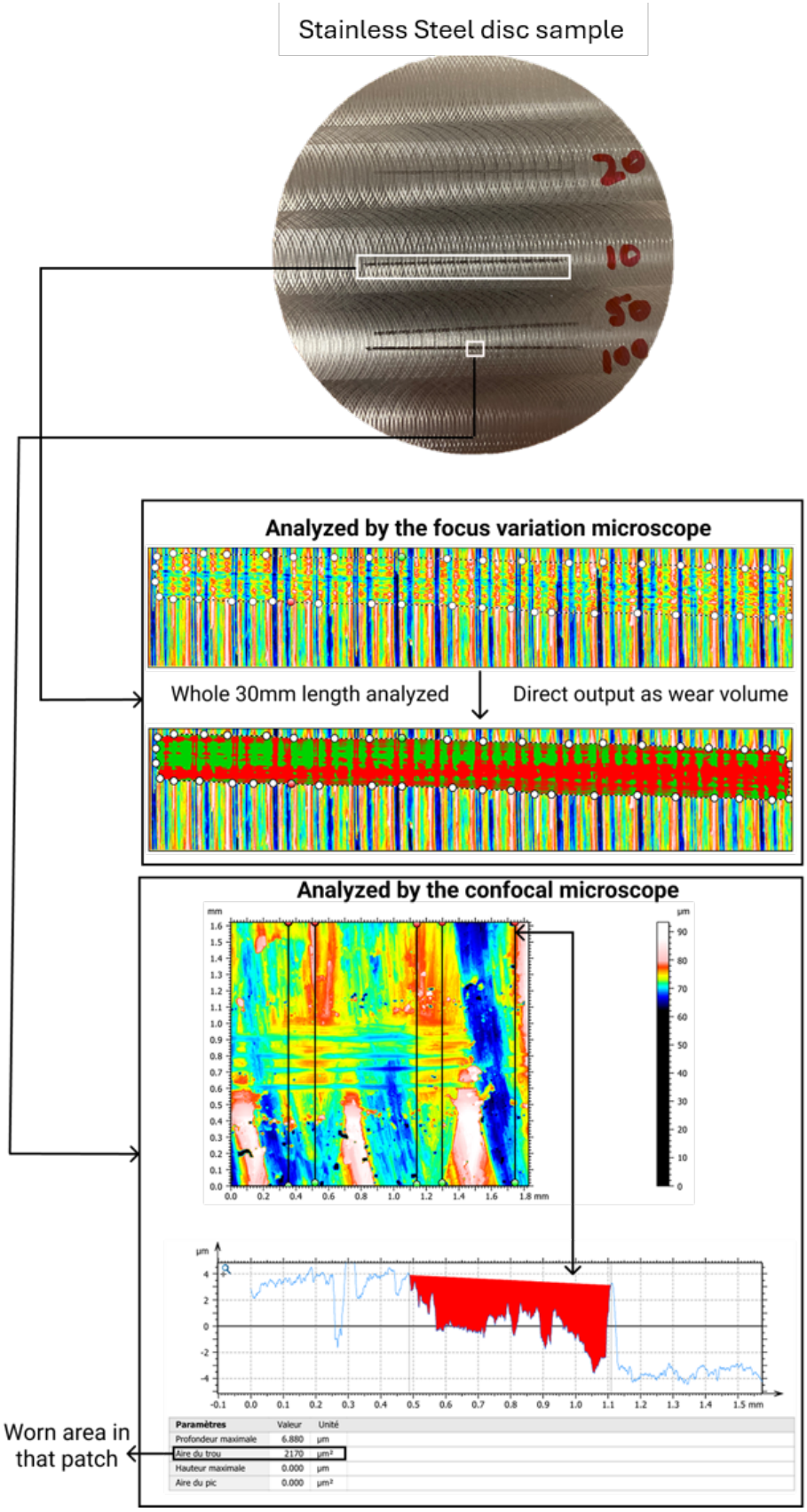

Figure A.1: Full track analyzed by focus variation microscope giving direct total wear volume as output after analyzing with MountainsMap and patch of track analyzed by confocal microscope which will give worn area after MountainsMap analyzing

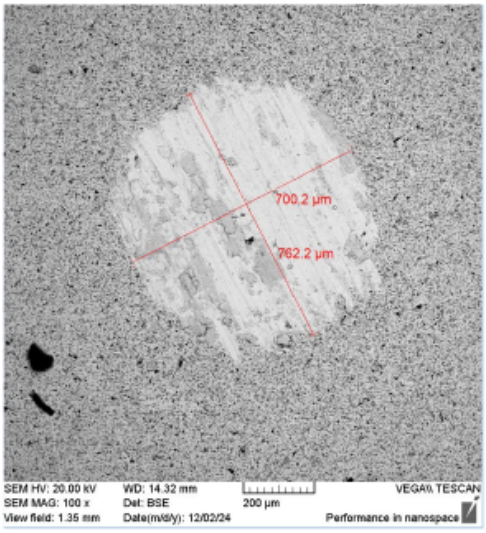

Figure A.2: Diagonals marked on worn patch on sphere on SEM

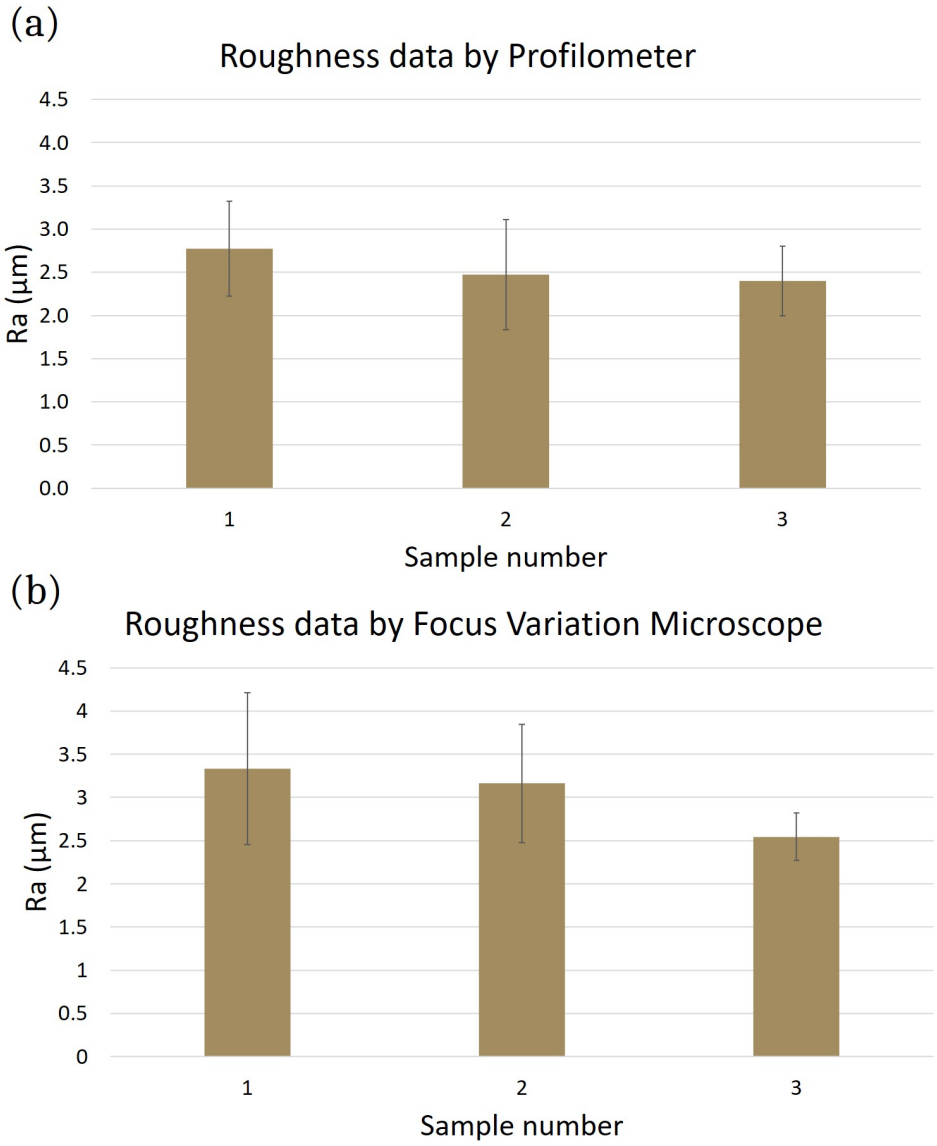

Figure A.3: Roughness analysis results (a) by profilometer, and (b) by focus variation microscope

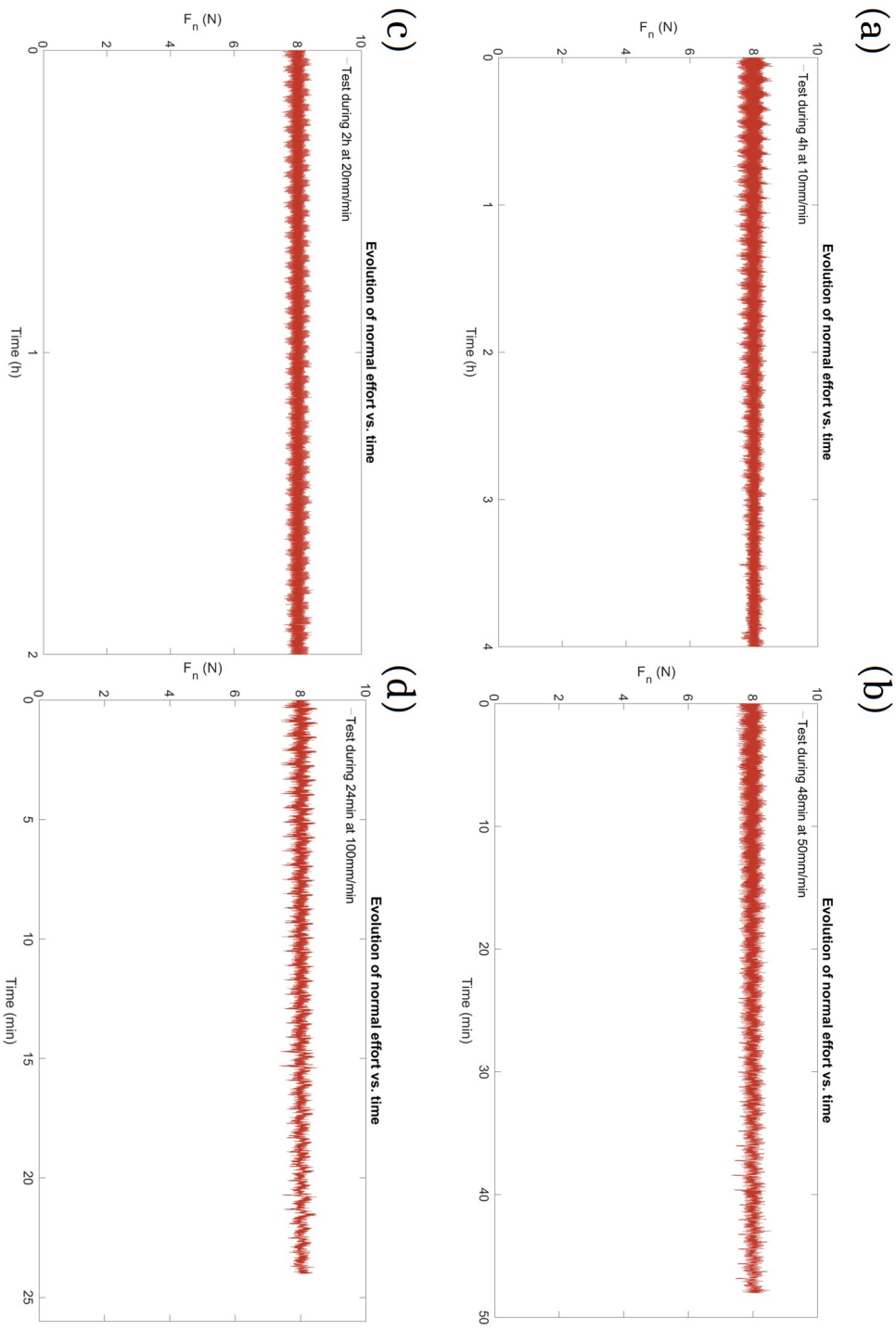

Figure A.4: Stable 8N force for (a) 10mm/min, (b) 20mm/min, (c) 50mm/min, and (d) 100mm/min

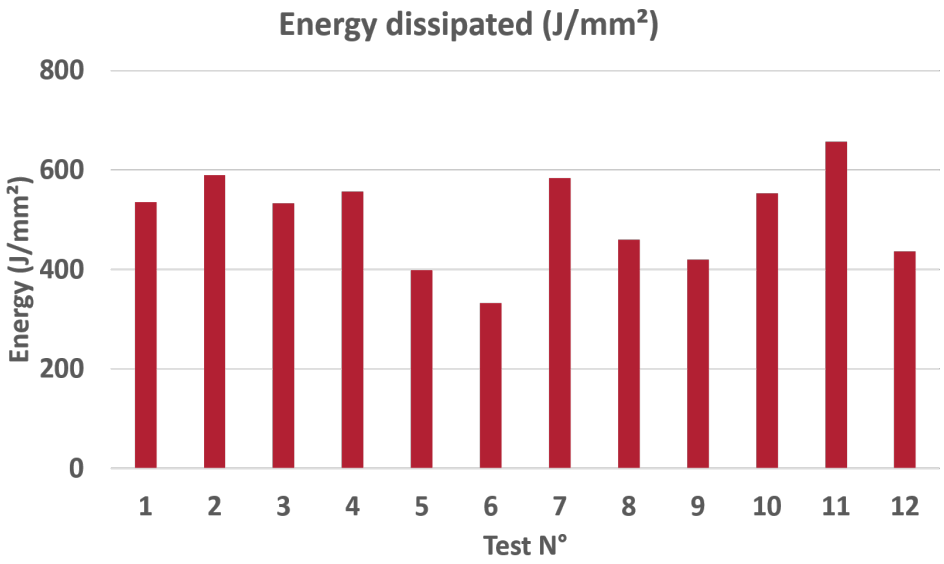

Figure A.5: Energy dissipated during each wear test

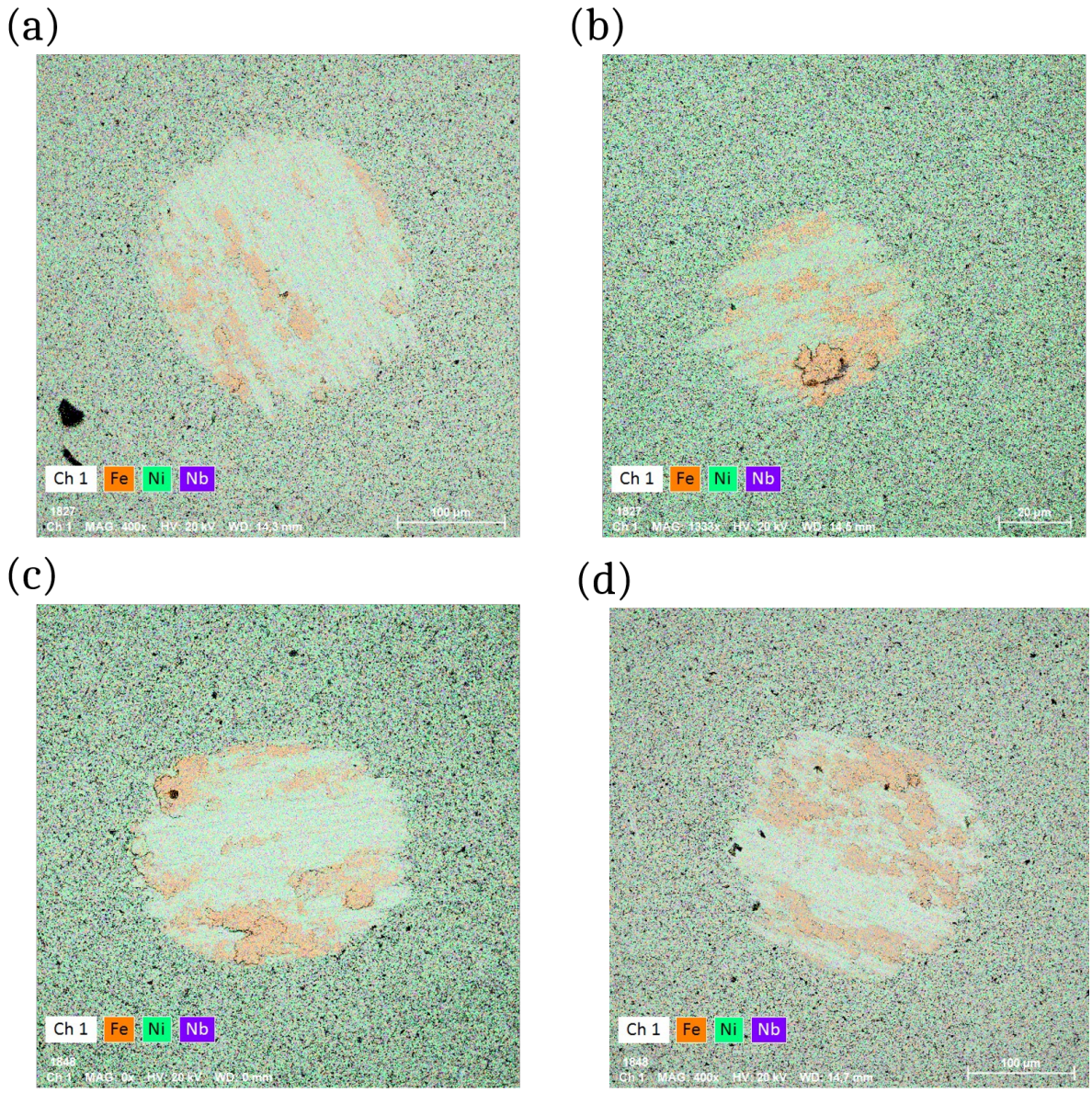

Figure A.6: Sphere worn patch analyzed by SEM at 100X (a) 10mm/min, (b) 20mm/min, (c) 50mm/min, and (d) 100mm/min

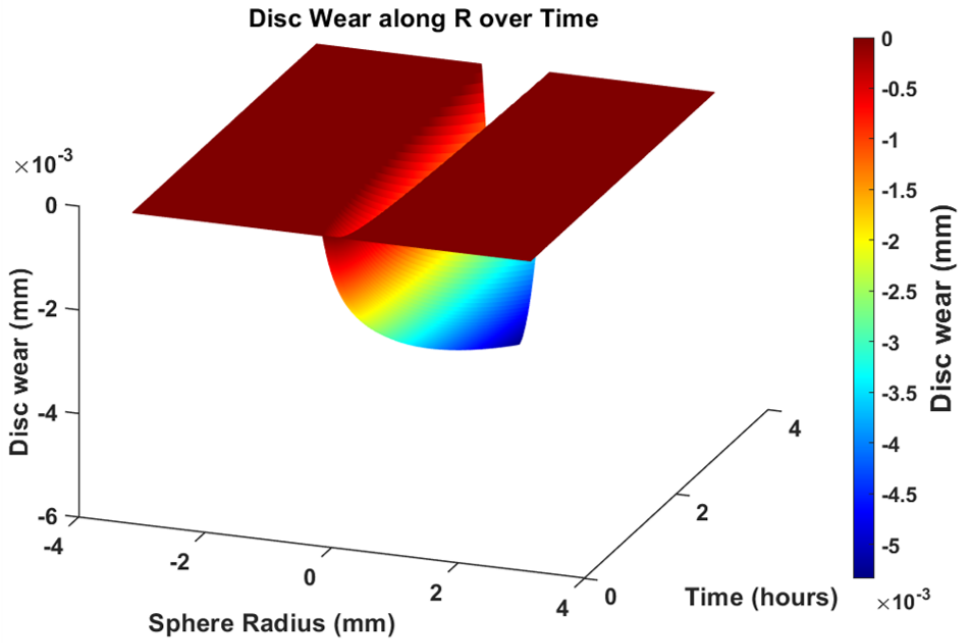

Figure A.7: Disc wear along radius of sphere motion direction against sliding time on y axis

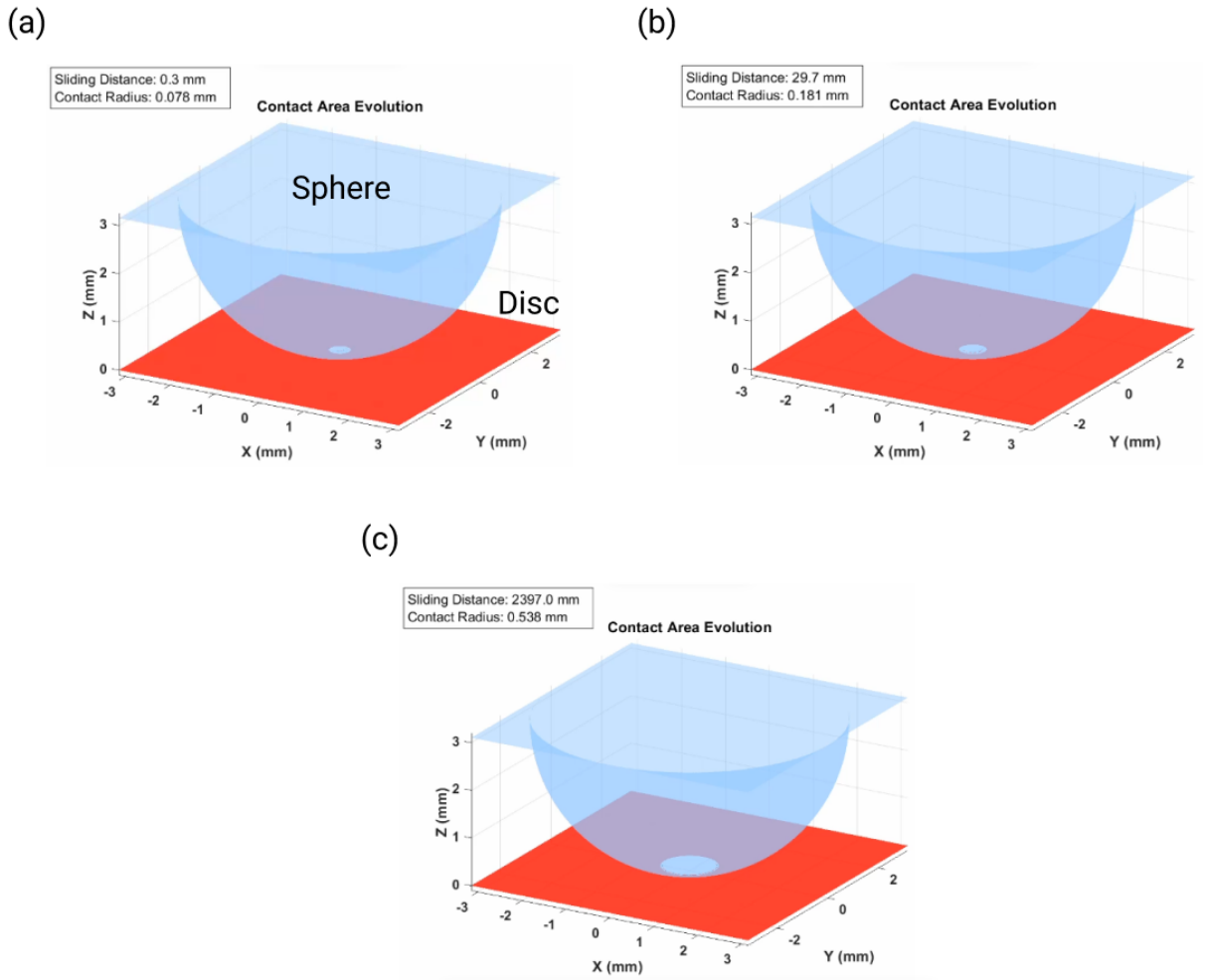

Figure A.8: Evolution of area between sphere and disc recorded at different sliding distance for comparison (a) Initial contact area same as Hertzian contact area, (b) Contact area after 30mm sliding distance, and (c) Contact area after 2400mm sliding distance

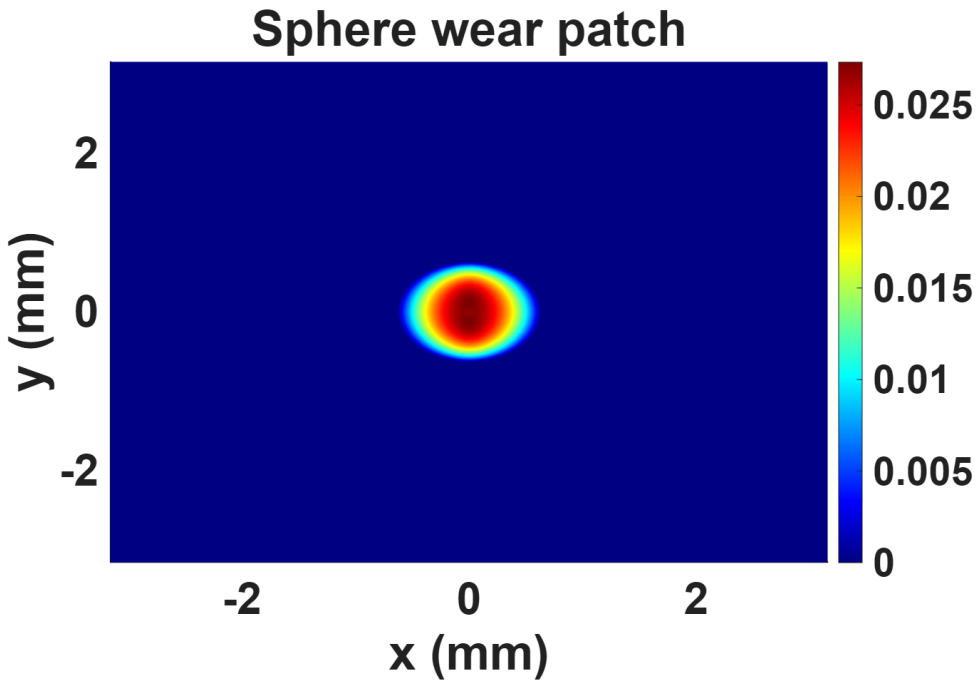

Figure A.9: Sphere worn patch geometry

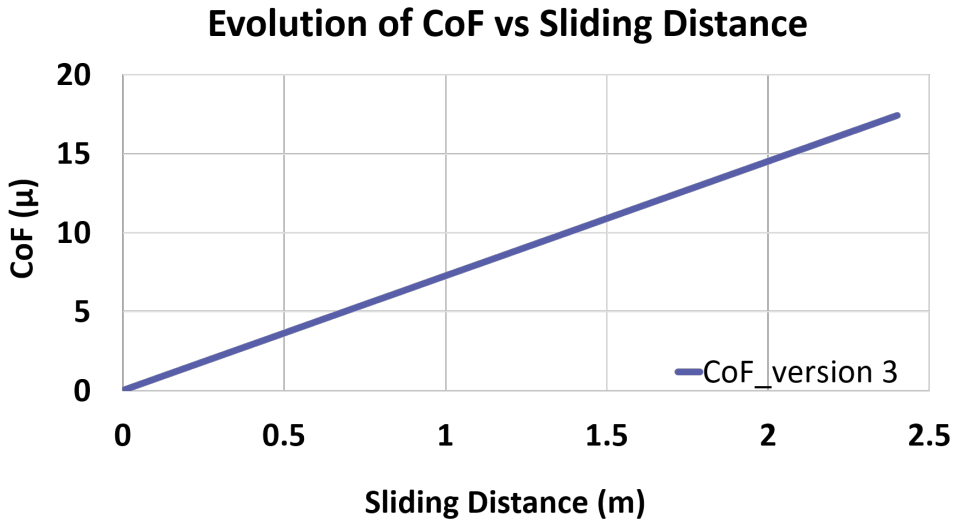

Figure A.10: Evolution of coefficient of friction for V3 vs sliding distance

Bibliography

[1] Kenneth Holmberg and Ali Erdemir. “Influence of Tribology on Global Energy Consumption, Costs and Emissions”. In: *Friction* 5.3 (2017), pp. 263–284 (cit. on pp. 1, 2).

[2] Bharat Bhushan. *Modern Tribology Handbook, Vol. 1*. CRC Press, 2000 (cit. on pp. 2, 3, 5–11, 15, 18, 20).

[3] Valentin L. Popov. *Contact Mechanics and Friction: Physical Principles and Applications*. Springer Science and Business Media, 2010 (cit. on p. 2).

[4] Duncan Dowson. *History of Tribology*. Addison-Wesley Longman Limited, 1979 (cit. on p. 2).

[5] Gwidon Stachowiak and Andrew Batchelor. *Engineering Tribology*. 4th. Elsevier, 2013 (cit. on pp. 2, 3, 8–11, 15, 20).

[6] Heinrich Hertz. *Ueber die Beruehrung elastischer Koerper (On Contact Between Elastic Bodies)*. Vol. 1. Unknown Publisher, 1882 (cit. on pp. 3, 23).

[7] K. L. Johnson. *Contact Mechanics*. Cambridge University Press, 1985 (cit. on pp. 3, 23).

[8] J. F. Archard. “Elastic Deformation and the Laws of Friction”. In: *Proceedings of the Royal Society of London A: Mathematical, Physical and Engineering Sciences* 243.1233 (1957), pp. 190–205 (cit. on pp. 3, 22).

[9] Jamal Takadoum. *Materials and Surface Engineering in Tribology*. Wiley, 2008 (cit. on pp. 3, 5, 11, 18–20).

[10] Karl-Heinz Zum Gahr. *Microstructure and Wear of Materials*. Vol. 10. Tribology Series. Amsterdam, Oxford, New York, Tokyo: Elsevier, 1987 (cit. on pp. 5, 7–10).

[11] MRO Magazine. *WON Linear Bearings and Rails*. Accessed: 2025-06-07. 2025. URL: https://www.mromagazine.com/products/won-linear-bearings-and-rails/ (cit. on p. 6).

[12] Adelaide Auto Pro. *Mercedes Brake Pads: A Comprehensive Guide*. Accessed: 2025-06-07. 2025. URL: https://www.adelaideautopro.com.au/post/mercedes-brake-pads-a-comprehensive-guide (cit. on p. 6).

[13] MecMovies. *Friction - MecMovies Module 1.9*. Accessed: 2025-06-07. 2025. URL: https://drbuc2jl8158i.cloudfront.net/shared/Engeneering/mecmovies/ch01/m01_09_s000.html (cit. on p. 6).

[14] Sterling Bearings Ltd. *Sterling Bearings*. Accessed: 2025-06-07. 2025. URL: https://www.sterlingbearings.com/ (cit. on p. 7).

[15] Ian M. Hutchings and Philip Shipway. *Tribology: Friction and Wear of Engineering Materials*. 2nd. Oxford, UK: Butterworth-Heinemann, 2017 (cit. on pp. 8–11, 17, 18).

[16] Sahar Ghatrehsamani, Saleh Akbarzadeh, and M. M. Khonsari. “Relationship between subsurface stress and wear particle size in sliding contacts during running-in”. In: *Mechanics Research Communications* 123 (2022), p. 103891. DOI: 10.1016/j.mechrescom.2022.103891 (cit. on pp. 11, 13–15).

[17] P. J. Blau. “Mechanisms for Transitional Friction and Wear Behavior of Sliding Metals”. In: *Wear* 71.1 (1981), pp. 29–43. DOI: 10.1016/0043-1648(81)90211-2 (cit. on pp. 11–14, 19, 20).

[18] N. D. Spencer. *Surfaces, Interfaces, and their Applications II – Introduction to Wear*. ETH Zurich, Switzerland, Lecture notes. 2014 (cit. on p. 11).

[19] J. Wang and H. Danninger. “Dry Sliding Wear Behavior of Molybdenum Alloyed Sintered Steels”. In: *Wear* 222.2 (1998), pp. 49–57. DOI: 10.1016/S0043-1648(98)00221-6 (cit. on pp. 12, 13).

[20] S. Ghathrehsamani and S. Akbarzadeh. “Experimental and Numerical Study of the Running-In Wear Coefficient during Dry Sliding Contact”. In: *Surface Topography: Metrology and Properties* 8.4 (2020), pp. 1–10. DOI: 10.1088/2051-672X/abbd7a (cit. on pp. 13, 14, 25, 28).

[21] Liangjie Mao, Mingjie Cai, Qingyou Liu, and Yufa He. “Effects of sliding speed on the tribological behavior of AA 7075 petroleum casing in simulated drilling environment”. In: *Tribology International* 145 (2020), p. 106194. DOI: 10.1016/j.triboint.2020.106194 (cit. on p. 14).

[22] Zhenfang Zhang, Liangchi Zhang, and Yiu-Wing Mai. “The running-in wear of a steel/SiC_p-Al composite system”. In: *Wear* 194 (1996), pp. 38–43. DOI: 10.1016/0043-1648(95)06760-3 (cit. on pp. 14, 22).

[23] S. C. Lim and M. F. Ashby. “Wear-Mechanism Maps”. In: *Acta Metallurgica* 35.1 (1987), pp. 1–24 (cit. on pp. 15, 16, 38).

[24] M. Ciavarella. “Some Remarks on a Recent Wear Theory”. In: *Tribology Letters* 73.55 (2025). DOI: 10.1007/s11249-025-01984-3 (cit. on pp. 16, 17, 28).

[25] Peter J. Blau. “How common is the steady-state? The implications of wear transitions for materials selection and design”. In: *Wear* 332-333 (2015), pp. 1120–1128. DOI: 10.1016/j.wear.2014.12.037 (cit. on p. 19).

[26] Zhihua Sha, Qiang Hao, Jian Yin, Fujian Ma, Yu Liu, and Shengfang Zhang. “Wear calculation and life prediction model of disc brake based on elastoplastic contact mechanics”. In: *Advances in Mechanical Engineering* 14.4 (2022), pp. 1–17. DOI: 10.1177/16878132221093136 (cit. on pp. 21, 23, 28).

[27] P. B. Son and J.-F. Molinari. “Adhesive wear regimes on rough surfaces and interaction of microcontacts”. In: *Tribology Letters* 69.1 (2021), p. 107. DOI: 10.1007/s11249-021-01467-3 (cit. on pp. 21, 25, 28).

[28] Michael Varenberg. “Adjusting for Running-in: Extension of the Archard Wear Equation”. In: *Tribology Letters* 70.59 (2022). DOI: 10.1007/s11249-022-01602-6 (cit. on pp. 22, 25, 28).

[29] Simon Garcin, Soha Baydoun, Pierre Arnaud, and Siegfried Fouvry. “Fretting wear modeling of 3D and 2D Hertzian contacts with a third-body layer using a Winkler elastic foundation model”. In: *Tribology International* 170 (2022), p. 107493. DOI: 10.1016/j.triboint.2022.107493 (cit. on pp. 22–24, 28).

[30] Priit Põdra and Sören Andersson. “Wear simulation with the Winkler surface model”. In: *Wear* 207.1–2 (1997), pp. 79–85 (cit. on pp. 23, 28).

[31] J.A. Greenwood and J.B.P. Williamson. “Contact of nominally flat surfaces”. In: *Proc. R. Soc. A* 295 (1966), pp. 300–319 (cit. on p. 24).

[32] Y. Zhao, D.M. Maietta, and L. Chang. “An Asperity Microcontact Model Incorporating the Transition From Elastic Deformation to Fully Plastic Flow”. In: *ASME J. Tribol.* 122 (2000), pp. 86–93 (cit. on p. 24).

[33] J. Jamari and D.J. Schipper. “An Elastic–Plastic Contact Model of Ellipsoid Bodies”. In: *Tribology Letters* 21.3 (2006), pp. 262–271 (cit. on p. 24).

[34] Guojia Ma, Liliang Wang, Haoxiang Gao, Jie Zhang, and Tom Reddyhoff. “The friction coefficient evolution of a TiN coated contact during sliding wear”. In: *Surface and Coatings Technology* 276 (2015), pp. 551–559 (cit. on pp. 25, 26, 28).

[35] Yuesheng Hu, Minghui Yang, Yong Zou, Xuesong Jin, and Daming Zhu. “Development of an interactive friction model to predict aluminum transfer in a pin-on-disc sliding system”. In: *Tribology International* 134 (2019), pp. 240–250 (cit. on pp. 26, 28).

[36] Dongdong Tian, Zhenyu Xie, Zhiqiang Shi, Hao Liu, and Yan Cheng. “Real-Time Prediction of Wear Morphology and Coefficient of Friction Using Acoustic Signals and Deep Neural Networks in a Tribological System”. In: *Processes* 13.8 (2025), p. 1762 (cit. on pp. 26, 28).

[37] Lei Yang, Yu Chen, Liren Liu, Zhengyi Sun, and Xiang Wei. “Experimental and modelling study of interaction between friction and galling under contact load change conditions”. In: *Tribology International* 174 (2022), p. 107735 (cit. on pp. 26, 28).

[38] S. Z. Wattel and J.-F. Molinari. “A story of two transitions: From adhesive to abrasive wear and from ductile to brittle regime”. In: *The Journal of Chemical Physics* 160.1 (2024), p. 014711. DOI: 10.1063/5.0176553 (cit. on p. 28).